Development and application of photofragmentation laser-induced fluorescence for visualization of hydrogen peroxides

Johansson, Olof

2011

Citation for published version (APA):
Johansson, O. (2011). *Development and application of photofragmentation laser-induced fluorescence for visualization of hydrogen peroxides*. [Doctoral Thesis (compilation), Combustion Physics].

Total number of authors:
1

Development and application of photofragmentation laser-induced fluorescence for visualization of hydrogen peroxides

Doctoral Thesis

Olof Johansson

Division of Combustion Physics
Department of Physics

LUND UNIVERSITY

ISSN 1102-8718
Lund Reports on Combustion Physics,
LRCP-143
ISRN LUTFD2/TFCP–09/143–SE
ISBN 978-91-7473-131-6

Division of Combustion Physics
P.O. Box 118
SE-221 00 Lund, Sweden

Printed by: Media Tryck AB, Lund, Sweden

Abstract

The work presented in this thesis is mainly motivated by the need for an optical diagnostic technique which can be used to visualize hydrogen peroxide (H_2O_2) in its gas phase. Due to the lack of bound electronic states, H_2O_2 cannot be detected using laser-induced fluorescence based on electronic excitation. Absorption in the ultraviolet leads to photodissociation. Thus a technique called photofragmentation laser-induced fluorescence (PF-LIF) has been developed and applied. It is a pump-probe technique that can be used for indirect detection of some non-fluorescing species. The species of interest is first dissociated using the pump-laser pulse, and the generated fragments are then probed via laser-induced fluorescence (LIF). Photofragmentation laser-induced fluorescence can be used for imaging, line measurements as well as for point measurements, and it can provide high temporal and spatial resolution.

Experimental investigations have been carried out in free flows of gas phase $H_2O_2/H_2O/N_2/O_2$ mixtures, in an industrial test rig as well as in premixed, laminar H_2/O_2, CH_4/O_2 and CH_4/air flames. Qualitative single-shot imaging during injection of H_2O_2/H_2O/air mixtures into a bottle has been applied to study H_2O_2 concentration buildup. Quantitative H_2O_2 concentration measurements have been performed by studying the chemical consumption of OH photofragments following dissociation. In order to be calibration free, the measurements should be carried out with low pump fluence. The chemical consumption of OH photofragments will then be governed by the reaction $OH + H_2O_2 \rightarrow HO_2 + H_2O$. This method has been demonstrated for H_2O_2 number densities in the range $1.16 \cdot 10^{16}$ cm^{-3} to $3.0 \cdot 10^{17}$ cm^{-3}.

Photofragmentation laser-induced fluorescence is generally subject to the usual difficulties of making LIF quantitative. The main issue is often spatial differences in fluorescence quantum yield. In order to be able to measure the radiative lifetime distribution, which is directly linked to the fluorescence quantum yield, a separate campaign was directed towards development of a new wide-field method for fluorescence lifetime imaging.

Extensive measurement campaigns have been directed towards PF-LIF measurements in laminar, premixed flames. It turned out that the majority of the OH photofragments in the studied flames were stemming from HO_2, with smaller contributions from H_2O_2 and CH_3O_2. A major challenge with the flame measurements was that OH is naturally present in flames. This signal contribution, which generally was much stronger than the signal from OH photofragments, was subtracted by recording a separate image with the pump laser blocked. This image was then subtracted from the image obtained when both the pump and the probe lasers were used.

List of Papers

This thesis is based on the following papers, which will be referenced by Roman numerals in the text. The papers are referenced and appended to the thesis in the order listed here.

I. Ehn, A., **Johansson, O.**, Bood, J., Arvidsson, A., and Aldén, M., *Fluorescence lifetime imaging detector for single-shot measurements of rapid events*, To be submitted.

II. Ehn, A., **Johansson, O.**, Bood, J., Arvidsson, A., Li, B., and Aldén, M., *Fluorescence lifetime imaging in a flame*, Proceedings of the Combustion Institute, **33**(1), 807–813, 2011.

III. **Johansson, O.**, Bood, J., Aldén, M., and Lindblad, U., *Detection of hydrogen peroxide using photofragmentation laser-induced fluorescence*, Applied Spectroscopy, **62**(1), 66–72, 2008.

IV. **Johansson, O.**, Bood, J., Aldén, M., and Lindblad, U., *Vapor phase hydrogen peroxide imaging using photofragmentation laser-induced fluorescence*, in the Conference on Lasers and Electro-Optics (CLEO)/The International Quantum Electronics Conference (IQEC) (Optical Society of America, Washington, DC, 2009), presentation CThI4.

V. **Johansson, O.**, Bood, J., Aldén, M., and Lindblad, U., *Hydroxyl radical consumption following photolysis of vapor-phase hydrogen peroxide at 266 nm: implications for photofragmentation laser-induced fluorescence measurements of hydrogen peroxide*, Applied Physics B: Lasers and Optics, **97**(2), 515–522, 2009.

VI. **Johansson, O.**, Lindblad, U., Seyfried, H., Omrane, A., Olsson, M., and Bood, J., *Visualization of vaporized hydrogen peroxide in an industrial sterilization test rig*, To be submitted.

VII. **Johansson, O.**, Bood, J., Li, B., Ehn, A., Li, Z.S. Sun, Z.W., Jonsson, M., Konnov, A.A., and Aldén, M., *Photofragmentation laser-induced fluorescence imaging in premixed flames*, Combustion and Flame, 2011, doi:10.1016/j.combustflame.2011.02.021.

VIII. Ehn, A., Jonsson, M., **Johansson, O.**, Bood, J. and Aldén, M., *Fluorescence lifetimes of toluene as a function of* O_2/N_2 *concentrations using 266 nm excitation of the* S_1-S_0 *transition*, To be submitted.

Contents

Nomenclature

2γ	torsion angle
$\bar{r}$	vector of parameters for image transform algorithms
$\boldsymbol{\Omega}$	sum of the projections of the electronic spin angular momentum and the electronic orbital angular momentum on the internuclear axis of a diatomic molecule
$\boldsymbol{\omega}$	angular velocity vector
$\boldsymbol{I}$	inertia tensor
$\boldsymbol{J}$	total angular momentum excluding nuclear spin
$\boldsymbol{N}$	sum of nuclear rotational angular momentum and electronic orbital angular momentum
$\boldsymbol{R}$	rotational angular momentum of the nuclei
δ	time jitter
$\hbar$	reduced Planck's constant
λ	wavelength
ν	photon frequency or kinematic viscosity
ϕ	fluorescence quantum yield or fuel/oxidizer equivalence ratio
ρ	radiation density at a given frequency
σ	absorption cross section
$\mathbf{a}_i$	equilibrium coordinates of atom i in rotating coordinate system
$\mathbf{d}_i$	displacement of atom i from its equilibrium position in rotating coordinate system
$\mathbf{E}$	3×3 identity matrix
$\mathbf{R}_i$	instantaneous position of atom i in nonrotating axes

$\mathbf{S}$	matrix relating rotating to nonrotating axes through Euler angles
θ, ϕ, χ	Euler angles
A_v	spin-orbit coupling constant
A_{eff}	effective cross section area of photolysis laser sheet
A_{km}	Einstein A coefficient for transition from rovibronic state k to rovibronic state m
B_v	rotational constant
B_{ij}	Einstein B coefficient for transition from rovibronic state i to rovibronic state j
c	speed of light in vacuum
D	signal ratio
D_v	centrifugal distortion constant
E	energy
F	laser fluence
F_1	rotational energy levels of OH in the $\Omega = 3/2$ energy ladder of the $X^2\Pi$ state
F_2	rotational energy levels of OH in the $\Omega = 1/2$ energy ladder of the $X^2\Pi$ state
G_i	gate function of camera i
g_J	rotational degeneracy factor
g_v	vibrational degeneracy factor
H	Hamiltonian
h	Planck's constant
I_i	signal recorded in a single pixel of camera i
J	rotational quantum number
J_α	angular momentum operator
k_B	Boltzmann constant
m_i	mass of atom i
N	quantum number of the total angular momentum excluding electronic spin and nuclear spin, or molecular number density

P	predissociation rate or probability
P_k	momentum operator for conjugate momentum corresponding to normal coordinate Q_k
Q	normal coordinates or quenching rate
Re	Reynolds number
S	fluorescence decay function
T	kinetic energy or temperature
t_i	gate delay for camera i
V	potential energy
v	vibrational quantum number

Chapter 1

Introduction

Hydrogen peroxide (H_2O_2), the hydroperoxyl radical (HO_2) and the hydroxyl radical (OH) are important molecules in combustion and atmospheric chemistry. Hydrogen peroxide is also interesting from a purely scientific point of view as it is the simplest type of molecule having internal (torsional) rotation. Due to the active oxygen content of peroxygen species, they are strong oxidizing agents. Hydrogen peroxide is, for example, used to control sludge bulking and algae in lakes and reservoirs. It is also used in the aseptic food packaging industry for sterilization of packaging materials. Hydrogen peroxide is often used in conjunction with ultraviolet (UV) radiation to improve pollutant removal. The UV radiation can be used either to prepare the contaminent or to photodissociate H_2O_2 into OH fragments. When UV transmission is limited, H_2O_2 can be used toghether with ozone (O_3) since they react and form highly oxidizing radicals and ionic species. Ultraviolet/H_2O_2 and H_2O_2/O_3 facilities have been widely used for treatment of contaminated water. For a thorough review of environmental applications as well as other applications such as paper bleaching and chemical purification, see the book by Jones [1].

OH is the most important oxidizer in the troposphere. Its formation is mainly initiated by photolysis of O_3, and its chemistry is closely linked to that of HO_2 and H_2O_2 [2, 3]. In the gas-phase, the main formation channel of sulphuric acid (H_2SO_4) begins with sulfur dioxide (SO_2) molecules being oxidized by OH [4]. In aqueous phase, however, H_2O_2 is a very important oxidant of S(IV). Two important factors for the impact of H_2O_2 are its high solubility in water and the pH dependence of the reaction rate for H_2O_2 reacting with S(IV). The possibilities of reducing SO_2 from flue gases of industrial facilities by scrubbing with H_2O_2 has been proposed and investigated [5]. Apart from cleaning the flue gas from SO_2, such treatment could provide a usable H_2SO_4 solution.

Atmospheric H_2O_2 has been measured by several research groups using different techniques. For a review, see e.g. the article by Lee et al. [6]. It is of interest to develop and apply optical methods for H_2O_2 detection. Slemr et al. [7] used tunable diode laser absorption spectroscopy. They used a White cell, which provided an optical path length of roughly 40 m and their detection limit could be reduced to 0.3 ppbv (parts per billion by volume) through extended averaging.

Baardsen and Terhune [8] were among the first to suggest laser-induced fluorescence (LIF) to be a feasible tool for atmospheric OH detection. In order to reduce interferences such as OH generation from photolysis of O_3 into $O\left(^1D\right) + O_2$ followed by reaction between $O\left(^1D\right)$ and H_2O, the sample gas is commonly expanded and LIF measurements are performed at low pressures. This method is called FAGE (fluorescence assay with gas expansion), and Hard et al. [9] were among the first to propose and apply this method. Also atmospheric HO_2 has been measured with LIF, but then indirectly by probing OH produced by the reaction $HO_2 + NO \rightarrow OH + NO_2$. A recent study using FAGE for measurements of OH and HO_2 is presented in the paper by Whalley et al. [10]. Parker et al. [11] presented a setup containing both OH detection via LIF and HO_2 detection via continuous-wave cavity ring-down spectroscopy (cw-CRDS) tuned to the overtone of the OH stretch near 1.5 μm. They used their setup to simultaneously measure HO_2 and H_2O_2, the latter species being indirectly detected through OH photofragments. Thiebaud et al. [12] measured the absorption cross sections of the 100 most intense transitions near 1.5 μm in HO_2 using cw-CRDS.

The OH radical is an important intermediate in flames and it is present in relatively large concentrations in most flames. The chain branching elementary reaction between H and O_2 forming OH and O is one of the most important reactions in hydrocarbon combustion [13]. Hence, OH has been widely studied using LIF within the combustion research community, see [14–25] for a few examples or the review article by Kose-Höinghaus [26] and references therein. Hydroperoxyl and H_2O_2 are also important flame intermediates, and both species are included in chemical kinetic combustion models such as the GRI 3.0 [27] and the detailed Konnov C/H/N/O mechanism [28]. The reaction $H + O_2 + M \rightarrow HO_2 + M$ has chain terminating character since HO_2 is less reactive than H, and this reaction is one of the most important rate-limiting reactions in hydrocarbon combustion [13]. Salooja [29] underlined the importance of H_2O_2 in hydrocarbon ignition. Pitz and Westbrook [30] concluded that the decomposition of H_2O_2 into two OH radicals is involved in the major reaction path leading to chain branching at the high pressure of the end gas in a combustion engine. They also found that H_2O_2 as well as HO_2 are decisive for high pressure autoignition. Formation of HO_2 and H from H_2 and O_2 is the most important reaction initiating chain branching in high temperature H_2/O_2 combustion systems [31].

The germicidal effects of H_2O_2 have been known for a long time, and it is suited for applications within the food industry since it decomposes to water and oxygen. The sporicidal properties of liquid H_2O_2 have been studied at different concentrations and temperatures with aseptic food packaging in mind, see e.g. [32–34]. Toledo [35] suggested H_2O_2 to be a very promising sterilant for aseptic packaging with the possibility of being used for in-line sterilization of packaging material. Apart from aseptic packaging, H_2O_2 in liquid mixtures with H_2O has been suggested for a variety of different sterilization applications, ranging from water disinfection [36, 37] to sterilization of spacecraft hardware [38].

In recent decades, H_2O_2 in its gas phase has been applied and tested as a cold gas sterilant. Wang and Toledo [39] investigated its sporicidal properties at different temperatures and Klapes and Vesley [40] used vapor phase H_2O_2 for sterilization of an ultracentrifuge. Alfa et al. [41] compared four different gas sterilizers including vaporized H_2O_2 in order to evaluate alternatives to ethylene oxide in freon. They found, however, that all four sterilizers, even ethylene in freon, showed limited results in narrow tubes when serum and salt were present. The amounts of H_2O_2 remaining after different aeration times following sterilization was measured by Ikarashi et al. [42] for different medical materials. They found a correlation between the remaining amounts of H_2O_2 and the cytotoxicity of the sterilized materials. Vapor phase H_2O_2 has also been selected and tested as a low-temperature sterilization method for spacecraft systems [43].

Corveleyn et al. [44] and Adams et al. [45] reported on near-infrared detection of H_2O and H_2O_2 for monitoring vapor concentrations. Corveleyn et al. [44] extracted the H_2O concentration by measuring the absorbance at 1364, 1378 and 1400 nm, and they attributed the absorbance at 1420 nm to be due to H_2O_2. Their measured H_2O_2 concentrations were, however, somewhat higher than the theoretical values. Adams et al. [45], on the other hand, used only absorption at 1362 nm for extraction of the H_2O concentration. They attributed the absorption at 1422 nm to be a combination of absorption by both H_2O_2 and H_2O. Hence, they calculated the H_2O absorbance at 1422 nm from the absorbance at 1362 nm through the known absorption ratio at these two wavelengths. The calculated H_2O absorbance at 1422 nm was then subtracted from the measured absorbance at 1422 nm, and the H_2O_2 concentration was finally calculated using its absorption coefficient at 1422 nm.

The vast industrial applications of H_2O_2 along with its importance in atmospheric and combustion chemistry makes it both interesting and necessary to develop measurement techniques for this species. Since HO_2 and OH are connected to H_2O_2 and also are vital in various oxidation processes, the simultaneous detection of these species is of interest.

Chapter 2

Motivation

The current project is a collaboration between the Division of Combustion Physics at Lund University and Tetra Pak Packaging Solutions AB, with the goal of developing a method for visualization and measurement of vapor phase H_2O_2. A requirement is that the technique provides high temporal and high spatial resolution, and that it can be a complement to absorption methods. The ability to visualize in two dimensions (2D) is important in order to be able to understand flow patterns in complicated machines and to compare experimental measurements with computational fluid dynamics (CFD) calculations. For comparison purpose, it is also important to be able to measure the concentration in a point. Absorption techniques fail in both these aspects since they are line-of sight techniques and thus at best only provide the average concentration value over the absorption path. In addition, by developing sensors based on different physical concepts, sensors can be used to validate each other.

For industrial applications of H_2O_2, typical questions that need to be answered are whether decomposition of H_2O_2 occurs, if there are any droplets and how long does it take for local concentration buildup, e.g. at a certain point in a package that is being sterilized. Measuring in 2D is sometimes important for the understanding of chemical and physical systems since it provides information about shapes and profiles and not just concentrations. Being able to record images in single shot is not only time saving, but in some cases necessary in order to observe different phenomena. An image of a turbulent flow, for example, can not be built up by individual point measurements performed in succession since the flow is not constant over time. Another example is a measurement environment that changes over time, rendering comparison between measurements obtained at different times difficult. This problem of different measurement environments may also, however, affect single-shot measurements since physical parameters and chemical environments may differ in space.

An optical measurement technique, which could fulfill many of the requirements is LIF. It is one of the most widely used optical measurement techniques for imaging. There are, however, two main challenges with applying LIF for H_2O_2 measurements. First of all, for reasons that will become clear later, LIF based on electronic excitation can not be applied directly on H_2O_2. We have proposed and showed that it is feasible to solve this problem by preceding LIF by photodissociation. The second challenge is to be able to use LIF for quantitative measurements. A major effort of this Ph.D. project has been to develop a robust and reliable method that can be used to detect and measure absolute H_2O_2 concentrations in the interval from $\sim$100 ppm to $\sim$30000 ppm in the temperature range $\sim$300 K to $\sim$400 K. In order to address the problems arising when trying to perform quantitative LIF measurements in single shot or in single acquisition, an effort has also been directed towards fluorescence lifetime imaging for correction of differences in fluorescence quantum yield.

Chapter 3

The H_2O_2 molecule

Even though detailed information about the energy levels of the ground state of H_2O_2 is not important in order to grasp the essence of this thesis, it is instructive to give a brief introduction on the torsion of the two OH rotors around the O-O bond since it has fueled the scientific interest in H_2O_2, and it has been the subject of a significant number of studies, see [46–51] for a few examples. In addition, the torsion is one of the two most important coordinates involved in the UV photodissociation of H_2O_2, the other one being the O-O stretch, which is the coordinate along which the dissociation ultimately occurs [52, 53]. Section 3.1 is, however, not important for the understanding of the rest of the contents of this thesis and may thus be skipped. Sections 3.2, on the other hand, lay the foundation for the measurement method used for H_2O_2 detection in the work making up the basis of the current thesis.

3.1 Ground state energy levels

Several experimental investigations of the H_2O_2 spectrum have been performed in the 3.7 mm to 430 μm (microwave) range [54–56], the mid- and far infrared [46, 47, 57, 58], the 7.9 μm band [59–61], the 3.7 μm region [62, 63], and in the 2.7 μm region [62–64]. These studies along with various calculations [52, 53, 65–72] have laid much of the foundation for the understanding of H_2O_2 spectroscopy.

Following the outline of Dellepiane et al. [73], two coordinate systems are introduced; one static (*XYZ*) and one rotating system (*xyz*). The origin of the *xyz* coordinate system is chosen to be the instantaneous center of mass of the molecule. Since the kinetic energy associated with translation of the molecule's center of mass will separate from rotation and vibration, it can be dropped. Neglecting translation is justified by the fact that it is not quantized and, therefore, does not contain information of spectroscopic interest. Thus, the origin of the static coordinate system can also be chosen to be the instantaneous center of mass of the molecule. Denote by $\mathbf{R}_i$ and $\mathbf{t}_i = \mathbf{a}_i(\gamma) + \mathbf{d}_i$ the instantaneous position of the i:th atom in the *XYZ* and *xyz* coordinate systems, respectively. The vectors $\mathbf{a}_i$ and $\mathbf{d}_i$ are the reference position of the i:th atom and its displacement from the reference position. As indicated, the reference position depends on the torsion angle, 2γ.

Introduce the matrix $\mathbf{S}(\theta, \phi, \chi)$ defined by Wilson et al [74]:

$$\mathbf{S} = \begin{bmatrix} \cos\theta\cos\phi\cos\chi - \sin\phi\sin\chi & \cos\theta\sin\phi\cos\chi + \cos\phi\sin\chi & -\sin\theta\cos\chi \\ -\cos\theta\cos\phi\sin\chi - \sin\phi\cos\chi & -\cos\theta\sin\phi\sin\chi + \cos\phi\cos\chi & \sin\theta\sin\chi \\ \sin\theta\cos\phi & \sin\theta\sin\phi & \cos\theta \end{bmatrix},$$

where θ and ϕ are the polar angles of *z* in the *XYZ* coordinate system and χ is the counter-clockwise rotation angle in the *xy* plane about the *z* axis. Starting from the *XYZ* axes, the matrix **S** describes three successive rotations in the following order:

(i) counter-clockwise rotation about the Z axis through an angle ϕ. It results in the *X'* and *Y'* axes.

(ii) counter-clockwise rotation about the *Y'* axis through an angle θ. It results in the *X"* and *Z"* $=$ *z* axes.

(iii) counter-clockwise rotation about the *z* axis through an angle χ. It results in the *x* and *y* axes.

It can be summarized by equation 3.1:

$$\begin{bmatrix} x \\ y \\ z \end{bmatrix} = \mathbf{S} \begin{bmatrix} X \\ Y \\ Z \end{bmatrix} \tag{3.1}$$

The matrix **S** has the following properties:

$$\mathbf{S}\mathbf{S}^{\mathrm{T}} = \mathbf{E} \tag{3.2}$$

$$\mathbf{S}\dot{\mathbf{S}}^{\mathrm{T}} = \begin{bmatrix} 0 & -\omega_z & \omega_y \\ \omega_z & 0 & -\omega_x \\ -\omega_y & \omega_x & 0 \end{bmatrix} \tag{3.3}$$

In equation 3.2, **E** is the 3×3 identity matrix, and ω_x, ω_y and ω_z in equation 3.3 are the components of the angular velocity vector $\boldsymbol{\omega}$.

Using **S**, the vectors $\mathbf{R}_i$ and $\mathbf{t}_i$ can be related to each other:

$$\mathbf{R}_i = \mathbf{S}^{\mathrm{T}}\mathbf{t}_i = \mathbf{S}^{\mathrm{T}}\left(\mathbf{a}_i\left(\gamma\right) + \mathbf{d}_i\right), \tag{3.4}$$

and the classical kinetic energy can thus be written:

$$2T = \sum_{i=1}^{4} m_i \dot{\mathbf{R}}_i^{\mathrm{T}} \dot{\mathbf{R}}_i = \sum_{i=1}^{4} m_i \dot{\mathbf{R}}_i^{\mathrm{T}} \mathbf{S}^{\mathrm{T}}\mathbf{S}\dot{\mathbf{R}}_i =$$

$$= \sum_{i=1}^{4} m_i \left(\mathbf{t}_i^{\mathrm{T}} \dot{\mathbf{S}} \mathbf{S}^{\mathrm{T}} \mathbf{S} \dot{\mathbf{S}}^{\mathrm{T}} \mathbf{t}_i + \mathbf{t}_i^{\mathrm{T}} \dot{\mathbf{S}} \mathbf{S}^{\mathrm{T}} \dot{\mathbf{t}}_i + \dot{\mathbf{t}}_i^{\mathrm{T}} \mathbf{S} \dot{\mathbf{S}}^{\mathrm{T}} \mathbf{t}_i + \dot{\mathbf{t}}_i^{\mathrm{T}} \dot{\mathbf{t}}_i \right) \tag{3.5}$$

Using equation 3.3, the first term on the lower line of equation 3.5 can be identified as $\boldsymbol{\omega}^{\mathrm{T}} \boldsymbol{I} \boldsymbol{\omega}$, where $\boldsymbol{I}$ is the moment of inertia tensor:

$$\boldsymbol{I} = \begin{bmatrix} \sum_{i=1}^{4} m_i \left(\mathrm{t}_{iy}^2 + \mathrm{t}_{iz}^2 \right) & -\sum_{i=1}^{4} m_i \mathrm{t}_{ix} \mathrm{t}_{iy} & -\sum_{i=1}^{4} m_i \mathrm{t}_{ix} \mathrm{t}_{iz} \\ -\sum_{i=1}^{4} m_i \mathrm{t}_{iy} \mathrm{t}_{ix} & \sum_{i=1}^{4} m_i \left(\mathrm{t}_{ix}^2 + \mathrm{t}_{iz}^2 \right) & -\sum_{i=1}^{4} m_i \mathrm{t}_{iy} \mathrm{t}_{iz} \\ -\sum_{i=1}^{4} m_i \mathrm{t}_{iz} \mathrm{t}_{ix} & -\sum_{i=1}^{4} m_i \mathrm{t}_{iz} \mathrm{t}_{iy} & \sum_{i=1}^{4} m_i \left(\mathrm{t}_{ix}^2 + \mathrm{t}_{iy}^2 \right) \end{bmatrix} \tag{3.6}$$

The second and third terms on the lower line of equation 3.5 are equal and yield:

$$2 \sum_{i=1}^{4} m_i \mathbf{t}_i^{\mathrm{T}} \dot{\mathbf{S}} \mathbf{S}^{\mathrm{T}} \dot{\mathbf{t}}_i = 2 \boldsymbol{\omega}^{\mathrm{T}} \sum_{i=1}^{4} m_i \mathbf{t}_i \times \dot{\mathbf{t}}_i \tag{3.7}$$

Thus, the kinetic energy can be written:

$$2T = \boldsymbol{\omega}^{\mathrm{T}} \boldsymbol{I} \boldsymbol{\omega} + 2 \boldsymbol{\omega}^{\mathrm{T}} \sum_{i=1}^{4} m_i \mathbf{t}_i \times \dot{\mathbf{t}}_i + \sum_{i=1}^{4} m_i \dot{\mathbf{t}}_i^{\mathrm{T}} \dot{\mathbf{t}}_i \tag{3.8}$$

Since the origin of the coordinate systems is the instantaneous center of mass, the following conditions hold:

$$\sum_{i=1}^{4} m_i \mathbf{a}_i \left(\gamma \right) = 0 \tag{3.9}$$

$$\sum_{i=1}^{4} m_i \mathbf{d}_i = 0 \tag{3.10}$$

It might at first glance seem strange that both equation 3.9 and equation 3.10 are satisfied at the same time. Consider a system where all atoms are in their equilibrium positions. Clearly the two equations are satisfied since the origin coincides with the center of mass of the molecule. If one atom is displaced from its equilibrium position, the center of mass of the molecule will be shifted. However, a movement of the center of mass is included in the translation. Hence, it can be imagined that the center of mass and the equilibrium positions are kept in the same positions as prior to the displacement of the atom. Instead the entire molecule with one of its atoms displaced from the equilibrium position is translated in such a way that the new center of mass of the molecule coincides with the original position of the molecular mass center. It means that all atoms instead of just one have been displaced from their equilibrium positions. Equation 3.9 is obviously fulfilled since neither the center of mass, nor the equilibrium positions have changed. Equation 3.10 is, however, also satisfied since the origin is the center of mass of the molecule.

Equation 3.10 provides three constraints on $\mathbf{d}_i$, which have been used to separate translational energy from other motions. However, the left hand side of equation 3.4 only has three degrees of freedom, while the right hand side has seven (three components of $\mathbf{d}_i$, θ, ϕ, χ and γ). Four additional constraints are required to bring the degrees of freedom on the right hand side of equation 3.4 down to three. These additional constraints are with advantages explained in [73] chosen to be:

$$\sum_{i=1}^{4} m_i \mathbf{a}_i (\gamma) \times \mathbf{d}_i = \mathbf{0} \tag{3.11}$$

$$\sum_{i=1}^{4} m_i \left(d\mathbf{a}_i/d\gamma\right)^{\mathrm{T}} \mathbf{d}_i = 0 \tag{3.12}$$

If the time derivatives of equations 3.11 and 3.12 are used, equation 3.8 can be written:

$$\begin{aligned} 2T = \boldsymbol{\omega}^{\mathrm{T}} \boldsymbol{I} \boldsymbol{\omega} + 2\dot{\gamma}\boldsymbol{\omega}^{\mathrm{T}} \sum_{i=1}^{4} m_i \left(\mathbf{a}_i + 2\mathbf{d}_i\right) \times \left(d\mathbf{a}_i/d\gamma\right) + 2\boldsymbol{\omega}^{\mathrm{T}} \sum_{i=1}^{4} m_i \mathbf{d}_i \times \dot{\mathbf{d}}_i + \\ \sum_{i=1}^{4} m_i \dot{\mathbf{d}}_i^{\mathrm{T}} \dot{\mathbf{d}}_i + \dot{\gamma}^2 \sum_{i=1}^{4} m_i \left(\left(d\mathbf{a}_i/d\gamma\right)^{\mathrm{T}} \left(d\mathbf{a}_i/d\gamma\right) - 2\mathbf{d}_i^{\mathrm{T}} \left(d^2\mathbf{a}_i/d\gamma^2\right) \right) \end{aligned} \tag{3.13}$$

Introduce normal coordinates, Q, along with the Meal and Polo matrices [75]. The Meal and Polo matrices allow vector products to be expressed in matrix form. Equation 3.13 can then be rewritten in a more compact form. The calculations are not shown here. Instead the result is quoted and the interested reader is referred to e.g. Dellepiane et al. [73] for details.

$$2T = \sum_{\alpha} \sum_{\beta} \omega_\alpha I_{\alpha\beta} \omega_\beta + \sum_{k=1}^{5} \dot{Q}_k^2 + 2 \sum_{\alpha} \omega_\alpha \sum_{k=1}^{5} \sum_{l=1}^{5} \zeta_{kl}^{\alpha} Q_k \dot{Q}_l, \tag{3.14}$$

where $\alpha, \beta = x, y, z$ and γ, and $\boldsymbol{\omega}$ has four components, i.e. $\boldsymbol{\omega} = (\omega_x, \omega_y, \omega_z, \dot{\gamma})$. Note that the inertia tensor, $\boldsymbol{I}$, in equation 3.14 is described by a 4×4 matrix as compared to the 3×3 matrix in equation 3.6. The additional components, $I_{\alpha\gamma} = I_{\gamma\alpha}$ and $I_{\gamma\gamma}$, are not presented here since the calculations when going from equation 3.13 to equation 3.14 have been left out.

Wilson et al. [74] explain a procedure which can be used to obtain a quantum mechanical form of the kinetic energy using the volume element $d\tau = dQ_1 dQ_2 dQ_3 dQ_4 dQ_5 sin\theta d\theta d\phi d\chi d\gamma$. Going through this procedure is well beyond the scope of this thesis, and the obtained expression for the molecular Hamiltonian is simply stated:

$$H = \frac{1}{2}\sum_{\alpha}\sum_{\beta}\mu^{1/4}\left(J_\alpha - p_\alpha\right)\mu_{\alpha\beta}\mu^{-1/2}\left(J_\beta - p_\beta\right)\mu^{1/4} + \\ \frac{1}{2}\sum_{k=1}^{5}\mu^{1/4}P_k\mu^{-1/2}P_k\mu^{1/4} + V \tag{3.15}$$

In equation 3.15, $\alpha, \beta = x, y, z, \gamma$, and J_x, J_y, J_z are the angular momenta about the molecular axes.

$$J_x = -i\hbar\left(\sin\chi\frac{\partial}{\partial\theta} - \frac{\cos\chi}{\sin\theta}\frac{\partial}{\partial\phi} + \cot\theta\cos\chi\frac{\partial}{\partial\chi}\right) \tag{3.16}$$

$$J_y = -i\hbar\left(\cos\chi\frac{\partial}{\partial\theta} + \frac{\sin\chi}{\sin\theta}\frac{\partial}{\partial\phi} - \cot\theta\sin\chi\frac{\partial}{\partial\chi}\right) \tag{3.17}$$

$$J_z = -i\hbar\frac{\partial}{\partial\chi} \tag{3.18}$$

$$J_\gamma = -i\hbar\frac{\partial}{\partial\gamma} \tag{3.19}$$

$$P_k = -i\hbar\frac{\partial}{\partial Q_k} \tag{3.20}$$

$$p_\alpha = \mathbf{Q}^{\mathrm{T}}\zeta^\alpha\mathbf{P} \tag{3.21}$$

Furthermore, μ is the determinant of the matrix made up of elements $\mu_{\alpha\beta}$. This latter matrix is the inverse of the matrix made up of elements:

$$I_{\alpha\beta} - \sum_{k=1}^{5}\sum_{l=1}^{5}\sum_{m=1}^{5}\zeta_{km}^{\alpha}\zeta_{lm}^{\beta}Q_kQ_l, \tag{3.22}$$

An approximation to equation 3.15 can be obtained by neglecting p_α and p_β along with the Q-dependence of the matrix made up of $\mu_{\alpha\beta}$. This approximation allows separation of the vibrational and the torsional-rotational problems:

$$H = \frac{1}{2}\sum_{\alpha}\sum_{\beta}\mu^{1/4}J_\alpha\mu_{\alpha\beta}\mu^{-1/2}J_\beta\mu^{1/4} + \frac{1}{2}\sum_{k=1}^{5}P_kP_k + V \tag{3.23}$$

In the torsional axis system, the torsion-rotation part of equation 3.23 can be written according to the following equation (calculations have been left out since they are beyond the scope of this thesis. The interested reader is referred to the paper by Flaud et al. [47]):

$$H_{tr} = \sum_{\alpha=x,y,z} \bar{B}_{\alpha\alpha} J_\alpha^2 + \bar{B}_{xz} \left\{J_x, J_z\right\} + \left\{J_\gamma^2, B_{\gamma\gamma}\right\} + \bar{V}\left(\gamma\right), \tag{3.24}$$

where $\left\{J_\gamma^2, B_{\gamma\gamma}\right\}$ is related to the torsional motion. Due to the fact that the hydrogen mass is relatively small compared to the oxygen mass, the H_2O_2 molecule very closely resembles a symmetric top with a torsional contribution [46, 47]. Flaud et al. [47] provides Fourier expansion coefficients for the torsional potential. Using these coefficients, the torsional part of equation 3.24 can be solved numerically. The five lowest energy levels have been included in Figure 3.1 along with the squared torsional wave functions for three of these energy levels. The two other squared torsional wave functions have been left out in order not to make the plot too busy. The cis and trans configurations of the H_2O_2 molecule have been indicated on the y-axis. The cis configuration corresponds to a torsion angle of 0 rad, while the trans configuration is found for a torsion angle of π rad.

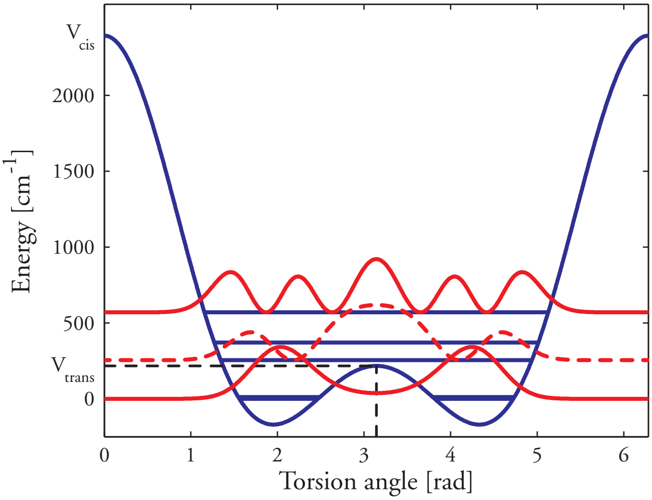

Figure 3.1: *Calculated torsional energy levels and squared wave functions. The lowest energy levels are separated only by 11.4 cm^{-1}, and they hence seem to lie on top of each other in the plot. The cis and trans configurations of the H_2O_2 molecule have been indicated. The molecule is seen to be in its cis configuration when the torsion angle, also called dihedral angle, is 0 rad, while the trans configuration (black dashed line) is when the torsion angle is π rad.*

3.2 Electronic excitation and photodissociation

The absorption spectrum of H_2O_2 in the UV is smooth and featureless [76] due to unbound excited electronic states. The angular anisotropy parameter, β, suggests that the $\tilde{A}^1$A and the $\tilde{B}^1$B excited electronic states are involved in the 193 nm photodissociation [77]. At 266 nm [78, 79] and in the wavelength region 280 nm to 290 nm [80] experiments suggest that the dissociation proceeds via the $\tilde{A}^1$A state only. Brouard et al. [81] reported that between 308 nm and 465 nm both the $\tilde{A}^1$A and the $\tilde{B}^1$B are involved in the dissociation. The recommended value for the quantum yield of OH formation following photodissociation of H_2O_2 at wavelengths longer than 230 nm is 2.0, i.e. two OH fragments are formed [82]. This value was quite recently validated by Thiebaud et al. for 248 nm photodissociation [83].

The rotational distribution of the nascent OH population following photodissociation of H_2O_2 at 300 K using 193 nm was studied by Jacobs et al. [84]. They found that the rotational distribution resembled a Gaussian peaking at N = 12 (see section 4.2 for the definition of N) with a FWHM of roughy $\Delta N = 7$. Grunewald et al. [85] performed 193 nm photolysis measurements on H_2O_2 cooled to around 20 K by jet expansion. The nascent OH rotational distribution was bell-shaped and peaked at N = 12 with a FWHM of about $\Delta N = 5$. The mild temperature dependence obtained in these experiments indicates that it is mainly strong final state interaction that determines the product state distribution [86]. Schinke and Staemmler [87] and Shinke [88] modeled the photodissociation of H_2O_2 at 193 nm using a semiclassical picture. They treated the excited states classically by numerically solving Hamilton's equations on these excited potential energy surfaces. In deriving the classical Hamilton function, they assumed the H_2O_2 molecule to be made up of two connected rigid rotors. The treatment of the ground state was done to mimic a quantum mechanical description. The total wave function of the ground state was assumed to be separable in all coordinates. Moreover, the H_2O_2 molecules were assumed to be in the lowest vibrational state, and all coordinates and momenta except for the torsion angle were assumed to mimic quantum mechanical harmonic oscillators with distributions given by Gaussian functions. The torsion angle was chosen randomly and then weighted by its probability given by the square of the torsional wave function for the chosen energy state. The rotational distribution was achieved by running at least 1000 trajectories for which nine of the ten initial coordinates were chosen randomly. The tenth coordinate, i.e. the length of the vector between the centers of mass of the two OH groups, was determined from energy conservation. Each trajectory was weighted by its statistical weight given by the distribution functions for the coordinates. The calculated nascent rotational population distributions of the OH photofragments overlapped experimental observations very accurately at both 20 K and 300 K. A similar Monte-Carlo integration performed by the author, including 25000 trajectories for 193 nm photodissociation at 300 K, resulted in the rotational distribution shown in figure 3.2. Expressions for excited potential energy surfaces were taken from [89]. These expressions are approximate fits to the potential energy surfaces used by Schinke and Staemmler [87], and they only depend on the O-O interatomic distance and the torsion angle. The branching ratios were taken to be 0.7 and 0.3 for the $\tilde{A}$ and $\tilde{B}$ states respectively. Also shown in the figure are the experimental results reported in [84] under the assumption that all four splitting components $\left({}^2\Pi^+_{3/2}, {}^2\Pi^-_{3/2}, {}^2\Pi^+_{1/2}, {}^2\Pi^-_{1/2}\right)$ are equally populated.

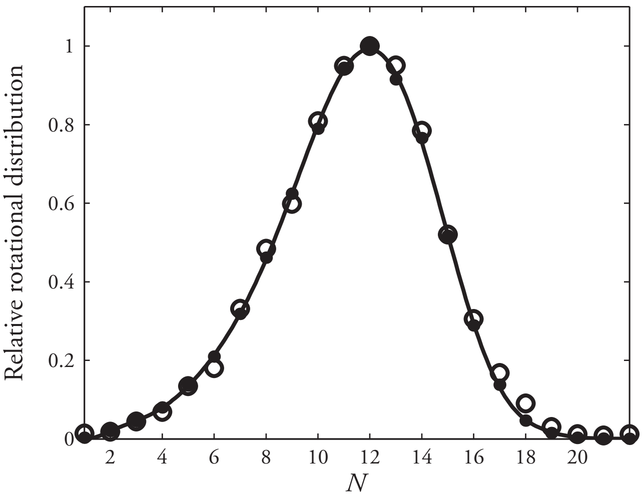

Figure 3.2: *Calculated relative rotational population distribution of the nascent OH fragments formed from 193 nm photodissociation (solid circles). The open circles show the distribution obtained experimentally [84] under the assumption that all four splitting components of the OH photofragments are equally populated. The solid line is a polynomial fit to the calculated points.*

A problem with a semiclassical approach is that Hamilton's equations assume that position and momentum can be exactly specified at any point in time, which is contradictory to the Heisenberg uncertainty principle. However, the amount of energy released in photodissociation processes is often large enough for the wave function to perform several oscillations over the interaction region due to the short deBroglie wavelength, justifying a classical description [90]. While single-photon photodissociation of H_2O_2 at 193 nm seems to be well characterized by a semiclassical picture, Cai et al. [89] pointed out that the photon energies at 266 nm and 248 nm are not large enough to reach the $\tilde{A}$ and $\tilde{B}$ states from the ground state equilibrium geometry. Recent calculations suggest that the vertical excitation energies for the $\tilde{A}^1$A state is in the range 5.49-5.95 eV and in the range of 6.69-7.10 eV for the $\tilde{B}^1$B state [52, 53, 91]. The available photon energies at 266 nm and 248 nm are 4.66 eV and 5.00 eV, respectively. Accordingly, photodissociation at these wavelengths will access a classically forbidden region at and near the equilibrium geometry, and quantum mechanical calculations are thus preferable [89].

The OH photofragments produced by single-photon absorption of H_2O_2 are generated with a high degree of translational energy. At 266 nm, translation accounts for 90% of the energy available in the exit channel [78]. At the same wavelength, less than 0.2% ends up as vibrational energy, with remaining energy going into rotation [78]. Similarly, vibrational excitation is marginal for 248 nm and 193 nm photodissociation. Ondrey et al. [92] and Jacobs et al. [93] reported an upper limit of 5% for $P\left(v''=1\right)/P\left(v''=0\right)$ with 193 nm photolysis. The rotational distributions obtained in these two studies, however, showed signs of rotational relaxation since these distributions were cooler than what Jacobs et al. [84] later reported. The latter study reveled that 83% of the energy available turns into translation, 16% goes into rotation and 1% ends up as vibrational excitation. They were also able to reproduce the spectra by Ondrey et al. [92] and Jacobs et al. [93] by increasing the pressure from 5 mTorr to 100 mTorr.

The high level of translational energy of the OH photofragments corresponds to a recoil speed of 3700 m/s for 266 nm photolysis [79]. This result has impact on practical diagnostics applications. For imaging, it is customary to form laser sheets, having widths around 100 μm. In addition, it is often necessary to have a rotational population in thermal equilibrium, which means that the photofragments must not be probed promptly following dissociation. Without collisions it would take only 13.5 ns for an OH fragment moving at 3700 m/s to travel 50 μm and end up outside the probe volume. Experimental work performed within the current thesis has been performed at atmospheric pressure; thus, collisions keep the generated OH fragments within the probe volume for a significantly longer period of time.

Two-photon photodissociation of H_2O_2 has been investigated by Gölzenleuchter et al. [94] for 248 nm and 193 nm as well as by Klee and coworkers [95] for 266 nm and 193 nm. While the former group detected OH(A $\rightarrow$ X) fluorescence only for 193 nm photolysis, the latter observed it for both 266 nm and 193 nm. At laser fluences below 0.1 GW/cm^2 their power-dependence results clearly indicate a two-photon processes. At higher fluences the power-dependences became linear due to bleaching, i.e. photolysis saturation, of the ground state H_2O_2. The authors of both studies used nanosecond laser pulses, and since an upper limit for the lifetime of the $\tilde{A}^1$A state is 60 fs [79], Klee et al. [95] reasoned that nanosecond pulses can be viewed in the continuous-wave limit. Accordingly, rate equations were used to model the two competing processes, i.e. generation of two ground state OH molecules from single photon absorption and formation of OH (A) + OH (X) following two-photon absorption. Klee et al. [95] determined the absorption cross section for the second photon to be in the range $1\cdot10^{-16}-5\cdot10^{-16}$ cm^2 at 266 nm and roughly 60 times lower at 193 nm. The lower value obtained at 193 nm is taken as an indication that the OH(A) production quantum yield decreases with increasing photon energy for the benefit of other, non-fluorescing fragments. Nevertheless, the relatively high absorption cross sections for absorption of the second photon should be compared with the lifetime of the $\tilde{A}^1$A state. It then follows that the fluence needed at 266 nm for the two rates to be equal is 30 GW/cm^2, i.e. roughly 1.5×10^2 J/cm^2 for a 5 ns laser pulse. Considering that the single-photon absorption cross section for H_2O_2 is 4.02×10^{-20} cm^2 at 300 K and 266 nm [76], such a high fluence is expected to give a saturation level of virtually 100% regarding the absorption process of the first photon.

Chapter 4

Laser-induced fluorescence

Laser-induced fluorescence is the process when laser radiation is absorbed by atoms or molecules, which then spontaneously undergo transitions to lower levels under the emission of radiation. Laser-induced fluorescence is an important and widely used optical measurement technique, discussed in several review articles, see e.g. [26, 96–100]. This chapter briefly describes LIF applied for OH detection. It also includes a section about fluorescence lifetime imaging, which in many cases is important for quantitative 2D LIF measurements.

4.1 OH LIF

Laser-induced fluorescence via the first excited electronic state $\left(A^2\Sigma^+\right)$ is the main laser-based method for OH detection in gas phase. Figure 4.1 shows the LIF scheme applied for OH measurements in the experimental work on which this thesis is based. The OH molecules are initially in the ground vibrational state of the electronic ground state $\left(X^2\Pi\right)$. Photons are absorbed near 282 nm (upwards vertical arrow), bringing molecules from rotational level i to level j in the first excited vibrational level in the $A^2\Sigma^+$ electronic state (rotational levels are not indicated in the figure except for the levels between which transitions have been drawn). There are no strict rules on how the vibrational quantum number, v, may change during an electronic transition. According to the Frank-Condon principle, the electronic part of the electric dipole operator is independent of the internuclear separation [101]. Thus, when a transition takes place between different electronic states, the transition strength depends on the overlap of the vibrational wave functions of the two states. For OH, the internuclear separation is almost the same in the electronic ground state and the first excited electronic state (see figure 4.1). Hence, the transition strength from $v'' = 0$ decreases rapidly with increasing v' [102]. Accordingly, excitation is most commonly done either between $A^2\Sigma^+\,(v' = 0) \leftarrow X^2\Pi\,(v'' = 0)$ or $A^2\Sigma^+\,(v' = 1) \leftarrow X^2\Pi\,(v'' = 0)$. Following excitation to a specific quantum level, collisions will lead to vibrational (VET) as well as rotational energy transfer (RET). These processes will bring molecules from the selectively pumped level to nearby rotational and vibrational levels. Figure 4.1 shows fluorescence emitted (downward vertical arrow) from rotational level k in $A^2\Sigma^+\,(v' = 0)$ to rotational level m in $v'' = 0$ of the ground electronic state. Fluorescence emitted between these levels has a wavelength around 309 nm. However, in reality several excited quantum states will be populated due to VET and RET. Hence, fluorescence will be emitted from several rotational levels in both $A^2\Sigma^+\,(v' = 0)$ and $A^2\Sigma^+\,(v' = 1)$, and emitted fluorescence will be of many different wavelengths. The disadvantage of exciting OH molecules from $X^2\Pi\,(v'' = 0)$ to $A^2\Sigma^+\,(v' = 1)$ is that the transition strength is significantly weaker than if the corresponding transition in the $v' = 0 \leftarrow v'' = 0$ band had been pumped. However, since VET brings molecules excited to $v' = 1$ down to $v' = 0$ before they emit fluorescence, the majority of the spontaneously emitted fluorescence will be Stokes shifted roughly 27 nm with respect to the excitation laser wavelength. Hence, laser-stray light is quite easily removed using spectral filtering.

Also shown in figure 4.1 is the repulsive $^4\Sigma^-$ state. There are three repulsive electronic states crossing the $A^2\Sigma^+$ state, but only one has been included in the figure to preserve clarity. For a recent publication regarding OH potentials, see [103]. Due mainly to spin-orbit interaction in the crossing region, molecules may cross over from the $A^2\Sigma^+$ state to the repulsive states [106]. This phenomenon is referred to as predissociation, and it is indicated by P in the figure. Interaction with the $^4\Sigma^-$ state starts for high rotational quantum numbers of the $v' = 0$ and $v' = 1$ levels, while for $v' = 2$ all rotational levels are predissociative [107]. Due to high rates of predissociation, the radiative lifetimes decrease. Low lying rotational levels of the $v' = 2$ state have radiative lifetimes (~150 ns), which are roughly 5-6 times shorter than the lifetimes of the corresponding rotational levels in the $v' = 0$ and $v' = 1$ states (~750-1000 ns) [107]. Regarding $v' = 3$, radiative lifetimes are on the order of 100 ps [108, 109]. Also levels of low rotational quantum numbers in $v' = 0$ and $v' = 1$ exhibit predissociation, although marginal, due to coupling with the vibrational continuum of the $X^2\Pi$ state [110].

Apart from predissociation, which is almost non-existing for low rotational quantum numbers in $A^2\Sigma^+\,(v' \leq 1)$, the excited molecules are affected by collisional quenching (indicated by Q in figure 4.1). It means that due to collisions, excited molecules will de-excite without emitting radiation. The amount of collisional quenching is thus dependent on the collision environment and thereby parameters such as temperature, pressure and ambient species composition. Collisional quenching will affect OH in the $v' = 0$ and $v' = 1$ states, resulting in shorter lifetimes of the excited states and a decrease in fluorescence intensity. The fraction of excited molecules that fluoresce is called the fluorescence quantum yield, ϕ. If excitation is done to $v' = 0$ or $v' = 1$, the fluorescence quantum yield is approximately given by $\phi = A/\left(A + Q\right)$ in the linear LIF regime. It is important to point out that collisions will also affect the ground state rotational population. If the time duration of the exciting laser pulse is long compared to the time of RET within the current vibrational level of the ground state, the rotational level from which excitation is being done will be repopulated during the laser pulse by RET [111].

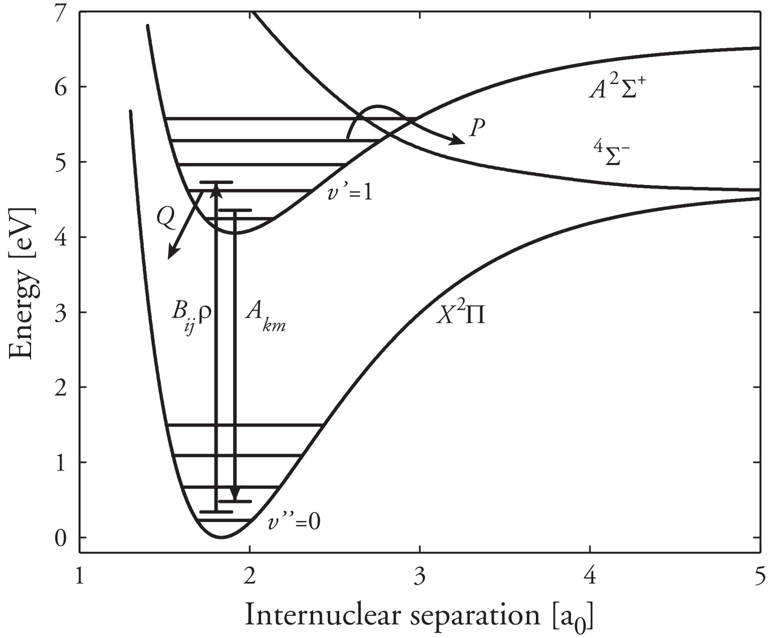

Figure 4.1: *The ground state potential of OH and the potentials of the* $A^2\Sigma^+$ *and* $^4\Sigma^-$ *states along with the lowest lying vibrational levels. Rotational levels are not shown. The arrow directed upwards indicates absorption of a photon near 282 nm, i.e.* $X^2\Pi\,(v''=0) \rightarrow A^2\Sigma^+\,(v'=1)$, *and the arrow directed downwards illustrates fluorescence emitted from* $v' = 0$ *in the* $A^2\Sigma^+$ *state to* $v'' = 0$ *in the ground state.* $B_{ij}\rho$ *is the rate of absorption from rovibronic level* i *to rovibronic level* j. A_{km} *is the rate of spontaneous emission from rovibronic level k with the molecule ending up in rovibronic level* m *following emission. Q and P indicate the collisional quenching and predissociation, respectively. Note that the potentials of the* $X^2\Pi$ *and* $A^2\Sigma^+$ *states are approximate Morse curves and are just intended as illustrations. Hence, the energy and internuclear separation scales are not exact. The* $^4\Sigma^-$ *potential has been approximately drawn with the results of van der Loo and Groenenboom [103] as the model. The internuclear separation is given in the unit of Bohr radius,* $1a_0 \approx 5.29 \cdot 10^{-11}$*m. Molecular constants used for the* $X^2\Pi$ *and* $A^2\Sigma^+$ *potentials were taken from Herzberg [104] and Luque and Crosley [105].*

4.2 OH-rotational structure

The ground state of OH is labeled $X^2\Pi_{3/2,1/2}$ and its two spin components give rise to two rotational energy ladders, termed F_1 and F_2, starting from total angular momentum quantum number $J = 3/2$ and $J = 1/2$, respectively [104]. For low values of J, Hund's coupling case (a) (see figure 4.2) is a good approximation. It means that both the orbital angular momentum of the electrons, $\boldsymbol{L}$, and the electronic spin, $\boldsymbol{S}$, precess about the internuclear axis. Their projections on this axis, $\boldsymbol{\Lambda}$ and $\boldsymbol{\Sigma}$, respectively, thus couple and form the well-defined vector $\boldsymbol{\Omega}$. If $\boldsymbol{R}$ represents the rotational angular momentum of the nuclei, the total angular momentum excluding nuclear spin is $\boldsymbol{J} = \boldsymbol{R} + \boldsymbol{\Omega}$. With increasing J, the rotational velocity of the molecule will become comparable to the precession velocity of the spin about the internuclear axis. As J increases, the spin will uncouple from the internuclear axis and $\boldsymbol{\Omega}$ will no longer be defined. $\boldsymbol{J}$ is then formed by adding $\boldsymbol{S}$ and $\boldsymbol{N} = \boldsymbol{R} + \boldsymbol{\Lambda}$, i.e. $\boldsymbol{J} = \boldsymbol{N} + \boldsymbol{S}$. This coupling scheme is called Hund's case (b) and it will be used from now on also for low J values, since the formalism can be applied even though $\boldsymbol{N}$ lacks any physical meaning. For a more thorough review of Hund's coupling cases and spin uncoupling, see the works by Herzberg [104] and Brown and Carrington [112].

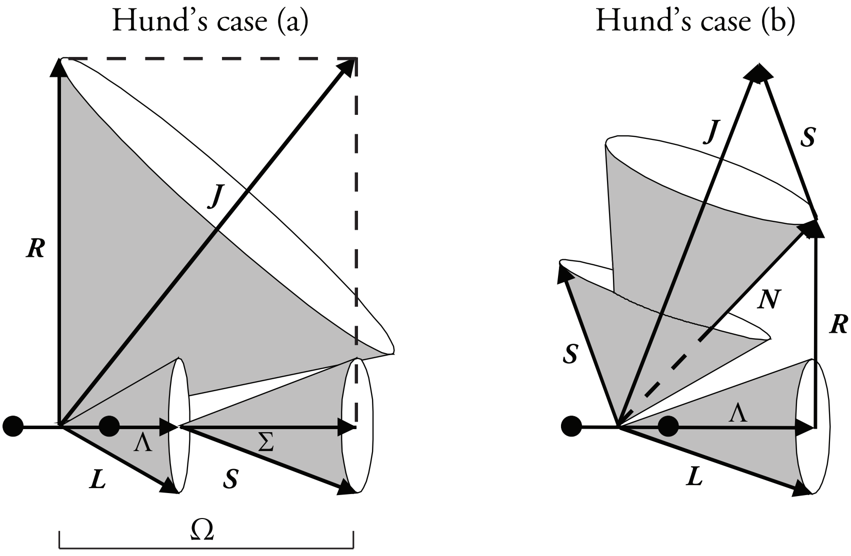

Figure 4.2: *Left: Hund's coupling case (a). The electronic orbital angular momentum, $\boldsymbol{L}$, is coupled to the internuclear axis by electrostatic forces, and the electronic spin angular momentum, $\boldsymbol{S}$, couples to $\boldsymbol{L}$ via spin-orbit coupling. The projections of $\boldsymbol{L}$ and $\boldsymbol{S}$ on the internuclear axis (Λ and Σ, respectively) are well defined. They form the vector $\boldsymbol{\Omega}$, which is vector added to the nuclear rotational angular momentum, $\boldsymbol{R}$. The resultant is $\boldsymbol{J}$, the total angular momentum excluding nuclear spin. Right: Hund's coupling case (b). The spin vector, $\boldsymbol{S}$, is not coupled to the internuclear axis and $\boldsymbol{\Omega}$ is not defined. $\boldsymbol{L}$ precesses about the internuclear axis and the projection, Λ is well defined. The vector $\boldsymbol{\Lambda}$ couples to the nuclear rotational angular momentum, $\boldsymbol{R}$, and they form $\boldsymbol{N}$. $\boldsymbol{S}$ and $\boldsymbol{N}$ are coupled to form $\boldsymbol{J}$.*

Figure 4.3 shows the seven lowest rotational levels of the two energy ladders (F_1 and F_2) for the OH ground state. Molecular constants were taken from [113]. Since the spin-orbit coupling constant is negative [113, 114], the term value of the $X^2\Pi_{3/2}$ level is lower than that of the $X^2\Pi_{1/2}$ level [104].

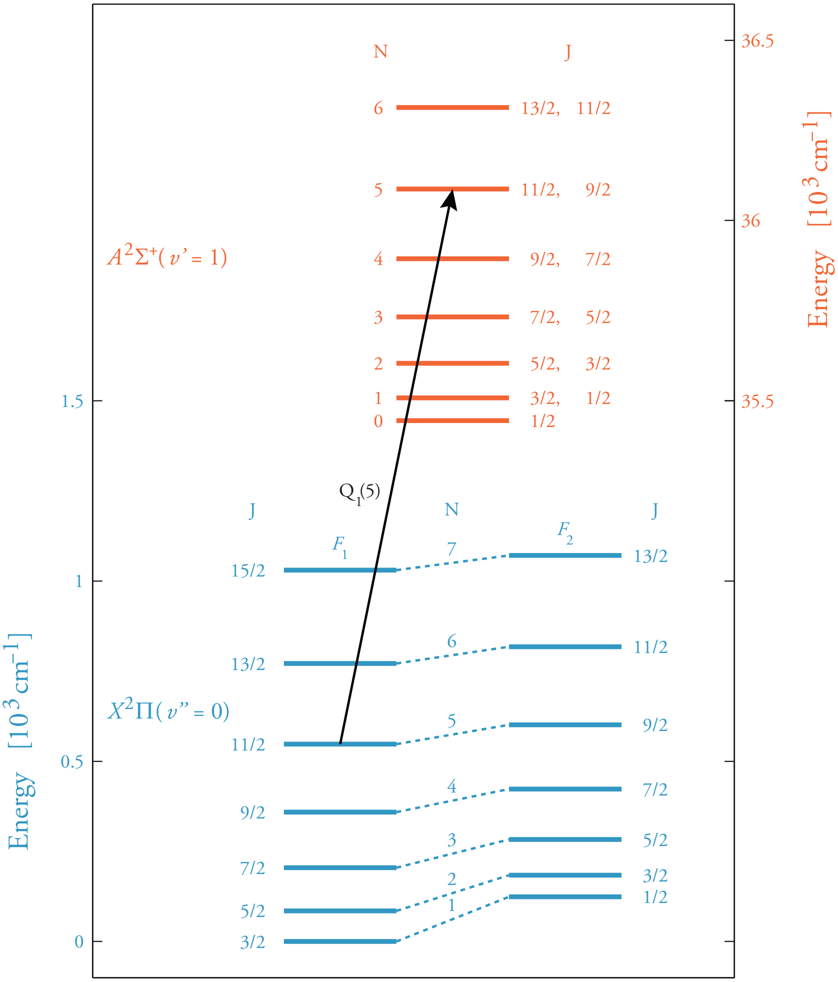

Figure 4.3: *Rotational energy levels of the* $X^2\Pi(v'' = 0)$ *and* $A^2\Sigma^+(v' = 1)$ *states of OH. The* $Q_1(5)$ *transition is indicated by an arrow.*

It is seen in figure 4.3 how energy levels with equal N values in the two ladders get closer with increasing spin uncoupling, while levels with equal values of J separate as the uncoupling increases. This phenomenon can be understood from the following two formulas for the rotational term values [104, 115, 116]:

$$F_1(J) = B_v\left(\left(J+\frac{1}{2}\right)^2 - \Lambda^2 - \frac{1}{2}\sqrt{4\left(J+\frac{1}{2}\right)^2 + Y(Y-4)\Lambda^2}\right) - D_vJ^4 \quad (4.1)$$

$$F_2(J) = B_v\left(\left(J+\frac{1}{2}\right)^2 - \Lambda^2 + \frac{1}{2}\sqrt{4\left(J+\frac{1}{2}\right)^2 + Y(Y-4)\Lambda^2}\right) - D_v(J+1)^4 \quad (4.2)$$

In equations 4.1 and 4.2 B_v denotes the rotational constant, D_v the centrifugal distortion constant and $Y = A_v/B_v$, where A_v is the spin-orbit coupling constant. The values of B_v, D_v and A_v depend on the vibrational level and the word constant might thus be somewhat misleading. They are generally Taylor expanded and calculated using the following formulas:

$$B_v = B_e - \alpha_e\left(v+\frac{1}{2}\right) + \gamma_e\left(v+\frac{1}{2}\right)^2 + \delta_e\left(v+\frac{1}{2}\right)^3 + \dots \quad (4.3)$$

$$D_v = D_e - \beta_e\left(v+\frac{1}{2}\right) + \dots \quad (4.4)$$

$$A_v = A_0 + A_1\left(v+\frac{1}{2}\right) + A_2\left(v+\frac{1}{2}\right)^2 + A_3\left(v+\frac{1}{2}\right)^3 + \dots \quad (4.5)$$

Also shown in figure 4.3 are the seven lowest rotational levels of the first excited vibrational level in the first excited electronic state, $A^2\Sigma^+$, (molecular constants taken from [105]). Since $\Lambda = 0$, there is only one energy ladder for the A state. The arrow in figure 4.3 illustrates the $Q_1(5)$ transition, which was used in several of the measurements reported on in this thesis.

4.3 Boltzmann population distribution of OH

The LIF process is initiated by absorption, and so it is important to excite from a rovibronic level which has a significant population in order to have a strong LIF signal. Hence, it is important to consider the distribution of molecules over the different quantum states. At thermal equilibrium, the vibrational population distribution follows Maxwell-Boltzmann statistics with degeneracy, $g_v = 1$. The number density of molecules in vibrational level v is thus proportional to the Boltzmann factor, $exp\left(-E(v)/(k_BT)\right)$, where $E(v)$ is the energy of vibrational level v, k_B is the Boltzmann constant and T is the temperature [104]. The fractional population in this level is given by (relative to zero energy vibrational ground-state):

$$\frac{N_v}{N} = \frac{e^{-E(v)/(k_B T)}}{1 + \sum_{i=1}^{\infty} e^{-E(i)/(k_B T)}} \tag{4.6}$$

In equation 4.6, N denotes the total population and the denominator of the right side is referred to as the vibrational partition function. A calculation yields that virtually the entire OH population is found in the lowest vibrational state at 300 K, with the population in $v = 0$ being several orders of magnitude larger than the populaton in $v = 1$. Even for a temperature of 2000 K, a calculation suggests that roughly 92% of the OH population is in the lowest vibrational level. Hence, for most practical diagnostic applications, it is sufficient to consider the rotational population distribution of the ground vibrational state.

Since each rotational level, J, has a degeneracy of $g_J = 2J + 1$, the population on level J in branch F_i is proportional to:

$$(2J+1)\, e^{-E_{F_i}(J)/(k_B T)}, \tag{4.7}$$

where $E_{F_i}(J)$ is the energy of that level. With N now being the total population in the lowest vibrational state, the fractional population on rotational level J in branch F_i is given by:

$$\frac{N_J^{F_i}}{N} = \frac{g_J e^{-E_{F_i}(J)/(k_B T)}}{\sum_m g_m e^{-E_{F_1}(m)/(k_B T)} + \sum_n g_n e^{-E_{F_2}(n)/(k_B T)}} \tag{4.8}$$

Λ doubling due to interaction between nuclear rotation and electron motion as well as splitting due to nuclear spin can be omitted. The Λ doubling will split each J level in two, and the nuclear spin of the hydrogen atom will split each energy level into two hyperfine components. Spectroscopically, Λ doubling is not observed in the experiments reported in this thesis. Accordingly, the even smaller hyperfine structure is not seen in these experiments. The total number of sublevels that each rotational energy level splits into due to Λ doubling and nuclear spin then appears both in the numerator and the denominator of equation 4.8. Hence, it will cancel.

Figure 4.4 shows the OH fractional populations on $J = 3/2$, $7/2$ and $11/2$ in the F_1 branch as functions of temperature. For the measurements presented in chapter 7, the $Q_1(5)$ transition was used, i.e. excitation was done from $J = 11/2$ in F_1 (see figure 4.3). The reason for choosing to excite from $J = 11/2$ in those measurements was not only to have a significant population over a broad temperature span, but also since this level has a population that does not vary too much over the temperature range of interest.

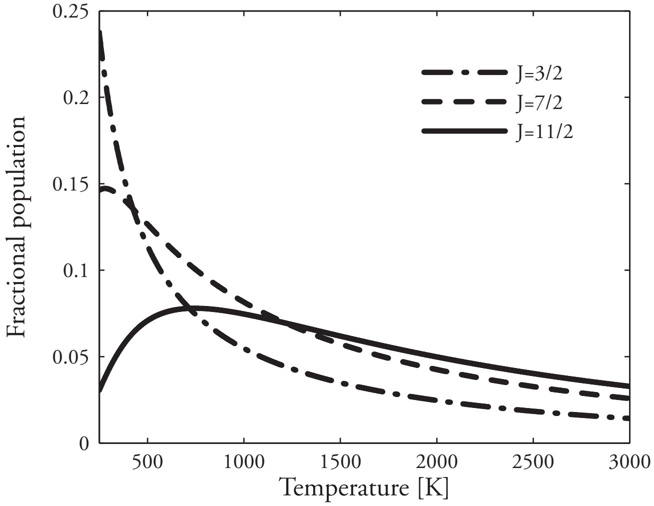

Figure 4.4: *Fractional populations on* $J = 3/2$, $7/2$ *and* $11/2$ *of the* F_1 *branch in the* $X^2\Sigma$ *state as functions of temperature.*

4.4 Fluorescence lifetime imaging

Among the strengths of LIF are imaging capacity, high sensitivity, possibility to provide high spatial and temporal resolution and that it is species specific in many measurements situations. However, despite the fact that emitted fluorescence intensity holds information about the concentration of the probed species, LIF is generally used as a qualitative measurement tool. One of the challenges with extending LIF to quantitative measurements is to determine the fluorescence quantum yield. Apart from collisions, which have already been mentioned, the fluorescence quantum yield is affected by stimulated emission, predissociation, photoionization and chemical reactions involving the excited molecules.

It is often desirable to record single-shot images and from these images be able to make rudimentary analysis of the concentration ratios between different parts of the images. Thus information about the fluorescence quantum yield is required. In combustion processes, collisional quenching is often the only important parameter affecting the fluorescence quantum yield. Approaches for LIF aimed at minimizing effects from collisional quenching are saturated LIF [15, 19], laser-induced predissociative fluorescence [111] and time-gated short pulse LIF [117]. The ideas behind saturated LIF and laser-induced predissociative fluorescence are to make stimulated emission and predissociation, respectively, the dominant loss mechanisms, thus allowing for collisional quenching to be neglected. With the time-gated short pulse technique, only the initial part of the fluorescence decay is measured. The idea is to measure on a time scale which is short enough to prevent collisions from affecting the signal to any significant extent.

However, in order to compensate entirely for fluorescence quantum yield differences, the temporal decay of the fluorescence signal should be measured.

Fluorescence lifetime imaging (FLI) includes several techniques, operating in either the time domain or the frequency domain [118]. They can be further divided into two groups depending on whether the image buildup is performed through imaging (wide field) or by scanning pixel-by-pixel (laser-scanning imaging). Common for all these techniques is that they spatially resolve and measure the excited-state lifetimes of a sample, thus showing spatial differences in energy transfer probabilities. Such information is not only of interest when performing quantitative LIF measurements. It can under certain circumstances be used to carry out quantitative pH measurements [119], measure quencher molecule concentrations [120, 121] as well as for thermometry [122].

In frequency-domain FLI, the excitation radiation is intensity modulated and the phase shift as well as demodulation of the emitted fluorescence in relation to the exciting radiation are measured [118]. Fluorescence lifetime imaging in the frequency domain inherently requires longer acquisition times than what could be obtained in the time domain. One advantage with frequency domain FLI compared to time domain FLI is that the former provides two lifetimes, one from the phase shift and one from the decrease in modulation depth. Fluorescence lifetime imaging in the time domain can be performed by stepping the time separation between excitation and signal recording. There are, however, more advanced schemes. Ni and Melton [122] used Ashworth's rapid lifetime determination (SRLD) algorithm [123]. This procedure has serious drawbacks, especially for short fluorescence lifetimes. The main limitations are that the SRDL algorithm is not valid for real camera gates since they are not square shaped, and, second, a certain choice of gate widths and gate time separation is only accurate for a limited range of fluorescence lifetimes.

Our research group has developed and tested a technique, which we designate DIME (Dual Imaging and Modeling Evaluation). It is a two-camera setup that allows single-shot 2D measurements of fluorescence lifetimes shorter than 1 ns. The details of the setup are found in papers I and II. Basically, the foundation of the technique is a thorough characterization of the experimental setup, so that experimental data can be evaluated by comparison with simulated signal ratios. The cameras need to be gated and the gate functions must be measured along with sensitivity differences between the two cameras. In order to measure short lifetimes accurately, it is also necessary to measure the time jitter between the exciting laser pulse and the camera gate functions. The signal I_i, where i is the camera index can be written:

$$I_i(\tau, t_i, \delta) = \int_{-\infty}^{\infty} S(t,\tau) G_i(t - t_i - \delta)\,\mathrm{d}t, \tag{4.9}$$

where t is time, τ is the fluorescence lifetime, t_i is the gate delay, δ is the time jitter, S is the fluorescence decay and G_i is the gate function. Denote $S(t,\tau)G_i(t - t_i - \delta)$ by

$W_i(t,\tau)$, and form the ratio $I_1/(I_1+I_2)$:

$$D = \frac{\int\limits_{-\infty}^{\infty} W_1(t,\tau)\,\mathrm{d}t}{\int\limits_{-\infty}^{\infty} [W_1(t,\tau)+W_2(t,\tau)]\,\mathrm{d}t}, \tag{4.10}$$

If S is assumed to follow a single-exponential decay, the following equation may be derived:

$$\frac{\mathrm{d}D}{\mathrm{d}\tau} = \frac{1}{\tau^2}\frac{\int\limits_{-\infty}^{\infty} W_1(t,\tau)\,\mathrm{d}t \int\limits_{-\infty}^{\infty} W_2(t,\tau)\,\mathrm{d}t}{(\int\limits_{-\infty}^{\infty} [W_1(t,\tau)+W_2(t,\tau)]\,\mathrm{d}t)^2}\left(\frac{\int\limits_{-\infty}^{\infty} tW_1(t,\tau)\,\mathrm{d}t}{\int\limits_{-\infty}^{\infty} W_1(t,\tau)\,\mathrm{d}t} - \frac{\int\limits_{-\infty}^{\infty} tW_2(t,\tau)\,\mathrm{d}t}{\int\limits_{-\infty}^{\infty} W_2(t,\tau)\,\mathrm{d}t}\right), \tag{4.11}$$

The two terms within parenthesis may be identified as the expectation values in time of W_1 and W_2, respectively. It is the difference in time of the temporal expectation values of the signals recorded by the two cameras that makes the ratio, D, a function of the fluorescence lifetime with determinate solutions. It is thus imperative that the gate functions of the two cameras are different so that the temporal expectation values of W_1 and W_2 do not coincide. We have shown that the optimal gate functions would be two ramped gain profiles, one with positive slope and one with negative slope. This choice of gate functions makes the algorithm equally sensitive to all fluorescence lifetimes. However, the DIME concept should always be used in order to compensate for deviations from the theoretical gate functions.

Since two cameras are used to obtain separate images of the same object, it is important that images recorded by the two cameras are properly overlapped before lifetime evaluation. For that purpose, two image overlap optimization algorithms, both based on simulated annealing [124, 125], were developed in connection with two image transform codes. The overlap algorithms operate on grid images recorded by the cameras prior to, or after a measurement. The first image-transformation program handles rotation, x and y translation, stretch in the x and y directions as well as compensation for barrel/pincushion distortion. The second transformation program performs higher order non-linear transformations in order to compensate for differences in the imaging optics, which can not be handled by the transformations included in the first program. The job of the two overlap optimization algorithms is to find optimal parameters for the two image-transform programs. The idea behind the optimization algorithms is to minimize the so called energy function, $E(\bar{r})$, which is quite naturally chosen to be the deviation between the grid images recoded using the two cameras. The vector $\bar{r}$ is the set of parameters, which are input variables for the image-overlap programs. Let $\bar{r}_0$ denote the vector containing initial values. A parameter is chosen randomly from $\bar{r}_0$, and it is subsequently randomly changed from its current value to a nearby value within certain limits. The grid image recorded with camera 1 is then transformed using the new set of parameters, $\bar{r}_1$. A new energy, $E\left(\bar{r}_1\right)$, is calculated by measuring the difference between the grid image obtained with camera 2 and the newly transformed grid image originally obtained with camera 1. If $E(\bar{r}_1) < E(\bar{r}_0)$, the new parameter is accepted with probability $P = 1$, and the optimum $\bar{r}$-vector, $\bar{r}_{min}$, is set to $\bar{r}_1$. A minimum energy, $E_{min} = E(\bar{r}_{min})$ is also defined. However, if $E(\bar{r}_1) > E(\bar{r}_0)$, the new parameter still has a chance of acceptance, the probability being given by:

$$P = e^{(E(\bar{r}_0) - E(\bar{r}_1))/T}, \tag{4.12}$$

where T is referred to as the temperature. It is a global, user-defined, time-dependent parameter. The probability given by equation 4.12 can very well be chosen in some other way, but it is important that there is a probability of accepting a change of a parameter even if it turns out this change increased the energy. The reason is that unless this probability exists, there is no way for the system to get out of local minima on its way towards the global minimum or at least a deep-lying local minimum. The process of randomly choosing a parameter to change and then change it randomly is repeated for a pre-set number of times or until the convergence criteria are reached. Each time a parameter change is accepted, the energy is saved. Whenever a newly calculated energy, E_{new}, is lower than the latest saved energy value, E_{new} is checked against E_{min} to see if the new parameter set is the optimal parameter choice found so far. The temperature, T, is decreased over the course of the iterations. Hence, the system starts off with a lot of thermal energy, but as the annealing process proceeds, the thermal energy decreases until the system freezes.

Chapter 5

Photofragmentation laser-induced fluorescence of H_2O_2

The following sections briefly go through photofragmentation of H_2O_2 followed by LIF on the generated OH photofragments. First some general considerations regarding this measurement technique are presented. It is followed by a section about how the technique can be used for quantitative concentration measurements. More details are given in the references and in the attached papers (III-V).

5.1 General considerations

Due to the lack of bound accessible excited electronic states, LIF based on electronic excitation cannot be directly applied on H_2O_2. However, the fact that photodissociation of H_2O_2 leads primarily to the formation of ground state OH, creates the possibility for photofragmentation followed by LIF detection of generated OH. Rogers et al. [126] were among the first to propose photofragmentation laser-induced fluorescence (PF-LIF) for detection of trace species. Since then, techniques based on photofragmentation followed by fragment detection have become well established [127, 128]. The PF-LIF scheme applied to H_2O_2 is illustrated in figure 5.1.

Since photofragments rather than parent molecules are probed, PF-LIF is an indirect measurement technique. This fact brings about advantages as well as disadvantages, depending on the measurement situation. For some systems, the generated fragments will induce chemistry, which, by performing time-resolved studies, can provide information which would otherwise be difficult to obtain. The pump-probe delay studies described in section 5.2 utilize the chemical consumption of OH to get around difficult calibration issues and quenching for quantitative H_2O_2 detection. For the measurements discussed in chapter 7, the non-species specificity of PF-LIF is negative since interfering signals become difficult to discriminate against since they are also from OH.

Photofragmentation laser-induced fluorescence can be performed using one or two lasers. If only one laser is used, that laser has to either directly generate photofragments

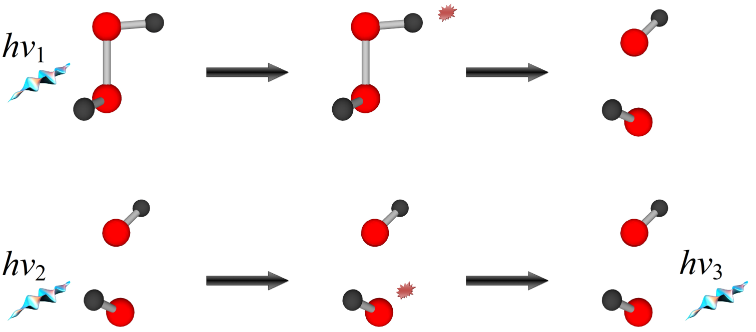

Figure 5.1: *Schematic illustration of PF-LIF applied to* H_2O_2*. A photon of frequency* ν_1 *excites an* H_2O_2 *molecule to a dissociative potential, and the molecule promptly dissociates into two OH fragments. A probe-pulse photon of frequency* ν_2*, tuned to an OH rovibronic transition, excites an OH fragment, and the molecule deexcites by emitting a fluorescence photon of frequency* ν_3*.*

in emissive excited states or first photodissociate the parent molecule and then excite the photofragments to emissive excited states. As was mentioned in section 3.2, Klee et al. [95] observed OH fluorescence from two-photon excitation of H_2O_2 using a single non-resonant laser at 266 nm as well as at 193 nm. Detection of OH generated from photolysis of H_2O_2 using a single laser for both photodissociation and excitation of the generated OH molecules has been performed in our group. Figure 5.2 shows two excitation scans obtained from a measurement where a single laser pulse ($\lambda = 281 - 285$ nm) was responsible for photodissociation as well as for inducing fluorescence from the generated OH. The two spectra were obtained using different pulse energies. Using a single laser for both photodissociation and excitation of the photofragments means that the laser-profile overlap for photodissociation and subsequent excitation is perfect. However, the observed signal will most likely not originate from a population in thermal equilibrium and power broadening may be significant if high power is required for the photolysis process.

For studies of H_2O_2 there are two principal reasons for using two lasers in a pump probe fashion. The main reason is that unless multi-photon absorption is induced, wavelengths in the vacuum ultraviolet (VUV) are needed in order to generate excited OH directly from photolysis of H_2O_2. Otherwise the photodissociation pulse must also excite the photofragments. The second reason for choosing a two-laser setup is that it enables pump-probe delay measurements, in which the PF-LIF signal is probed as function of the delay time between the two laser pulses.

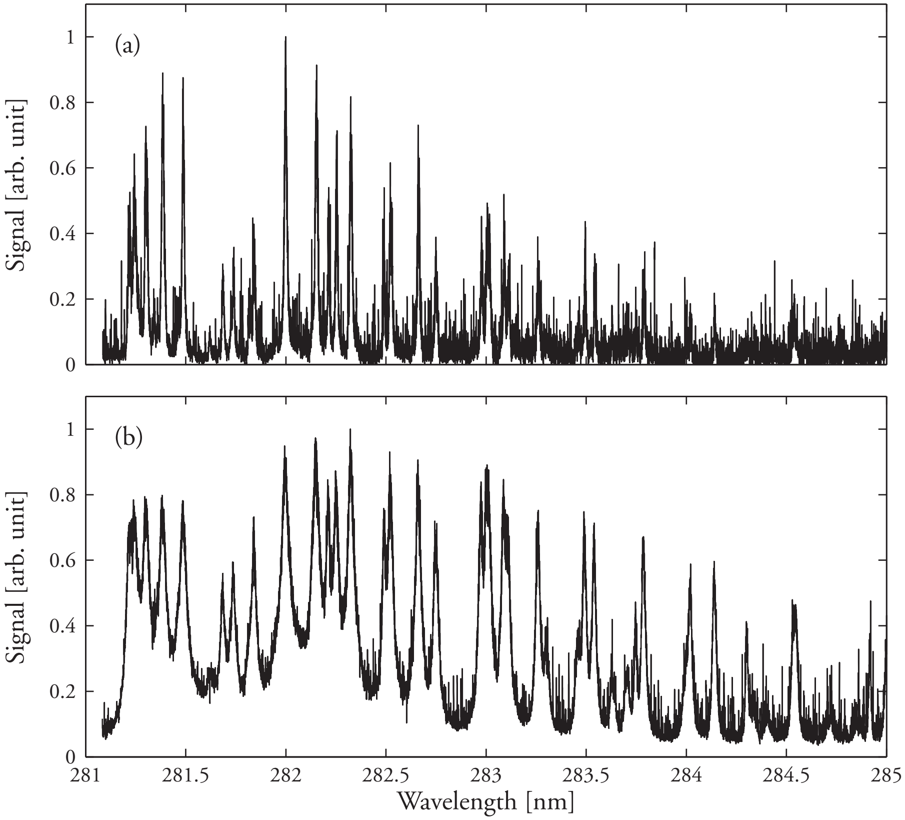

Figure 5.2: *Two excitation scans of OH photofragments recorded using a single laser for photodissociation as well as for excitation of generated OH fragments. (a) Excitation scan recorded with a fluence on the order of 50 mJ/cm^2. (b) Excitation scan recorded with a fluence around 750 mJ/cm^2.*

5.2 Photofragmentation laser-induced fluorescence pump-probe delay studies

It is convenient to take the following reaction as a starting point for this section:

$$OH + H_2O_2 \xrightarrow{k_1} HO_2 + H_2O \tag{1}$$

Reaction 1 has been thoroughly investigated since the 1980's [129–138], in a large part due to its importance as an atmospheric destruction mechanism for H_2O_2 and OH. The recommended value for the reaction rate constant, k_1, is $2.9 \cdot 10^{-12} e^{-160/T}$ cm^{3}molecule^{-1}s^{-1} in the temperature range 240-460 K [139]. Naturally, reaction 1 will also be important for the OH decay following photodissociation of H_2O_2 in systems made up of mixtures of H_2O_2 with buffer gases such as H_2O, He, N_2, Ar and O_2. If the fluorescence quantum yield does not change over the measurement time period, the decay of the integrated fluorescence signal as a function of the pump-probe delay time depends solely on chemical reactions and transportation. Considering only reaction 1 and assuming the H_2O_2 concentration to be high enough to be approximately constant, the OH consumption would follow a single exponential decay.

$$[\mathrm{OH}] = [\mathrm{OH}]_0 e^{-(k_1[\mathrm{H_2O_2}]+k_d)t} = I_0 e^{-t/\tau}, \tag{5.1}$$

where k_d is a rate constant for OH removal processes in the absence of H_2O_2, i.e. diffusion and gas flow. This pseudo-first order kinetic expression is valid for low photolysis levels. The photolysis level is a measure of the fraction of H_2O_2 molecules in the probe volume that have been photodissociated by the photolysis laser pulse, i.e. a parameter ranging from zero to unity. When the photolysis level is increased, reaction 1 alone will not suffice to describe the chemical decay of OH. The fraction of photodissociated H_2O_2 molecules can be estimated using the the following equation [140]:

$$\frac{N_{di}}{N} = \left(1 - e^{-(\sigma F)/(h\nu)}\right), \tag{5.2}$$

where N_{di} is the number density of dissociated H_2O_2 molecules, N the initial number density of H_2O_2, σ the temperature and wavelength-dependent absorption cross section, F is the laser fluence, h is the Planck constant and ν is the photon frequency at the photolysis wavelength.

Our group has investigated the OH chemical consumption as a function of the photolysis level (Paper V). We used a bubbler flask containing different concentrations of liquid H_2O_2/H_2O mixtures. The bath gas was N_2. It was verified prior to measurements that the equilibrium vapor pressure of H_2O_2 was obtained by recording a PF-LIF signal versus N_2-flow rate curve. The N_2 flow rate was then kept in a region where moderate changes did not affect the PF-LIF signal. Data recorded during this campaign showed that first-order exponential decays approximated the OH consumption rather well even for photolysis levels that began to fall outside the region where pseudo-first order chemistry could be assumed. However, in order to predict the change in the decay time, τ, observed from single-exponential fits to experimental data obtained at different photolysis levels, a mechanism including the 14 reactions listed in Table 1 of Paper V was created. Figure 5.3 illustrates how the decay time changes with increasing photolysis level.

A sensitivity analysis for the studied system suggested that the mechanism can be reduced to include only 4 reactions virtually without losing any accuracy. As well as reaction 1, the following 3 reactions need to be included:

$$\mathrm{OH + OH + M \longrightarrow H_2O_2 + M} \tag{2}$$

$$\mathrm{OH + OH \longrightarrow H_2O + O} \tag{3}$$

$$\mathrm{OH + HO_2 \longrightarrow H_2O + O_2} \tag{4}$$

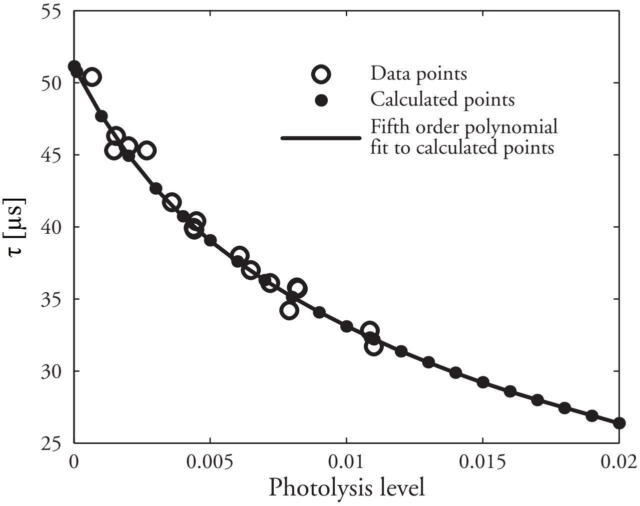

Figure 5.3: *Decay time of the OH photofragments as a function of the photolysis level for an initial* H_2O_2 *number density of* $1.16 \cdot 10^{16}$ cm^{-3}.

Figure 5.4 shows the PF-LIF signal recorded as a function of the delay time between the photolysis pulse and the probe pulse at 296 K and with an initial H_2O_2 concentration of roughly 470 ppm (number density $1.16 \cdot 10^{16}$ cm^{-3}). Also shown in the figure is a fitted single exponential. The lifetime of this fitted curve is around 32 μs, which should be compared to the lifetime $\tau = 51$ μs suggested by eq. 5.1 with $k_d = 0$. The deviation from the fitted single-exponential function is clearly seen for pump-probe delay times larger than 150 μs. This deviation is predicted by the 14 reaction chemical kinetic mechanism. Even though the single exponential is within the single-shot error bars (1 standard deviation), the trend of the data points, which show the average value from 300 single shots, follows the calculated curve.

Whenever PF-LIF pump-probe delay measurements are used for quantitative extraction of H_2O_2 concentrations, it is preferable to use sufficiently low photolysis fluence to operate in the pseudo-first order kinetic regime where reaction 1 governs the decay. A PF-LIF sensor operating in this regime does not require any calibration, but temperature has to be measured in order to use the correct value of k_1. Nevertheless, there may be situations when low signal levels make it necessary to apply higher photolysis levels. It is then still possible to approximate the signal decays as single exponential decays with H_2O_2 concentrations increasing linearly with $1/\tau$; however, the rate constant, k_1, will not apply. Instead an effective rate constant has to be used. This effective rate constant is not found in the literature since it is not connected to any elementary reaction. Hence, operation in the non-pseudo first order kinetic regime requires calibration or mapping of the effective rate constant as a function of both photolysis fluence and temperature.

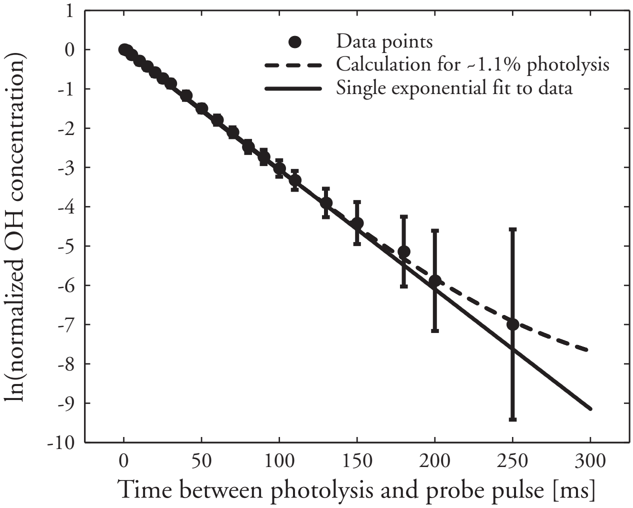

Figure 5.4: *Hydroxyl-photofragment decay as a function of the pump-probe delay time for an initial* H_2O_2 *number density of* $1.16 \cdot 10^{16}$ cm^{-3} *and a photolysis level of roughly 0.011.*

Photofragmentation laser-induced fluorescence measurements of OH chemical consumption can be performed in a point, along a line or in 2D. For line and 2D measurements, a camera is needed for detection, while a PMT suffice for point measurements. It is important to point out that if line measurements or 2D measurements are performed, it does not matter if the fluorescence quantum yield is not uniform in the probe volume. As long as the fluorescene quantum yield does not change during the measurement time, pump-probe delay studies are unaffected since it is the chemical consumption of OH, not the absolute signal strength, that is relevant.

To induce fluorescence from OH, either a pulsed or a continuous-wave source can be used. If the PF-LIF technique is to be applied as a point sensor, it would make sense to use a continuous or high repetition rate source for excitation in combination with a PMT. If a standard 10 Hz dye laser system is used as in the experiments presented in papers V and VI, it will take several minutes to acquire around 15-25 measurement points recorded with different pump-probe delay times using some averaging. Such a long acquisition time makes the measurement prone to errors arising due to fluctuations and drift in the gas-phase H_2O_2 concentration. With a continuous-wave OH excitation source, a complete OH-signal decay curve could be obtained on the time scale of 1 μs - 1 ms depending on the H_2O_2 concentration. Since the entire OH-signal decay is obtained for every photolysis pulse, it would be a much faster method even with averaging compared to stepping up the signal decay point by point using pulsed detection. The alternative would be to use a probe laser with very high repetition rate. Parker et al. [11] used a 10 kHz dye laser for OH photofragment LIF. While this repetition rate is sufficient for many applications, the high H_2O_2 concentrations used in industrial applications demand repetition rates in the MHz range.

Currently, the possibilities of making a point sensor with continuous-wave excitation of OH are limited due to the lack of cheap, mobile lasers emitting continuous wave around the (0,0) or (1,0) band of OH. There are UV diodes available in both these wavelength regimes, and there are plans for testing their applicability. The concern is, however, whether the signal induced by a diode will be sufficiently intense even with lock-in detection.

Chapter 6

Rig measurements

This chapter deals with measurements performed in two test rigs at Tetra Pak Packaging Solutions AB in Lund, Sweden. Geometrically the measurement chambers of the two test rigs are almost identical. However, in one of the rigs, measurements are performed in vaporized H_2O_2/H_2O solutions mixed with hot air (gas rig) while in the other rig (water rig) measurements are performed in liquid H_2O which has been mixed with Rhodamine 590 (Rh590). From a reliability point of view it is preferable to perform measurements in the gas rig since it mimics real gas-phase H_2O_2 sterilization applications. However, experimentally there are several advantages to measuring in the water rig instead of in the gas rig. The five main aspects are; substantially higher signal, no photodissociation required, a fixed-frequency laser can be used, the flow is slower at the same Reynolds number (Re), which means that adequate time resolution is easier to obtain, and health hazards are at a minimum. Therefore, a significant challenge is to compare the flow situations in the two rigs in order to check whether differences in results obtained from measurements performed in these two rigs can be neglected.

Section 6.1 briefly goes through the PF-LIF setup used for the gas rig measurements. It is followed by a section (6.2) describing the gas rig. In section 6.3 injection studies are presented. It is divided into two parts, where the first part includes visualization experiments performed only in the gas rig. The second part explains 2D imaging carried out in both the gas rig and the water rig with the aim of having the same Re for the flow situations in the two rigs. The Re is given by UL/ν, where U is a characteristic speed of the system, L a characteristic length and ν is the kinematic viscosity. The last section (6.4) of this chapter deals with quantitative concentration measurements performed only in the gas rig. In the short perspective, the goal with this latter study was to validate the PF-LIF technique against other H_2O_2 sensors. In a longer perspective, PF-LIF might be used as a reference tool.

6.1 Photofragmentation laser-induced fluorescence experimental setup

Figure 6.1 shows an overview of the experimental setup used for PF-LIF measurements in the gas rig. Photofragmentation of H_2O_2 was performed using the output from a pulsed Nd:YAG laser, equipped with a fourth harmonic (266 nm) frequency conversion unit. The repetition rate of this laser is 10 Hz, and the maximum pulse energy at 266 nm is roughly 80 mJ. The pulse duration is about $\sim$5 ns. The photolysis pulses were directed through a variable attenuator consisting of a half-wave plate, held by a mount allowing precise rotation, followed by a polarizing beam splitter cube. This configuration allowed the pulse energy of the photolysis laser to be varied from virtually zero to around 80 mJ. This feature is crucial for a setup that should be practical in industrial applications since it is important to be able to use the PF-LIF setup for quantitative concentration measurements, generally requiring low photolysis-pulse energies, but it is also important to be able to apply high photolysis-pulse energies for qualitative imaging applications.

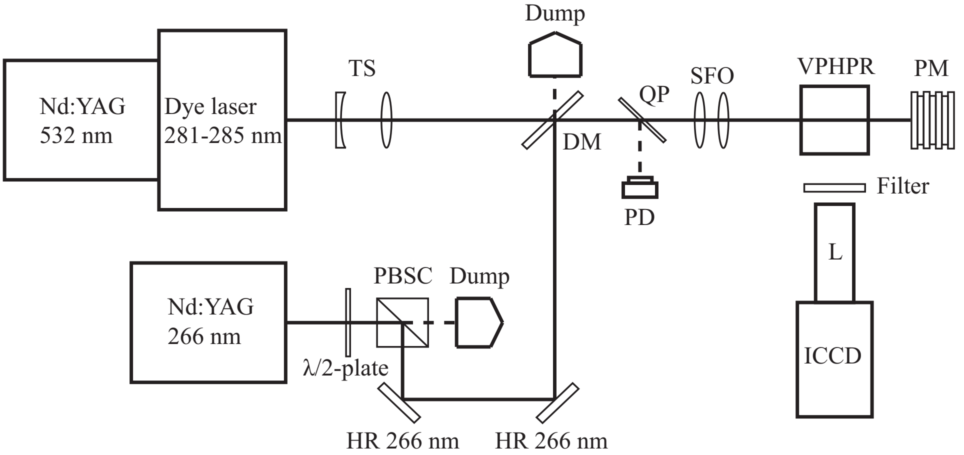

Figure 6.1: *Experimental setup used for the PF-LIF measurements in the gas rig. The abbreviations denote: TS; telescope, PBSC; polarizing beam-splitter cube, HR; high reflectivity, DM; dichroic mirror, QP; quartz plate, PD; photodiode, SFO; sheet-forming optics, VPHPR; vapor-phase H_2O_2 rig (gas rig), L; camera lens, ICCD; intensified CCD camera, PM; power meter.*

A frequency-doubled dye laser, operating with Rh590 was used for inducing OH fluorescence. The dye laser was pumped by the second harmonic radiation (532 nm) of an Nd:YAG laser. The pulse energy of the frequency-doubled output from the dye laser was roughly 8 mJ. The actual pulse energy from the dye laser depends on the dye concentrations used, and it is possible to obtain higher pulse energies than 8 mJ from this laser. However, it was considered enough for the measurements that were undertaken. The dye beam was attenuated as needed using color glass filters (Schott). Also, the dye-laser system had a repetition rate of 10 Hz, and the output was frequency tuned to excite the combined $Q_1(1) + R_2(3) + Q_{21}(1) + S_{21}(22)$ transition $\mathrm{OH}\left(A^2\Sigma^+\right) v' = 1 \leftarrow \mathrm{OH}\left(X^2\Pi\right) v'' = 0$ near 282.0 nm. Detection was performed undispersed in the $\mathrm{OH}\left(A^2\Sigma^+\right) v' = 0 \rightarrow \mathrm{OH}\left(X^2\Pi\right) v'' = 0$ band around 309 nm using an ICCD camera equipped with a UV lens ($f/2$). An interference filter centered at 310.5 nm with a bandpass of 11.5 nm was used together with a Schott WG 305 and a Schott UG 11 filter in front of the camera lens in order to reduce interferences.

The laser beams were expanded and focused to vertical sheets using different lenses. The actual lenses used differed depending on the application. The lens used to focus the beams to sheets typically had a focal length of 500 mm. The laser-sheet heights were roughly between 20-45 mm. Pump and probe-laser beam spatial overlap was adjusted prior to each measurement by monitoring the PF-LIF signal while translating the photolysis pulse horizontally until maximum signal was obtained. The overlap of the two beams was handled by a dichroic mirror with high reflectivity at 266 nm and high transmission between 281-285 nm. The time separation between consecutive photolysis and probe laser pulses was monitored using a photodiode connected to a digital oscilloscope. The two lasers as well as the camera gate were triggered through an external delay/pulse generator, which allowed precise adjustments of the pump-probe delay time.

6.2 Gas rig

Tetra Pak Packaging Solutions AB has developed and built a prototype test rig to be used as a starting point for development and testing of gas-phase H_2O_2 measurement techniques as well as for obtaining basic knowledge about fluid dynamics. An illustration of the gas rig is shown to the left in figure 6.2. It has an enclosed supply tank (not shown in the figure) from which a 35% (weight) H_2O_2/H_2O liquid solution is pumped via a smaller vessel to a spray nozzle. This nozzle injects the H_2O_2/H_2O solution into an evaporator where it is mixed with air heated to about 350 K. The evaporator, which is not shown in figure 6.2 consists of a perforated aluminum block which is heat regulated with the heating rods set to roughly 450 K. The mixture of hot air and vaporized H_2O_2/H_2O goes via inlet (I) in the figure into a manifold (II) with four outlets. Three of these outlets are open all the time while the fourth outlet can be opened and closed using a pneumatically controlled piston. The piston is part (III) in the figure. The fourth outlet leads to a measurement chamber (IV) through an interchangeable nozzle. The manifold has been prepared with four ports (V), where sensors can be connected. The measurement chamber is seen in detail to the right in figure 6.2. It has two possible exits for the entering flow; one in the center of its back plate (VI) and one in the center of its bottom plate (VII). The back plate exit is connected to a valve that can be synchronized to close when the piston opens the chamber inlet port. It is thus possible to use the back-plate port as an inlet rather than an exit. This feature proved to be crucial

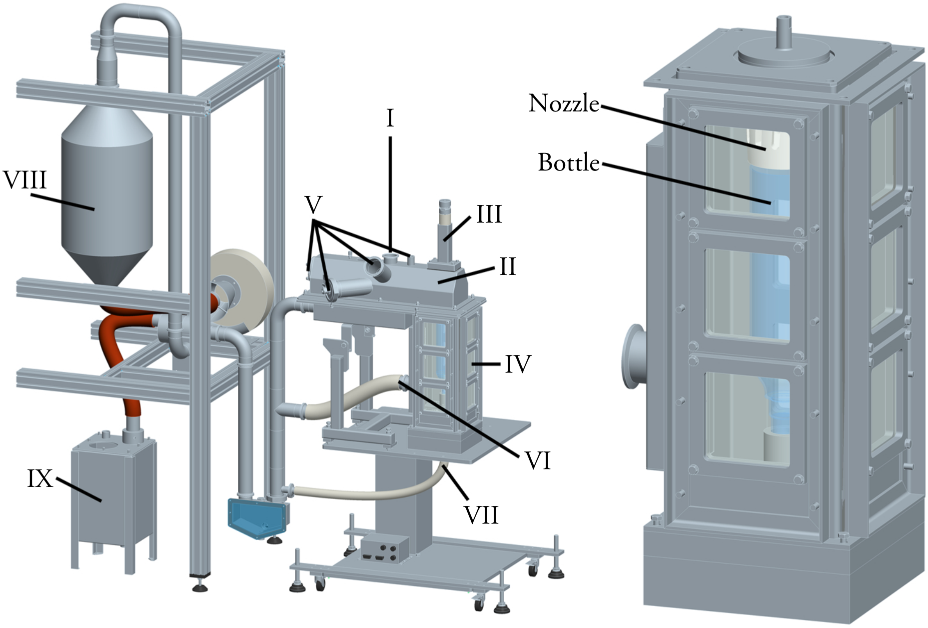

Figure 6.2: *Left: Illustration of the gas rig with the following parts indicated: (I); inlet for the vaporized* H_2O_2/H_2O*/air mixture from the evaporator down into the manifold, (II); manifold, (III); pneumatically controlled piston which opens and closes the inlet to the measurement chamber, (IV); measurement chamber, (V); ports for sensors to be connected, (VI); back-plate outlet/inlet, (VII); bottom-plate outlet, (VIII); catalytic destroyer, (IX); tank containing running water through which the gas from the catalytic destroyer is pushed. Right: Close-up view over the gas-rig measurement chamber with bottle and a nozzle. When this particular nozzle was used, a shield was placed around it to direct the return flow. This shield is not seen in the figure.*

for injection measurements. Since these measurements required the chamber inlet port to be initially closed in order to start the measurement with zero H_2O_2 concentration in the chamber, the heating of the chamber was insufficient to keep the chamber warm enough to prevent dew formation when the chamber inlet port was opened. The back-plate port was thus connected to a heated-air supply. The outlets of the manifold as well as the bottom-plate outlet of the measurement chamber are connected to a catalytic destroyer (VIII). The flow from the catalytic destroyer is pushed through a tank of running water (IX) before being exhausted.

The size of the chamber is 175 mm × 175 mm × 443 mm. It has optical access from the front as well as from its left and right sides. These sides consist of plastic plates with 3 square (100 mm × 100 mm) holes where quartz windows can be attached. Apart from mounting quartz windows, adaptors for different sensors can be attached in connection to the holes in the plates. It is thus possible to perform simultaneous measurements with several different sensors.

During the different measurement campaigns, the gas rig has had issues primarily with insufficient vaporization and stability. Measurements using absorption techniques have shown that the concentration fluctuations over a time period of a few minutes can be significant, depending on the running conditions.

6.3 Injection measurements

Images were recorded using the PF-LIF technique during injection of vaporized H_2O_2/H_2O/air mixtures into the measurement chamber. The pneumatically controlled piston was in its lower position, i.e. the inlet from the manifold to the chamber was closed, prior to measurement. It was verified experimentally that the measurement chamber did not contain any H_2O_2 before acquiring data. A specially designed triggering system was used. It allowed the lasers to run continuously, which is required in order to have the optimum pulse-to-pulse stability. When acquisition begins, trigger pulses synchronized with the probe-laser pulses are sent to the camera. After a user defined time period a trig pulse is sent and the piston, which then opens the chamber inlet. This system allows injection to be synchronized with the laser pulses and lets the camera record a couple of background images prior to injection.

Two different nozzles were used. The first one is a 66 mm long, 8 mm diameter vertical pipe. The pipe inlet is conically shaped, i.e. the pipe length is roughly 60 mm. The second nozzle has 6 angled ($7^\circ \times 7^\circ$) channels, each with 4 mm diameter. It is designed to be used for bottle sterilization. It is hollow in the center and has holes for the return flow coming up from the bottle into the hollow center of the nozzle. Figure 6.3 illustrates how this latter nozzle, hereafter referred to as the active nozzle, looks. A cross section is shown in the lower image of the same figure. The cut follows the center of one of the six pipes and is hence angled 7° inward towards the center of the nozzle. The active nozzle was designed to create a swirling motion of the fluid at the bottle wall and form a vortex in the center. This vortex ejects the fluid from the bottle. The fluid exiting the bottle will enter the hollow center of the nozzle and then exit the nozzle through the holes in the side wall (figure 6.3). It is directed downwards by means of a shield plate in order to sterilize the outside of the bottle. The shield plate is not shown in figure 6.3.

When the 8 mm diameter pipe was used, the measurement chamber was empty, i.e. there was no bottle located inside. The back-plate port of the chamber was used for heating while the inlet from the manifold was closed. Figure 6.4a shows a single-shot image recorded after the piston was lifted and H_2O_2/H_2O/air was injected into the chamber. The image was recorded 10 mm below the nozzle outlet plane without any binning of camera pixels. The image obtained just before the one shown in figure 6.4a showed no signal. This observation is consistent with the fact that the piston goes from its bottom to its top position in about 58 ms, which is shorter than the 100 ms between consecutive laser pulses. The photolysis pulse energy was about 60 mJ and

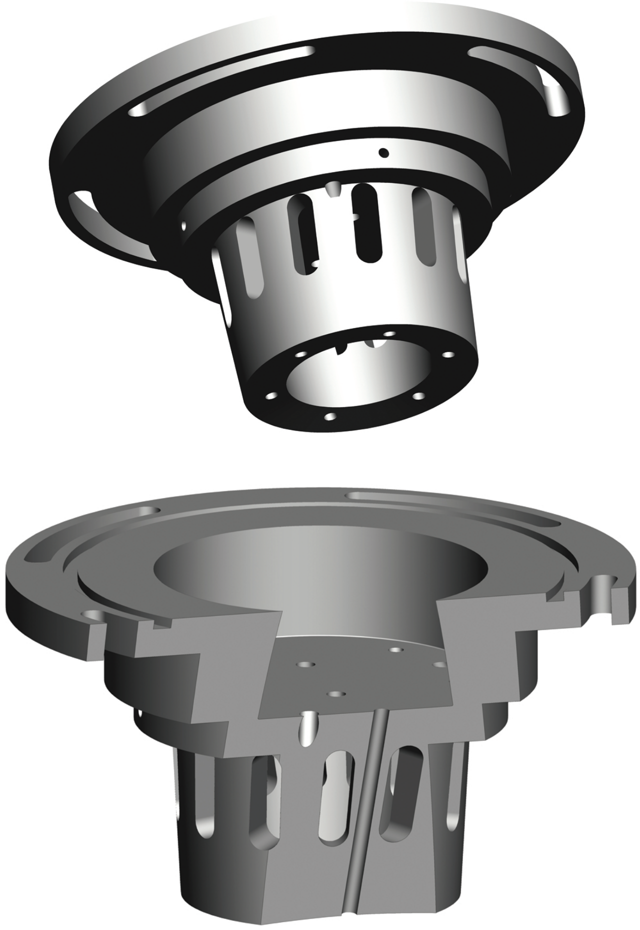

Figure 6.3: *Top: Active nozzle. Bottom: Cross section of the active nozzle. The section is angled 7° so that it follows the center of one of the six pipes.*

the corresponding number was roughly 8 mJ for the dye laser. The laser sheets were $\sim$40 mm high, and the beam waists were estimated to be rather wide, around 300-700 μm. The H_2O_2/H_2O mass flow was roughly 1.2 kg/h mixed with 8.3 m^3/h of air, and the number density of the gas mixture in the manifold was measured to approximately $2 \cdot 10^{17}$ cm^{-3} using absorption.

Figure 6.4b shows the average signal from the first 30 single shots, and panel (c) displays the standard deviation of the single-shot images forming the average in panel (b). Since only 30 images were averaged, the statistics are limited. Much of the structure observed between downstream distances $\sim$20 mm and $\sim$40 mm of panel (c) would most

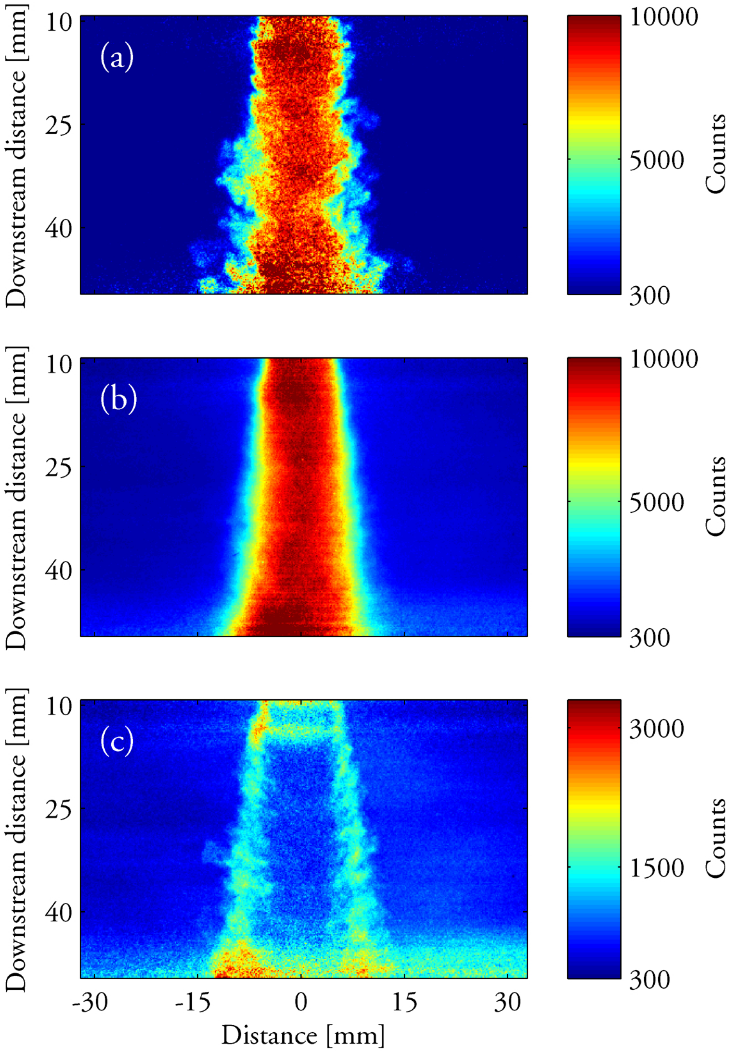

Figure 6.4: *Injection through the 8 mm diameter pipe. (a) First image recorded after lifting the piston. (b) Average of the first 30 single-shot images. (c) Standard deviation of the 30 single-shot images forming the average in panel (b).*

likely smooth out if more images had been used in the evaluation. However, the reason why more images were not included in the calculation of the average and the standard deviation is that the H_2O_2 concentration in the chamber was increasing around the jet, making it impossible to separate the jet from the surrounding volume. A small effect of the increase of the H_2O_2 concentration in the chamber can be seen as a faint signal at the bottom of panel (b) and in the lower corners of panel (c). However, the strong signals observed in the regions of the jet at the top and the bottom of panel (c) are due to the fact that these regions were in the edges of the laser sheets. Thus, the signal-to-noise ratio was lower than in the center due to low laser fluences. The definition of the standard deviation enhances noisy areas since they have significant shot-to-shot fluctuations. The lower limit of the color scale of all three panels have been chosen slightly above zero in order to restrain background noise.

Figure 6.4b gives an indication of the region where the jet is located on average, and panel (c) shows the concentration fluctuations. By measuring the slopes of the edges of the jet in panel (b), the cone angle of the jet can be estimated. For this jet it is around 9.5°. The location of the steady core of the jet is clearly seen as the hollow center in panel (c), and it can further be observed how the thickness of the fluctuating layer grows with the downstream distance. The turbulent jet accelerates the surrounding air and thereby creates vortices of different sizes. At the edge of the jet, surrounding air flows into the jet and becomes entrained, thus, enhancing mixing. The main conclusions are, however, that the PF-LIF technique can be used to perform spray studies on vaporized H_2O_2 sprays with sufficient signal-to-noise, and, hence, this study demonstrates the ability of PF-LIF to provide data in 2D. Nevertheless, while the time resolution of a single frame is high enough to momentarily freeze the flow, the repetition rate of the laser systems (10 Hz) is not sufficient to resolve turbulent fluctuations in time. Thus, it would be advantageous to use laser systems with higher repetition rates. Such systems are available, but they generally provide lower pulse energies. An estimation using equation 5.2 suggests that merely around 3.4% of the H_2O_2 molecules were photodissociated. By choosing a photolysis laser of shorter wavelength it should be possible to increase the signal substantially since the absorption cross section of H_2O_2 increases with decreasing photolysis wavelength. Hence, it is possible to compensate for signal losses due to lower pulse energies by using a shorter photolysis wavelength.

The majority of the injection studies were performed using the active nozzle. These measurements were performed in the gas rig as well as in the water rig. For each measurement conducted in the gas rig, a similar measurement was performed in the water rig at the same Re. The very same active nozzle was used in the two rigs. In the water rig, the chamber is initially filled up with tap water. When the piston lifts and opens up the channels from the mixing chamber (the equivalence to the manifold of the gas rig), water mixed with Rh590 is injected into the chamber. The pump rate or mass flow of the H_2O/Rh590 mixture is controlled by an automatic control loop, and the output from the measurement chamber is directly connected to the drain. A frequency-doubled Nd:YAG laser at 532 nm was used to induce fluorescence from the Rh590 and a 1260×1024 pixels CMOS camera was used for detection of the LIF signal. The laser was pulsed with pulse duration of roughly 5 ns and a repetition rate of 20 Hz. Sheet-forming optics were used. These components formed the laser pulses into expanding sheets, which covered the entire vertical plane of the center of the measurement chamber.

For these measurements, a quartz bottle was placed upside down in the measurement chambers of the two rigs. The bottle is open at its bottom, which was centered 5 mm below the active nozzle. The shield located around the nozzle to direct the return flow from the bottle is shown in dark gray in figure 6.5. It is just a short pipe, into which the active nozzle is inserted. The distance between the shield and the nozzle is 7 mm in the outlet plane of the six pipes. The bottle is cylinder shaped with a circular cross section, 63 mm inner diameter, and a height of 250 mm, including bottleneck and cap.

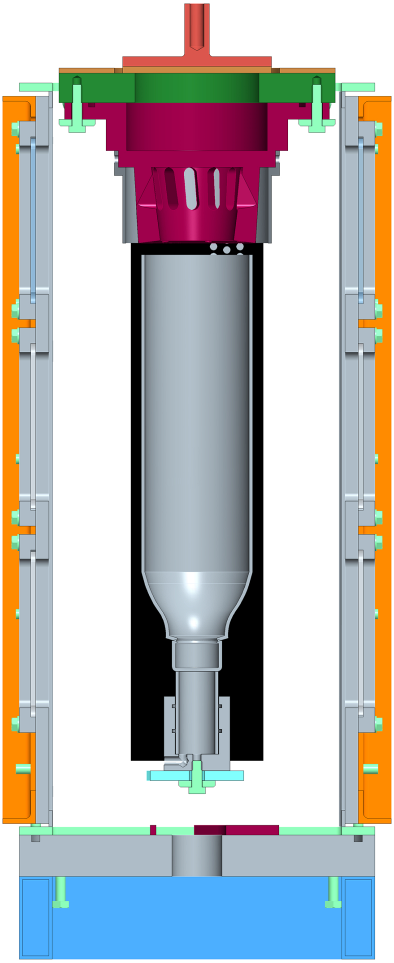

Figure 6.5: *Cross section of the gas rig measurement chamber including active nozzle with shield around and a bottle below.*

While the entire vertical plane of the center of the bottle could be captured in a single image in the water rig, it was not possible to capture such a large area in a single frame in the gas rig. One reason has been mentioned earlier; the fact that optical access is granted through the three quartz windows and not the entire side of the rig. However, even if optical access had allowed a plane covering the entire vertical cross section of the bottle to be imaged in single shot, the PF-LIF signal from H_2O_2 would probably have been too weak due to the low laser fluences that could have been obtained in such large laser sheets. Three regions located at different heights in the bottle were imaged in the gas rig. Each region was about 46 mm high, and their respective locations relative to the height of the nozzle outlet plane were 12.7-58.5 mm, 90.1-135.9 mm and 148.2-194.0 mm.

Two different mass flows were tested. These were 11.5 kg/h (1.4 kg/h H_2O_2/H_2O) and 17.0 kg/h (1.5 kg/h H_2O_2/H_2O), with measured H_2O_2 number densities around $2.4 \cdot 10^{17}$ cm^{-3} and $1.7 \cdot 10^{17}$ cm^{-3}, respectively, for the gas mixtures in the manifold. The corresponding flows used in the water rig were 527 l/h and 758 l/h respectively. The gas rig turned out to have a better operating condition at the higher mass flow. At the low mass flow, the signal did not stabilize when the entire measurement chamber had been filled with the H_2O_2/H_2O/air mixture. Instead the signal constantly kept dropping, indicating condensation problems. This phenomenon was not distinct at the higher mass flow. Regarding the water rig, both running conditions worked equally well.

Since the bottle, the nozzle and the chamber geometries of the two rigs are the same, there is no difference between the rigs regarding a characteristic length, L. The kinematic viscosities of air around 380 K and water around 292 K are 2.38×10^{-5} m^2/s and 1.04×10^{-6} m^2/s, respectively. The remaining parameter in the Re is the characteristic speed, U, and its value is determined by ν and L if Re is held constant. The gas rig measurements were performed prior to the water rig measurements, and the temperature in the manifold of the gas rig was used when the flows for the water rig were calculated. It yielded a ratio for the characteristic speeds of the flows in the two rigs, $U_{\text{gas rig}}/U_{\text{water rig}} = \nu_{gas}/\nu_{water} \approx 23$. However, there is a non-negligible uncertainty regarding the temperature of the gas rig. Prior to injection the bottle is filled with air, which has a significantly lower temperature than that of the injected H_2O_2/H_2O/air mixture. There is no thermocouple inside the bottle, but the temperature of the air surrounding the bottle was measured to be around 40 K lower than the temperature of the gas mixture in the manifold. There are three main reasons why the temperature of the gas mixture in the manifold was significantly higher than the temperature of the air inside the chamber. The volume of the manifold is roughly the same as the volume of the chamber, but a larger volume of hot gas flows through the manifold than through the chamber. The heating of the gas entering the manifold is more efficient than the heating of the air going into the chamber through the back-plate port. The reason is that the heating system for the gas entering the manifold includes both a pre-heater and the evaporator while the heating system for the air entering the chamber includes only a pre-heater. Moreover, the manifold is insulated on the outside while the chamber is not, and the possibility of insulating the chamber is limited since optical access is required. In addition to the temperature uncertainty, questions could be raised regarding the level of vaporization of the liquid H_2O_2/H_2O mixture.

Along the bottle wall, it can most likely be assumed that the time scaling between the two rigs is determined by the ratio between the inlet flow speeds, i.e. the time scale of the gas rig should be roughly 23 times faster than the time scale of the water rig. At the start of injection the scaling factor will probably be somewhat lower than 23 due to drop in temperature. However, the concentration buildup in the center of the bottle will be on a different time scale due to temperature differences between chamber and manifold. When the jets enter the bottle there will be diffusion, leading to a velocity component directed perpendicular to the bottle wall and a boundary layer will grow away from the surface of the wall towards the center of the bottle. Hence, it is conceivable that the kinematic viscosity ratio will decide the initial time scale for the center of the bottle. The kinematic viscosity of air decreases with decreasing temperature, and in the current temperature range a temperature drop of 40 K gives roughly 17% lower kinematic viscosity. It is then, due to the low temperature inside the chamber compared to inside the manifold, reasonable to believe that the concentration buildup will be roughly 17% slower in the center than close to the bottle wall if compared to the water rig measurements where there are no temperature gradients. This behavior can be seen in figure 6.6, where concentration buildup curves are shown. These curves were obtained by averaging the signal in 1.58 mm × 1.58 mm (5×5 pixels) regions in the gas rig and 1.00 mm × 1.00 mm (5×5 pixels) areas in the water rig. The resolution in the gas rig was lower than the resolution obtained in the water rig as 2×2 binning was used for the gas rig measurements, explaining the somewhat larger integrated areas for the gas rig.

Figure 6.6a shows the recorded concentration buildup in a region centered 4.8 mm from the wall, 10.6 cm down in the bottle. The time vector from the gas rig measurement has been multiplied by a factor of 18 (solid line with solid circles), which overlaps the rising edges of the concentration buildup curves obtained in the two rigs. Figure 6.6b shows the concentration buildup at the same height as the upper plot, but in the center of the bottle. The factor used to rescale the time vector from the gas rig measurement was 15 (solid line with solid circles) since it overlaps the rising edges of the data recorded in the two rigs. Hence the time scale for the initial concentration buildup in the center of the bottle is 17% slower than at the wall when compared to the flow in the water rig, i.e. in good agreement with a viscous time scaling. Also shown in both panels are the concentration buildup data from the gas rig with the time vector multiplied by 23, i.e. the factor obtained from the characteristic speeds. Note from panel (b) that this factor seems to be valid after approximately 20 s (water rig time). It could indicate that the flow is fully developed after roughly 20 s, and that the gas initially occupying the bottle has almost completely been exchanged with the hot gas of high H_2O_2 concentration from the manifold. In addition, 5 s after start of injection, the time scaling in panel (b) seems to change rather abruptly. It coincides with the time of the formation of the vortex, i.e. when the gas initially occupying the bottle is ejected and the center of the bottle is filled with hot gas of high H_2O_2 concentration.

Looking at figure 6.6, it is interesting to observe that the curves in panel (b) clearly show the decrease in concentration obtained when the vortex forms and pushes the low-

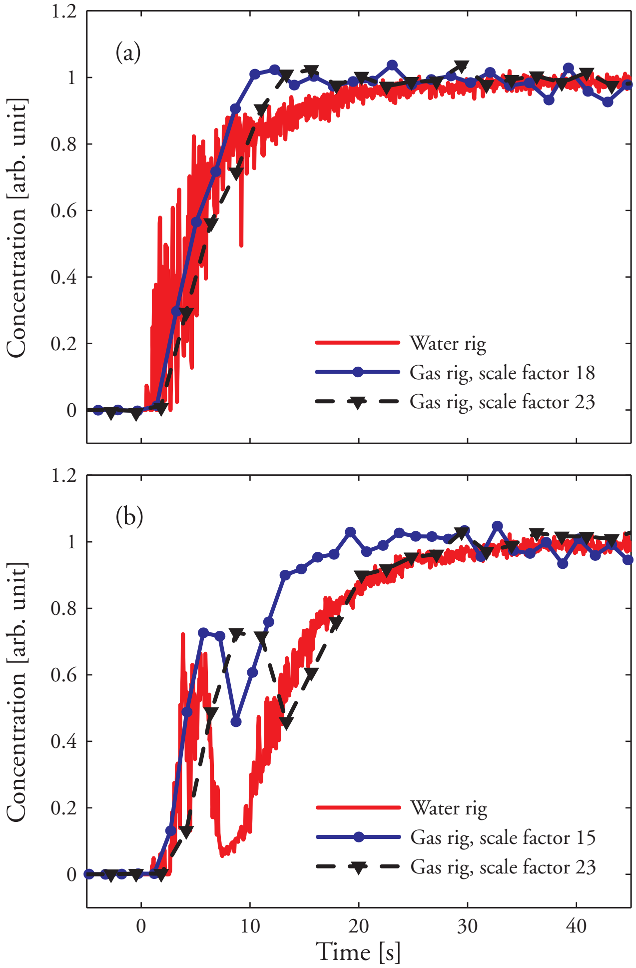

Figure 6.6: *(a) Concentration-buildup curves recorded in the two rigs 4.8 mm from the wall, 10.6 cm down in the bottle. The solid line displays the measurement in the water rig (1.00 mm × 1.00 mm size of integrated area) and the solid line with solid circles shows the data from the gas rig (1.58 mm × 1.58 mm size of integrated area) with the time vector multiplied by a factor 18. The dashed line with solid triangular markers shows the concentration buildup recorded in the gas rig with the time vector multiplied by a factor of 23. The gas rig data are the average obtained form five consecutive acquisitions. (b) Corresponding concentration-buildup curves recorded in the center 10.6 cm down in the bottle. Time scaling factors used for the data from the gas rig are 15 and 23, respectively, for the solid line with solid circles and the dashed line with solid triangular markers.*

H_2O_2 concentration gas out from the bottle. However, the concentration in the gas rig does not seem to drop as deep as the concentration in the water rig. Certainly, the time resolution obtained in the gas rig is not sufficient to fully resolve this structure. Both the upper and the lower plots in figure 6.6 demonstrate that, qualitatively, the flows are very similar in the two rigs apart from the initial time scaling. Understanding the differences in transient behavior of the flows in the two rigs is not the most important parameter for the current sterilization application. The important figure from a sterilization point of view is the dose, i.e. the H_2O_2 concentration integrated over the exposure time, and unless the exposure time is very short, any initial differences will have marginal impact on the time-integrated value. In addition, the H_2O_2 dose at the wall of the bottle is more important than the H_2O_2 dose in the center of the bottle.

From the scalar transport equation of an incompressible newtonian fluid it can be understood that the flow is governed by convection for high Re. For lower values of Re, diffusion will affect the flow to a larger extent. This phenomenon was observed outside the bottle, where the Re was lower than inside the bottle. Diffusion is much higher in the gas of the gas rig than in the liquid H_2O in the water rig. Thus, diffusion will blur structures much more in the gas rig than in the water rig. Even though somewhat limited due to the small frame, it can be seen in the upper right panel of figure 6.7 that the structures are smoother outside the bottle than what they are in the corresponding locations in the left image, recorded in the water rig. Again, it is interesting to note that the flows recorded in the two rigs show distinct similarities. The images shown in the figure were recorded before the vortex had formed. The H_2O_2 number density of the injected gas was roughly $1.7 \cdot 10^{17}$ cm^{-3}, measured in the manifold using an IR absorption sensor simultaneously as the PF-LIF images were recorded in single shot in the chamber. The time scaling factor between the measurements recorded in the two rigs is 18.

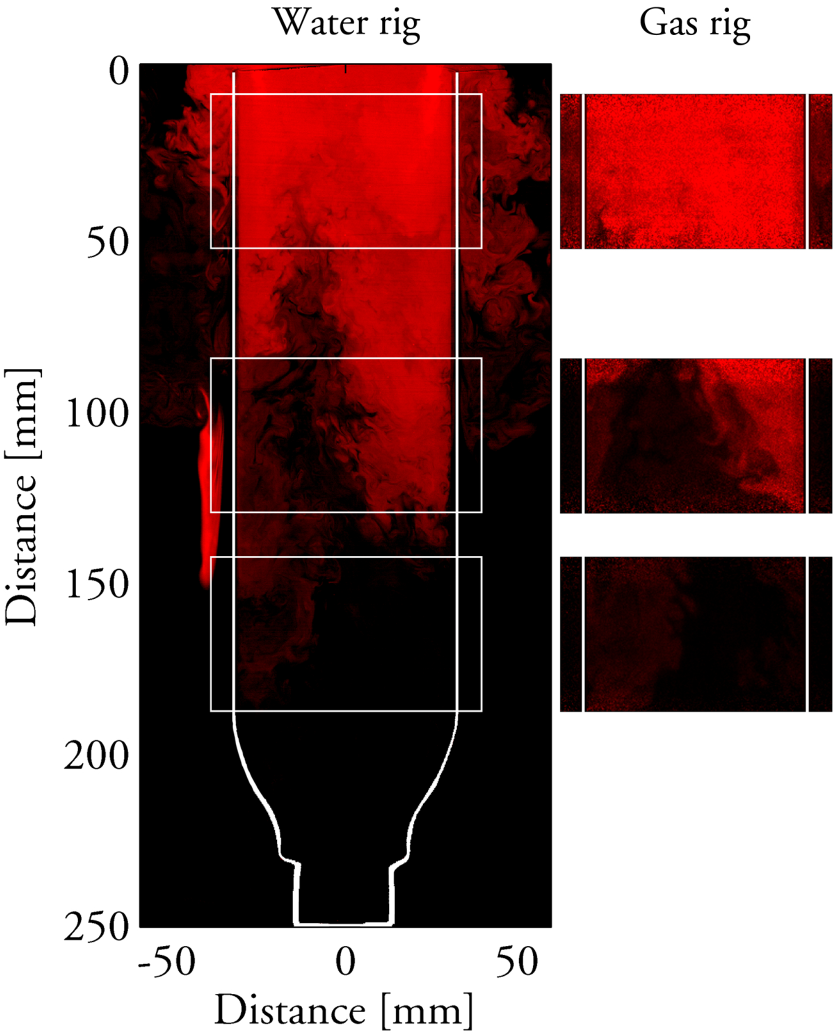

Figure 6.7: *A single-shot image obtained in the water rig is displayed to the left in the figure. The three small images to the right show corresponding images recorded in the gas rig, inserted at the heights were they were recorded. The boxes in the left image display the locations of the gas rig images. Also the contours of the bottle have been indicated. The water flow was 758 l/h and the mass flow in the gas rig was 17.0 kg/h with a* H_2O_2 *number density around* $1.7 \cdot 10^{17}$ *cm*$^{-3}$ *of the injected gas mixture. The large signal area at the center on the left side of the bottle in the left image is due to leakage of water mixed with Rh590 into the chamber prior to valve opening. The images acquired in the gas rig were recorded 0.18 s after lifting of the piston, and the image recorded in the water rig was captured after ~3.25 s, i.e. a time scale factor of 18 between the rigs.*

6.4 Sensor validation measurements

A series of measurements were performed to investigate deviations between different sensors. The sensor application of the PF-LIF technique is important since the broad industrial use of H_2O_2 makes sensor development for this species an issue of interest from process optimization points of views as well as from economical points of views. If vaporization is perfect and if the H_2O_2 molecules are known to be uniformly distributed within the vessel where the concentration is measured, PF-LIF could not compete with absorption measurements, providing the H_2O_2 concentration is high enough to give substantial absorption. The real strength of PF-LIF for sensor applications is its possibility to yield quantitative data in a point, along a line or in 2D.

For these measurements, the rig was running continuously with the chamber inlet open and both chamber exits open as well. A measurement series generally consisted of running the rig for about 30-50 minutes at a given mass ratio between the H_2O_2/H_2O solution and heated air entering the evaporator. During this time the H_2O_2 concentration would be measured using the different sensors. The mass ratio between the H_2O_2/H_2O solution and heated air would then be changed and the concentration would be measured again. This procedure was, at the most, repeated for seven different concentrations on a single measurement occasion.

A commercial absorption sensor operating in the IR spectral region was inserted in the manifold through one of its four ports. Another absorption sensor, using UV radiation around 282 nm, was attached to the lower window of the left side plate of the chamber. The laser pulses used for PF-LIF entered through the top window on the left side plate and exited through the top window on the right side plate. Detection of the PF-LIF signal was done orthogonally to the propagation direction of the laser pulses, i.e. though the upper front-plate window using the ICCD camera. The procedure of how to use PF-LIF for quantitative H_2O_2 measurements has been explained in section 5.2 and will not be repeated here. A fourth sensor, based on catalytic destruction of H_2O_2 was connected to one of the manifold ports. The idea behind the catalytic destruction sensor is to measure the temperature prior to and after catalytic destruction of H_2O_2, and from the difference calculate the H_2O_2 concentration. This sensor was connected to one of the manifold ports (part (V) in figure 6.2).

Figure 6.8 shows an example of a measurement series for which all the four sensors were used simultaneously. The boxes given for the PF-LIF technique include uncertainties from the exponential fitting due to data scattering. Due to the fact that the pump-probe delay time is sequentially stepped and some averaging is applied for each delay time in order to average out fluctuations, the number of data points recorded for each H_2O_2/H_2O/air mixture was limited to around 40 in order not to take too much time. Since a relatively low number of data points was recorded for each gas mixture, it was decided that a three-parameter exponential curve fit would be suitable for the extraction of the decay time of the OH consumption. Alternative methods such as multiplication with ramped gain profiles, mentioned in section 4.4, could be used. The three fitting parameters of the evaluation program were a_1, a_2 and a_3 in the equation $y = a_1 + a_2 \cdot exp\,(-t/a_3)$. Different measures, such as for example the mean sum of squares and the sum of the absolute vales, were used to calculate the deviation between the experimental data and fitted curves. Due to data scattering different error measures yield different curve fits and this fact was used in order to estimate the uncertainty in calculated H_2O_2 concentrations.

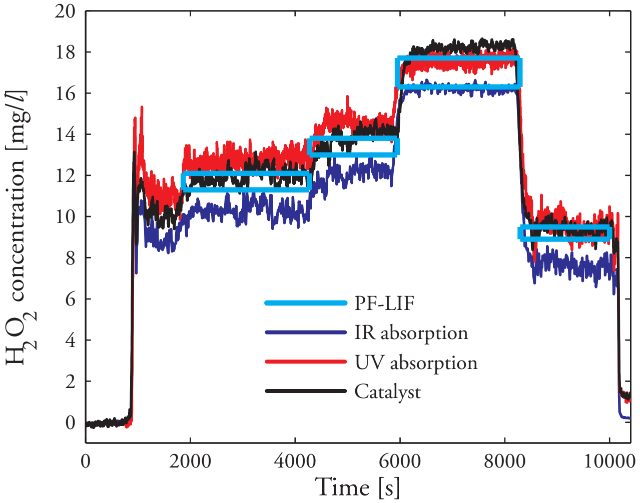

Figure 6.8: *Measured H_2O_2 concentrations using different sensors. The boxes shown for the PF-LIF results indicate errors estimated from exponential fits using different measures for the deviation between fitted curves and the experimental data.*

It can be seen by looking at the data from the two absorption sensors and the catalytic destruction sensor in figure 6.8 that the concentration fluctuations inside the rig were significant. The time resolution of the PF-LIF is far too low with the current laser systems to resolve these fluctuations. They will instead heavily influence both the accuracy and the precision of the PF-LIF technique since the exponential curve fitting is sensitive to data fluctuations. This limitation becomes more evident the faster the decay is, explaining why the uncertainty in the exponential fitting is largest for the highest H_2O_2 concentration. In order to shrink the error boxes for PF-LIF, a few measures could be taken. The concentration fluctuations of the rig must be minimized during the PF-LIF recording time. It could be achieved either by having more stable rig operation or by decreasing the measurement time for the PF-LIF. A computer program which will automate pump-probe delay time stepping and image acquisition is currently being developed and tested. It will reduce the PF-LIF acquisition time roughly by a factor of 4. A pulsed probe-laser system is, however, not optimal for a PF-LIF sensor due to pulse-to-pulse fluctuations regarding both energy and laser modes. Instead a continuous-wave laser ought to be used. With a continuous-wave laser, phase-sensitive detection could be applied as was mentioned in section 5.2.

Figure 6.8 shows that the concentration readings of the IR sensor were consistently lower than the readings of the other sensors. However, the IR sensor has proved to be sensitive to droplets due to incomplete vaporization. A low reading from this sensor could thus be an indication that vaporization is not complete. The catalytic destruction sensor is very sensitive to the gas flow rate going through it. It can to some extent be compensated for by having several thermocouples inserted into different depths of the sensor. The distance appropriate for the gas flow rate going through the sensor can then be used for the measurement of the temperature difference. Nevertheless, excluding the IR absorption sensor, the other three sensors agree to within 10%. The fact that these sensors are based on three different approaches, i.e. absorption, catalytic destruction and chemical decay, significantly strengthens the reliability of the measured concentrations. In addition, adding the results from section 5.2, it can be concluded that the current PF-LIF setup has been demonstrated to provide quantitative H_2O_2 number densities in the range $1.16 \cdot 10^{16}$ cm^{-3} to $3.0 \cdot 10^{17}$ cm^{-3} without any hardware modifications.

Chapter 7

Flame measurements

This chapter discusses PF-LIF measurements performed in different premixed, laminar flames. It is based on the results published in paper VII, but this chapter also includes some results that were not presented in the paper, and, hence, have not been published.

In order to give a brief introduction, it should be said that in 1989 Raiche et al. [141] showed that photofragmentation fluorescence could be used for detection of acetylene (C_2H_2) in flames. Since then, various techniques based on photofragmentation have been applied for combustion studies. For example, laser-induced fragmentation fluorescence has been applied for detection of alkali compounds in different combustors, see e.g. [142–144]. Osborn and Frank [145] investigated laser-induced fragmentation fluorescence from seven molecules that may give rise to C_2 Swan band fluorescence in methane flames, and our group recently showed (paper VII) that PF-LIF can be used for detection of mainly HO_2 in 2D in laminar, premixed hydrogen and methane flames.

7.1 Experimental details

The general setup for the flame measurements carried out was similar to that described in section 6.1. A schematic illustration is shown in figure 7.1. Photodissociation was performed using an Nd:YAG laser equipped with a fourth harmonic frequency-conversion unit, i.e. generating radiation at 266 nm. A variable attenuator consisting of a $\lambda/2$-plate followed by a polarizing beam splitter cube was used to control the photolysis-pulse energy. Hydroxyl radicals were probed via LIF, induced using a frequency-doubled dye laser operating with Rh590. The dye laser was tuned to the $Q_1(5)$ transition of OH near 282.75 nm (see figure 4.3). The dye laser was pumped by the second harmonic of an Nd:YAG laser, i.e. 532 nm. Both the pump and the probe-laser systems are pulsed with a repetition rate of 10 Hz, and the pulse durations are on the order of 5 ns. For some PF-LIF measurements, probing was performed using the third harmonic (355 nm) of an Nd:YAG laser. Pure LIF measurements were also performed using either the dye laser, 266 nm or 355 nm for excitation.

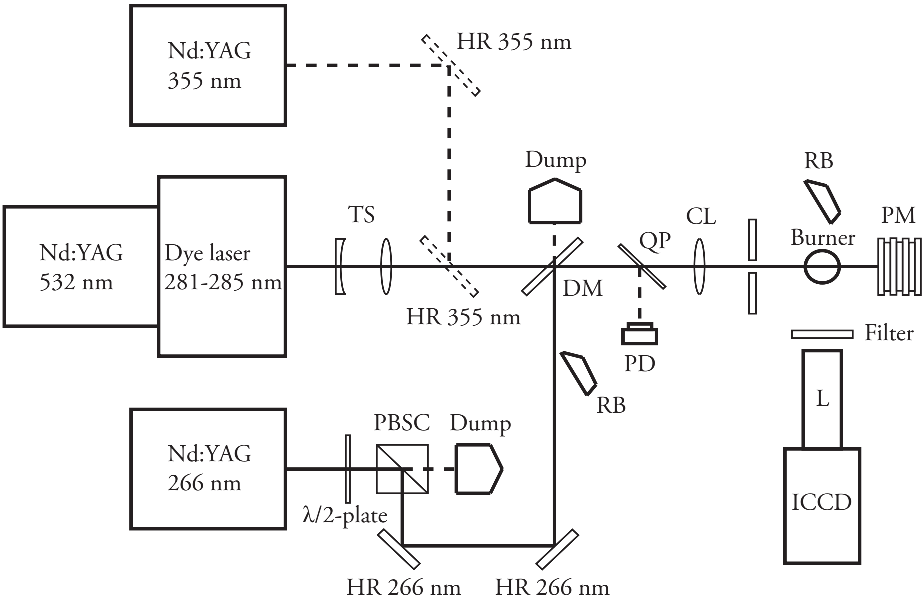

Figure 7.1: *Experimental setup used for 2D PF-LIF measurements in laminar, premixed flames. The abbreviations denote: TS; telescope, PBSC; polarizing beam-splitter cube, HR; high reflectivity, DM; dichroic mirror, QP; quartz plate, RB; razor blade, PD; photodiode, CL; cylindrical lens, L; camera lens, ICCD; intensified CCD camera, PM; power meter.*

Pump and probe beams were spatially overlapped using a dichroic mirror with high reflectivity at 266 nm and high transmission for longer wavelengths. A razor blade was mounted on a micrometer adjuster in the pump-laser lane just before the overlap dichroic mirror. The razor blade was used to partially block the photolysis beam in order to have a signal region where photofragment contributions to the observed signal would be at a minimum. After spatial overlap, laser sheets were formed using a cylindrical lens. Since the pump and the probe beams were of different wavelengths and had different divergence angles, they did not have the same distances between the cylindrical lens and their respective beam waists. The lens was positioned so that the photolysis beam had its focus in the center of the probe volume, and the probe laser was thus slightly out of focus. Measurements of the laser-sheet widths in the probe volume were most often done by orthogonally translating a razor blade mounted on a micrometer translator through the beams. In order to have both the photolysis sheet and the probe sheet foci in the center of the probe volume, counter-propagating beams could be used. Different lenses would then be used to focus the two beams. For a counter-propagating beam setup, it is, however, important to make sure that the laser beams do not propagate into the lasers. A counter-propagating beam setup may also have limited applicability in practical situations since it requires optical access from one additional side.

Detection of the induced signal was performed using an ICCD camera (1024×1024 pixels) equipped with a UV lens ($f/2$). The lens was mounted on a bellow connected to the camera. Optical resolution of the imaging system was measured with a resolution chart, and it was found to be around 50 μm. When the dye laser was used for probing, an interference filter centered at 310.5 nm with a bandpass of 11.5 nm was used to spectrally filter the signal before detection. Most often the interference filter was used in combination with a WG 305 Schott filter. For the LIF measurements with 355 nm and 266 nm, a GG 435 Schott filter was utilized. Spectrally resolved measurements were also performed with a spectrometer mounted in front of the camera. The same filters were used for these studies.

The flash lamps of the photolysis laser were used as master trigger source during the PF-LIF measurements. The trigger pulse from the flash lamps of this laser was connected to a pulse/delay generator with four outputs. One output was used to trigger the Q-switch of the photolysis laser, two output channels were used for triggering of the probe laser system, and the fourth output channel was used to trigger the camera. A UV-sensitive photodiode connected to a 3 GHz digital oscilloscope faced a quartz plate inserted in the path of the overlapped beams (figure 7.1). This setup allowed accurate monitoring and adjustments of the pump-probe delay time. The signal from the photodiode was logged during excitation scans in order to allow probe-laser pulse energy correction.

Even though PF-LIF can be used to obtain images of the distribution of HO_2 and H_2O_2, the technique has not been applied to imaging of these two species in flames prior to our recent demonstration (paper VII). One reason is most certainly the non-species specific nature of PF-LIF and the fact that OH occurs naturally in flames. The signal contribution from natural OH has to be subtracted from the image recorded with photolysis. Hence, when probing with the dye laser tuned to an OH transition, two consecutive images were recorded, one with both the photolysis and the probe laser fired, and one using the probe laser only. The latter image was then subtracted from the former, providing an image that reflected only the signal from OH photofragments. As has been mentioned in section 5.1, the probe laser also photodissociates HO_2 and H_2O_2. Thus, if the photolysis of HO_2 and H_2O_2 due to the photolysis pulse is significant, more than just signal from naturally occurring OH will be subtracted when the image recorded with only the probe laser fired is subtracted from the image recorded with both the pump and the probe lasers fired.

We have investigated several different premixed, laminar H_2/O_2, CH_4/O_2 and CH_4/air flames on two different burners. The H_2/O_2 and CH_4/O_2 flames were stabilized on a 2 mm gas-welding nozzle, while the CH_4/air flames were stabilized on a piloted coaxial burner, which has been described in [146]. Briefly, this burner consists of two coaxial tubes with 2.2 mm and 22 mm diameter, respectively. A ceramic flame holder with 1 mm side length squared holes is located between the inner and the outer tubes. The two tubes can have independent gas supplies. It allows an inner and an outer flame to be formed. The outer flame then works as a buffer, effectively eliminating the influence of ambient air on the inner flame. See figure 7.2 for an illustration of the coaxial burner. Our measurements in this burner were all performed at or around stoichiometric mixture, with gas speeds in the inner and outer tubes around 12 m/s and 0.4 m/s, respectively. All gas flows were controlled using calibrated mass-flow controllers.

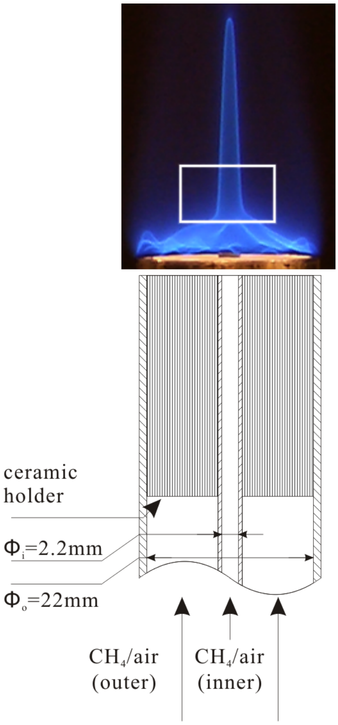

Figure 7.2: *Schematic illustration of the coaxial burner (Courtesy of B. Li).*

The H_2/O_2 and CH_4/O_2 flames studied were rich, with $\phi \approx 8$ for the H_2/O_2 flames and $\phi \approx 2.2$ for the CH_4/O_2 flames. Due to these rich fuel/oxidizer ratios, the flame temperatures and speeds were significantly lower than the maximum temperatures and speeds achievable for H_2 and CH_4 mixed width O_2. There are two obvious drawbacks with the welding nozzle. First, the flame structures have significant curvatures and, second, there is nothing protecting the flame from influence from ambient air. Hence, using the welding nozzle seriously limits the possibilities of comparing experimental results with one-dimensional (1D) chemical kinetic calculations.

7.2 Flame zones and Boltzmann population dynamics

A premixed flame can be divided into four zones; the unburned gas zone, the preheat zone, the reaction zone and the product gas zone. The unburned gas zone has the temperature of the fuel and oxidizer gases supplied. In the preheat zone, the gas is heated by atoms and molecules diffusing from the reaction zone. Here reactions start to occur and the reaction rates increase as the temperature increases closer to the reaction zone. The exothermic reactions mainly occur in the reaction zone, which is also called the flame front. This is roughly the region around the maximum temperature gradient. The reaction zone passes on to the product gas zone, where the temperature levels off since the combustion products have been formed. The product gas zone is also referred to as the burned gas zone or the post-flame zone.

Figure 7.3 shows a chemical kinetic calculation for a laminar, premixed, 1D CH_4/air flame at stoichiometric equivalence ratio. As can be seen in the figure, calculations predict HO_2 and H_2O_2 to be present in the preheat and reaction zones. These two species are thus present in a region which covers a large temperature span. If they are going to be probed with PF-LIF, it is important to excite OH from a rotational level that is populated over a temperature range going from roughly 300 K to about 2000 K. In addition, it is important to have high spatial resolution of the imaging system due to the fact that the width of the HO_2 and the H_2O_2 peaks are on the order of 500 μm for premixed laminar H_2/O_2 and CH_4/air flames.

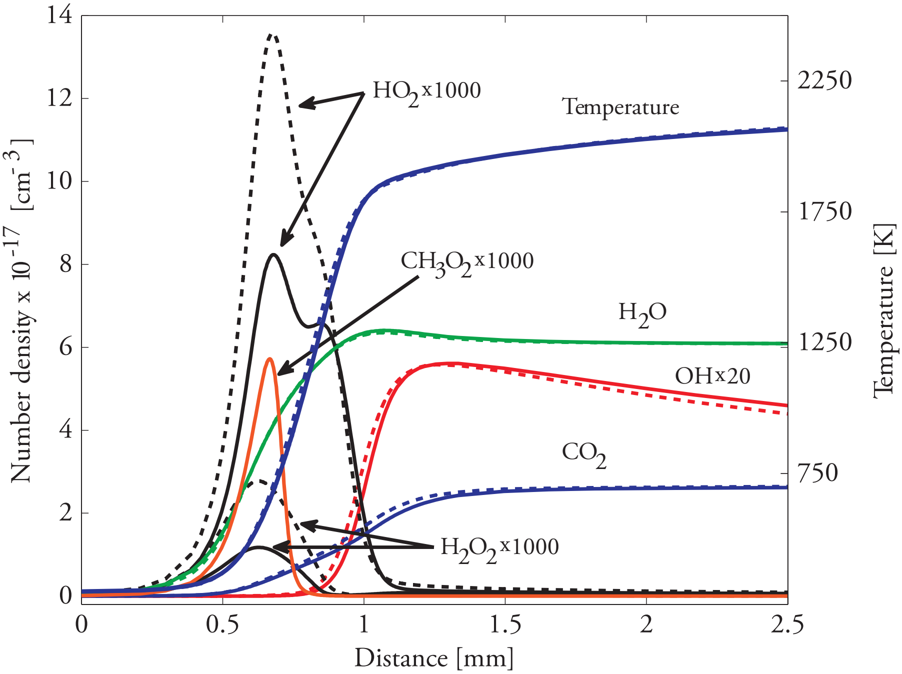

__Figure 7.3:__ Species and temperature profiles obtained from 1D chemical kinetic calculations using the Konnov C/H/N/O mechanism (solid lines) as well as the GRI 3.0 mechanism (dashed lines) for a stoichiometric CH_4/air flame. The methyl peroxy radical (CH_3O_2) is not included in GRI 3.0 (Calculations by A.A. Konnov).

The $Q_1(5)$ transition, indicated in figure 4.3, was used due to the population dynamics of the $J = 5.5$ level in the F_1 branch. As was shown in figure 4.4, the population on this level peaks for a temperature around 750 K, which almost coincides with the temperature at the peak of the HO_2 profile shown in figure 7.3. In addition, it is clear from figure 4.4 that this rotational level is populated over a wide temperature range. However, since the fractional population is not constant over the temperature span 300-2000 K, it is important to compensate for differences in fractional population before comparing calculations and measurements. Due to composition variations and temperature gradients, it is also important to compensate for differences in fluorescence quenching over the imaged area before any comparison between measurement and calculation is done.

7.3 Fuel rich H_2/O_2 flames

Studies of the H_2/O_2 flames are reference cases, which provide useful information for measurements in the methane flames. Both hydrogen and methane flames have high concentrations of H_2O in their product zones, but only the methane flames contain species with carbon. Several studies have been performed on photodissociation of H_2O, and the main photolysis channel generates OH(X) + H, see the review article by Sato [147] or, for two-photon photodissociation at 266 nm, the paper by Underwood and Wittig [148]. Since the photolysis products of HO_2 and H_2O_2 are also OH(X), it is important to verify that H_2O photolysis does not interfere. A hydrogen flame is arguably the best flame for an investigation of the influence of photofragmentation of H_2O under flame conditions, since the number of flame species is at a minimum. Figure 7.4a shows a typical averaged image after subtraction of the signal from naturally occurring OH. The PF-LIF image is an accumulation of 5000 single shots obtained in 50 readouts, i.e. 50 frames of 100 hardware accumulations. The pump-probe delay time was 10 ns. Panel (b) shows the profile of 30 vertically summed pixel rows at the height indicated by the arrow in panel (a). As evident from the figure, there is no signal apart from the Bunsen-shaped profile. This observation holds true also when the pump-probe delay time is increased. Any OH photofragments from photolysis of H_2O are thus negligible.

In order to check whether photodissociation of hot CO_2 could induce interfering OH signal, CO_2 was seeded into the H_2/O_2 mixture, which supplied the burner. It is an important piece of information since the methane flames contain large number densities of hot CO_2 in their reaction and product zones. Carbon dioxide cannot produce OH as a direct photofragment, but O atoms created from CO_2 photodissociation could react with other flame species and produce OH. Due to the high temperatures of flames, these reactions could be fast enough to produce detectable signal levels on the ns time scale.

It should be stressed that CO_2 was seeded into the flame along with fuel and oxidizer. Hence, CO_2 was present in the entire flame, which is not the case for the methane flames, where it is basically limited to the reaction and the product zones (see figure

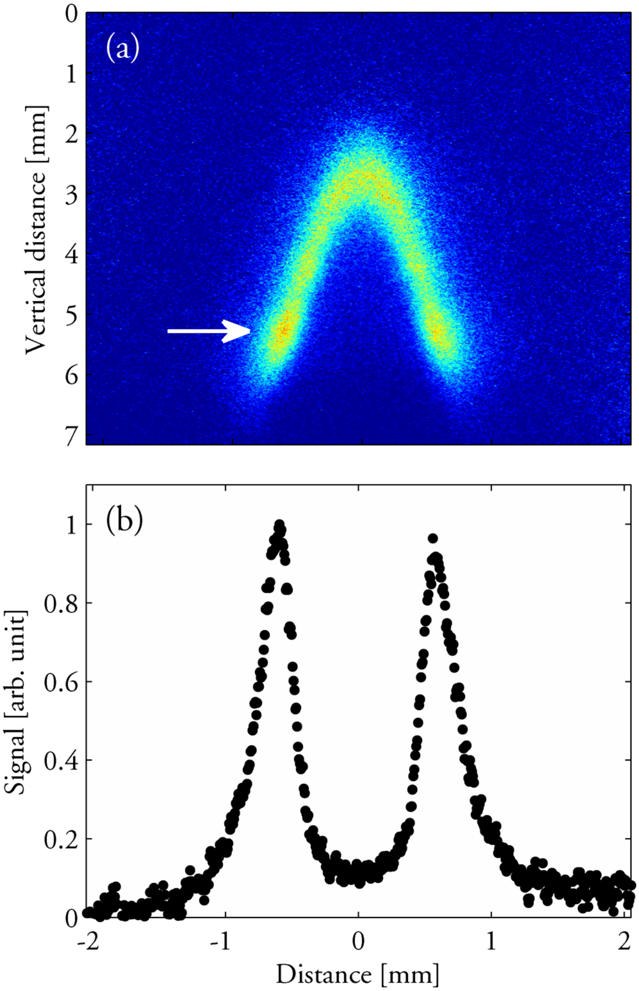

Figure 7.4: (a) Photofragmentation laser-induced fluorescence signal remaining after subtraction of signal from natural OH for an H_2/O_2 flame around equivalence ratio 8. The number of accumulations was 5000 and the pump-probe delay time was 10 ns. (b) Signal averaged over 30 pixel rows centered at the height indicated by the arrow in panel (a).

7.3). Another important difference between the H_2/O_2 flames and the methane flames is that the former flames were roughly 1000 K cooler than the latter ones due to the very rich equivalence ratio (~8) of the H_2/O_2 flames. The absorption cross section of CO_2 increases strongly with increasing temperature [149].

The result from an experiment where CO_2 was seeded into an H_2/O_2 flame is displayed in figure 7.5. The Bunsen-shaped signal region seen in figure 7.4a is situated just below the signal seen in figure 7.5. There is a broad signal region above the Bunsen shaped signal area. This contribution is not observed in figure 7.4a, and, thus, it has to be connected to the addition of CO_2 into the flame. Between 0 mm and $\sim$1.3 mm down the vertical distance in figure 7.5 there is no signal although the probe sheet extended into this region. However, the upper part of the photolysis sheet was blocked with a razor blade, explaining the sharp signal edge. Since there is no signal in the upper part of the figure, the subtraction of signal contribution from naturally occurring OH is correct, i.e. it does not generate any artifacts.

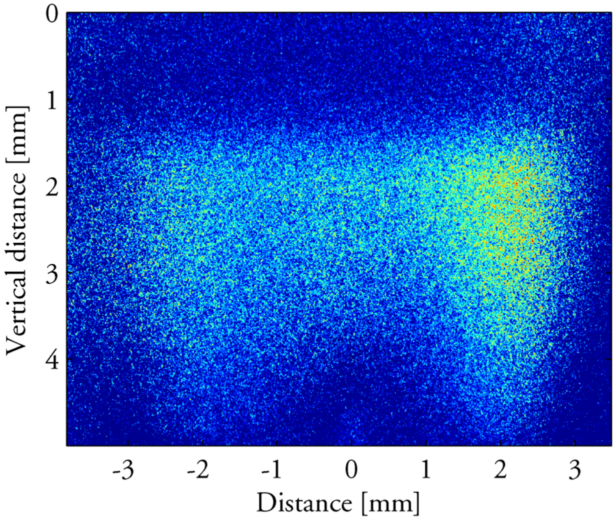

Figure 7.5: *Photofragmentation laser-induced fluorescence signal remaining after subtraction of the signal from naturally occurring OH in an H_2/O_2 flame when seeding it with CO_2.*

7.4 Fuel rich CH_4/O_2 flames

A large variety of different studies have been carried out in fuel-rich methane/oxygen flames stabilized on the 2 mm diameter gas-welding nozzle. Apart from performing PF-LIF measurements using 266 nm for photodissociation and either 282 nm or 355 nm for photofragment detection, LIF measurements have been performed with excitation at 266 nm as well as at 355 nm and around 282 nm. In addition, lifetime-imaging experiments have been conducted using 355 nm excitation, see paper II. The CH_4/O_2 flames are interesting and challenging for UV experiments, and at the time of writing, vast amounts of data remain to be analyzed.

Formaldehyde-LIF images recoded in these flames using the third harmonic of an Nd:YAG laser show dual-peak structures, see the solid line in figure 7.6. The data shown in the figure was obtained at an equivalence ratio around 2.2 and with a GG435 (Schott) filter in front of the camera lens. Fluorescence lifetime imaging measurements were performed at equivalence ratio 2.6, and the formaldehyde-LIF signal displayed a double peak also at this stoichiometry. However, when the images were corrected for differences in fluorescence quantum yield, the dual-peak structure transitioned to a single peak. This result clearly demonstrates the importance of correcting for fluorescence quantum yields even for relative measurements. However, when a 266 nm laser pulse was fired before the 355 nm probe pulse, signal peaks (dashed lines in figure 7.6) which coincide with the outer peaks of the solid line in figure 7.6 were obtained after subtraction of the signal recorded firing the 355 nm probe laser only. The new signal contribution is seen to be stronger than the initial peaks. It should be pointed out that the pump-probe delay time was long enough for any fluorescence induced by the photolysis pulse to decay before the camera gate opened. The natural interpretation is that the 266 nm laser pulse photodissociates some species and formaldehyde (CH_2O) is formed. Spectral emission investigations confirm that the observed signal both with and without the photolysis laser fired is from CH_2O. It should be emphasized that the outer signal peaks in figure 7.6 also seem to spatially coincide with signal peaks induced directly by the 266 nm laser pulse. This signal contribution is only observed if the camera gate is set to overlap the photolysis pulse. It has been shown, through

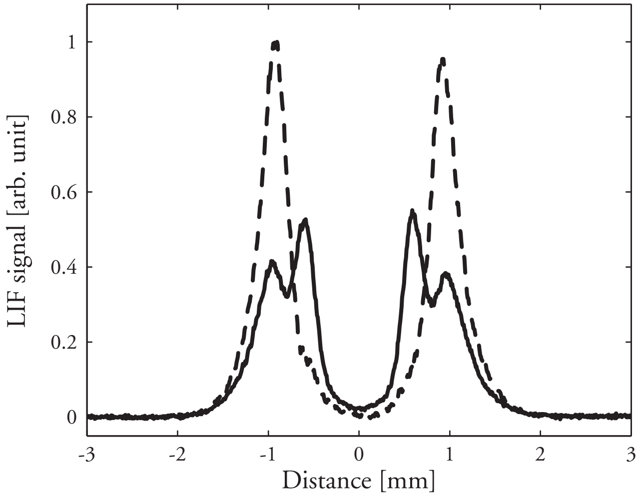

Figure 7.6: *Laser-induced fluorescence signal obtained in a CH_4/O_2 flame at equivalence ratio 2.2 using 355 nm for excitation (solid line). The dashed line is the signal that remained when PF-LIF experiments were performed using 266 nm for photodissociation and 355 nm for probing after subtraction of the signal shown by the solid line.*

spectral investigation, that the prompt signal stems from excited C_2 (Swan bands). A power-dependence study of the signal showed a non-linear dependence on the 266 nm laser fluence. When the signal is displayed in log-log scale, three different laser fluence regions may be identified. First the signal increases with a slope close to unity. It quickly switches and becomes dominated by a higher-order process, the slope being around 1.75. As the laser fluence is increased even further, the signal goes into a new regime where the slope is around 0.6. The third region is most likely partially saturated.

Using the dye laser tuned to probe the $Q_1(5)$ transition of OH following photodissociation at 266 nm, provides different signal contributions depending on the pump-probe delay time. In order to suppress interfering emission which is not from OH $A^2\Sigma^+\,(v'=0) \rightarrow X^2\Pi\,(v''=0)$ transitions, an interference filter centered around 310.5 nm with 11.5 nm bandpass was used for these measurements. Nevertheless, if only the photolysis pulse was fired, signal was still detected by the camera when its gate overlapped the photolysis pulse. The signal showed a smooth function following the filter transmission when spectrally resolved detection was applied. It is thus clear that this signal contribution was not from OH. It is probable that the emission stems from polyaromatic hydrocarbons (PAH), which are expected to be present in such a fuel rich flame. It should be stressed that this presumed PAH signal only is present for short pump-probe delay times, and it is easily removed by recording an image with only the photolysis laser fired and then subtracting this image from images recorded using both the photolysis laser and the probe laser. Naturally, images recorded using the photolysis laser only have to be recorded with the camera gate at the same temporal position as when the PF-LIF images are recorded. To sum up, it can be concluded that the outer peaks displayed by the solid line in figure 7.6 may be due to CH_2O photofragments which were generated and excited by the 355 nm laser pulse. This suggestion is supported by the fact that the outer peaks were stronger than the inner peaks when a picosecond (ps) laser was used for excitation and the equivalence ratio was 2.6 than when a ns laser was used for excitation and the equivalence ratio was 2.2.

A typical example of an accumulated PF-LIF image recorded in the CH_4/O_2 flame at $\phi = 2.2$ is shown in figure 7.7 after subtraction of the signal from naturally occurring OH. The image was recorded for a pump-probe delay time of 200 ns. A relatively strong Bunsen-shaped signal is seen as well as a non-zero signal level in the product zone. However, there is also a weaker structure on the reactant side of the stronger Bunsen-shaped signal region. These two Bunsen-shaped regions have, through wavelength-dispersed detection as well as excitation-wavelength scanning, been verified to originate from OH. The outer, stronger of these two structures, is predicted by chemical kinetic modeling if HO_2 and H_2O_2 are considered. However, in order for calculations to predict the inner structure, photodissociation of the methyl peroxy radical (CH_3O_2) has to be taken into account. Kassner and coworkers [150] performed photolysis experiments on CH_3O_2 in the wavelength range 210-290 nm. They detected prompt OH emission around 309 nm, meaning that $\mathrm{OH}(A^2\Sigma^+)$ was formed directly from photolysis (treshold $\lambda \leq 397$ nm). They also observed a sharp signal peak around 282 nm, which they ascribed to excitation of OH(X), formed by photolysis. Hartmann et al. [151] studied photofragmentation of CH_3O_2 at 248 nm, and they detected both OH(A) and OH(X). They also

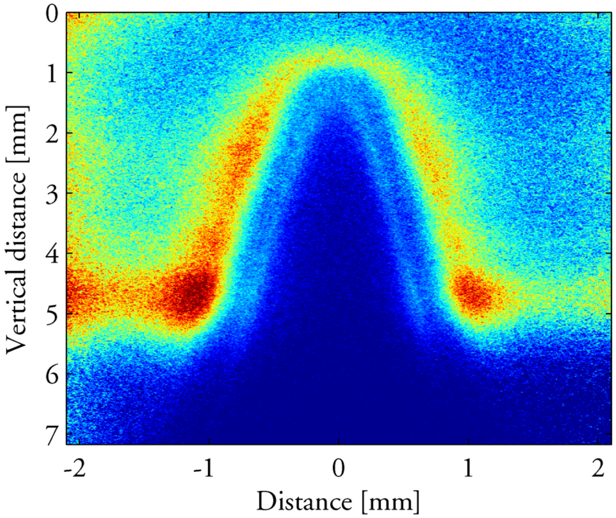

Figure 7.7: *Measured distribution of OH photofragments from 5000 accumulated single shots obtained in 50 readouts in a* CH_4/O_2 *flame at equivalence ratio* $\phi = 2.2$. *The pump-probe delay time was 200 ns. The reason why the lower part of the signal regions is stronger than other parts in the figure is due to the fact that the probe-laser beam was not spatially cleaned, and it was more intense in the lower region than in the upper region.*

determined the photodissociation quantum yield for OH generation at 248 nm to 0.06. We have, however, not been able to verify any OH contribution to the prompt fluorescence emission observed following the 266 nm photolysis pulse. It should be stressed though, that the prompt emission ascribed to PAH fluorescence for short pump-probe delay times is significantly stronger than any OH-photofragment signal. Thus there may be promptly emitted OH signal masked by the PAH fluorescence.

7.5 Methane/air flames around stoichiometric mixture

The CH_4/air flame measurements performed using the coaxial burner are those which can most easily be compared to chemical kinetic calculations. The flames on the coaxial burner are not 1D, but the hot, burned shielding gas that surrounds the inner flame makes the latter very stable and it also eliminates the influence from ambient air. Quantitative comparison between experiments and chemical kinetic calculations have been carried out.

A typical accumulated image recorded with equivalence ratio 1.15 in the inner flame cone and 1.02 in the outer flame cone is displayed in figure 7.8a. The pump-probe delay time was 80 ns. The image recorded with the photolysis laser blocked is not shown since

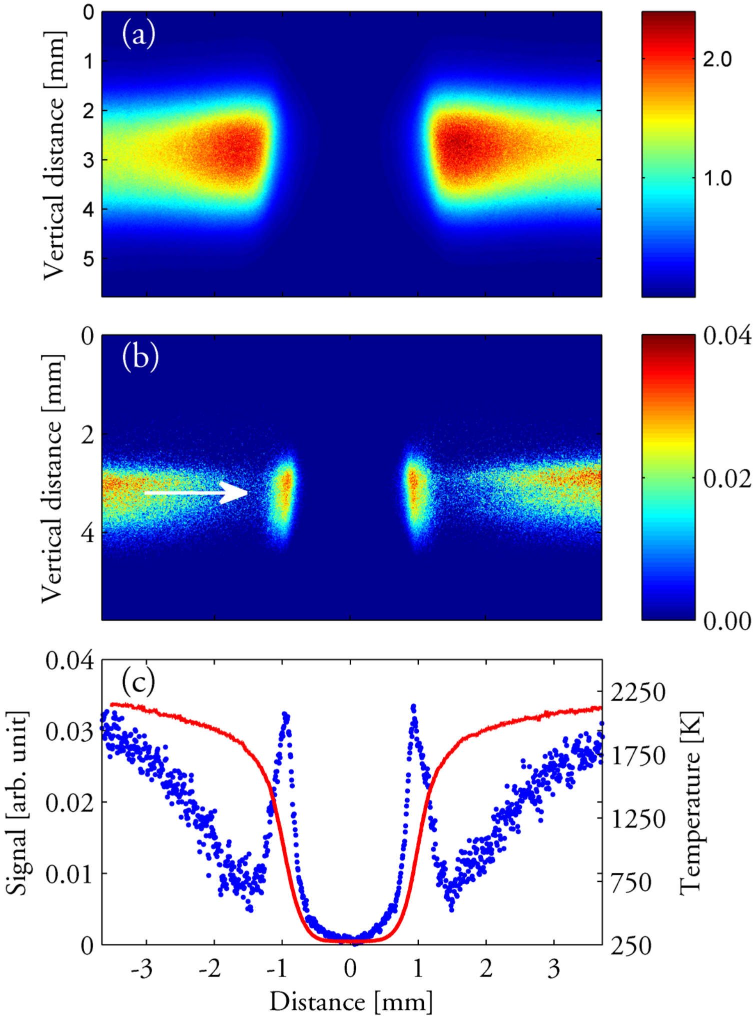

Figure 7.8: *(a) Typical PF-LIF signal obtained in the CH_4/air flame before subtraction of signal from natural OH (equivalence ratio 1.15). (b) Signal remaining after subtraction of natural OH contribution. (c) Cross-section plot (blue dots) taken by averaging 20 pixel rows at the arrow in panel (b) along with measured temperature profile (red solid line).*

it looks virtually the same as figure 7.8a. Panel (b) of the same figure shows the signal remaining after removal of signal from naturally occurring OH. A razor blade blocked the upper part of the photolysis beam, which is why the signal in panel (b) does not extend as high up as the signal in panel (a). Note that the intensity is roughly 60-70 times lower in panel (b) compared to panel (a). Panel (c) shows a cross-section plot of the average signal in panel (b) around the position indicated by the arrow. Also shown in panel (c) is the temperature profile, measured using Rayleigh scattering at 266 nm. Rayleigh cross sections were taken from [152], and the procedure of assigning these cross sections is described in paper VII.

In order to estimate the cross section area (A_{eff}) of the photolysis laser sheet, a power-dependence measurement of the PF-LIF signal from a free flow of a mixture of H_2O_2/H_2O and N_2 was performed. A function of the type:

$$C\left(1 - e^{-(\lambda\sigma E)/(hcA_{eff})}\right) \tag{7.1}$$

was then fitted to the experimental data points with fitting parameters C and A_{eff}. In equation 7.1, λ denotes the photolysis wavelength, i.e. 266 nm, σ is the absorption cross section of H_2O_2 at 298 K ($4.02 \cdot 10^{-20}$ cm^2 [76]), E is the pulse energy of the photolysis laser, h is the Planck constant and c is the speed of light. Note the similarity between equation 7.1 and equation 5.2. The exponent is simply the number of photons per unit area multiplied with the absorption cross section at that wavelength and temperature. Note that these equations assume top-hat laser spatial profiles. Equation 7.1 will only provide one value for A_{eff} from a power-dependence plot; thus, it will not handle the broadening of the effective area of the laser profile due to saturation effects for high energy densities. It is important to stress that the effective area obtained from the measurement is an approximation. Nevertheless, the obtained value, $A_{eff} = 0.00243$ cm^2 was used to calculate the signal from HO_2, H_2O_2 and CH_3O_2. The concentration profiles of these species along with the temperature profile were calculated using the Konnov detailed C/H/N/O mechanism [28] for a 1D, premixed, laminar CH_4/air flame at equivalence ratio 1.15. In order to use equation 5.2 to calculate number densities of OH photofragments, temperature-dependent absorption cross sections are required. For HO_2 and CH_3O_2, the model given by Joens [153] was used. Note that a λ is missing in the denominator of equation (1) of [153]. Regarding H_2O_2, temperature-dependent absorption cross sections were obtained from interpolation and extrapolation of the data provided in [82] and [154]. The photolysis-pulse energy was measured at 30 mJ, giving a fluence of 12.3 J/cm^2, which is outside the linear regime. At this fluence clear saturation effects are seen in a photolysis fluence power-dependence plot. One such plot is shown in paper VII.

Before comparing calculated and experimental profiles, both of these have to be adjusted for Boltzmann population dynamics as well as differences in fluorescence quantum yield due to different quenching environments across the flame. Since only the chemical kinetic calculations had information about concentrations of quenching species, it was natural to perform the compensation on the calculated results rather than the experimental data in order to avoid mixing between experimental and calculated data in the evaluation process. In figure 12 of paper VII, experimental profiles of OH photofragments and natural OH are shown along with calculated profiles, which have been corrected for Boltzmann fractions and quenching. The experimental data forming the basis for the plots in figure 12 in paper VII were recorded at a probe fluence of

21 mJ/cm^2. Even though it is a relatively high fluence for many applications, it is still below the saturation fluence corresponding to I_{SAT} (a definition of I_{SAT} can be found in [155]). Here, a data set recorded with a probe fluence of 750 mJ/cm^2 will be presented instead. This probe fluence is well above the saturation fluence, roughly about a factor of 15. It can thus be assumed, as a first-order approximation, that stimulated emission should be the dominant loss mechanism rather than collisional quenching, knowing that the laser pulse has a temporal width of ~5-10 ns, which is longer than the ~2 ns [156] excited-state lifetime of OH under the current conditions. Hence, no quenching corrections have been performed on the calculated data shown in figure 7.9.

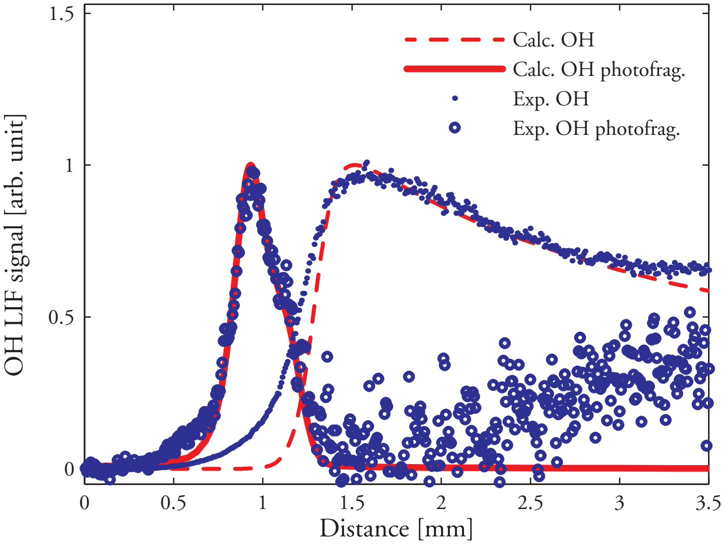

Figure 7.9: *Experimental signals from OH photofragments and natural OH together with the corresponding calculated signals for the CH_4/air flame at equivalence ratio 1.15. The experimental OH-photofragment profile was recorded with a pump-probe delay time of 10 ns.*

The x scale of the calculation has been translated in figure 7.9 so that the calculated and experimental OH photofragment peaks coincide. The agreement between the calculated photofragment peak and the experimentally measured PF-LIF peak after subtraction of signal from natural OH is excellent. However, the agreement between the OH profiles is not as good as for the data recorded with 21 mJ/cm^2 probe fluence (figure 12 in paper VII). The main reason why the measured natural OH profile is higher between $x = 0.5$ mm and $x \approx 1.4$ mm than what calculations predict is most likely that the effective width of the probe beam was increased due to saturation. Since the flame was not 1D, but rather had a circular cross section if cut in a horizontal plane, the curvature of the flame together with the width of the probe laser sheet make the OH profile grow towards the center of the flame, which is what can be seen in the figure.

See figure 7.10 for an illustration of this phenomenon. The OH-photofragment peak is not as severely affected since the spatial width of the photofragmentation laser beam at 266 nm is significantly smaller than that of the probe laser. In addition, excitation of photofragments generated by the probe pulse will yield a signal contribution to the OH profile at the position of the HO_2 and H_2O_2 profiles.

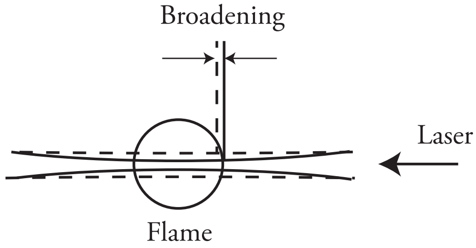

Figure 7.10: *Illustration of how the measured OH profile broadens towards the center of the flame due to the flame curvature if the laser sheet is wide.*

A temporal response study of the signal in the reaction zone found that the signal peaked for a pump-probe delay time of roughly 200 ns, and a small signal contribution was still measurable 100 μs after photolysis. Thus, high repetition-rate laser systems might thus not be suited for these type of studies since it is important that the flame reaches equilibrium between consecutive photolysis pulses. Figure 7.11a shows the reaction zone signal as a function of the pump-probe delay time for delay times up to 10 μs. The corresponding plot of the signal in the product zone, $\sim$3 mm from the flame center, is provided in figure 7.11b. According to figure 7.8c, the temperature is roughly 2050 K 3 mm from the flame center. The CO_2 absorption cross section at 266 nm is $6.01 \cdot 10^{-21}$ cm^2 [149]. Assuming $CO_2 + h\nu \rightarrow CO + O$ to be the only photolysis channel of CO_2, the upper level (photolysis quantum yield of 1.0) for the amount of photodissociated CO_2 molecules in the current experiment would be 9.5% according to equation 5.2. Three different photolysis quantum yields were investigated by perturbing the Konnov mechanism and study the buildup of OH. The three photolysis levels investigated were 0.01, 0.05 and 0.1, the last one roughly corresponding to a photolysis quantum yield of 1.0 since about 10% (9.5%) of the CO_2 molecules absorbed a photon. The three calculated OH-buildup curves are included in figure 7.11b. Rate-of-production analysis showed that the buildup of OH before 1000 ns is due to the reactions $O + H_2O \rightarrow 2OH$ and $O + H_2 \rightarrow OH + H$. Consumption of OH after 1000 ns proceeds mainly through the reactions $OH + O \rightarrow H + O_2$ and $H + OH + M \rightarrow H_2O + M$.

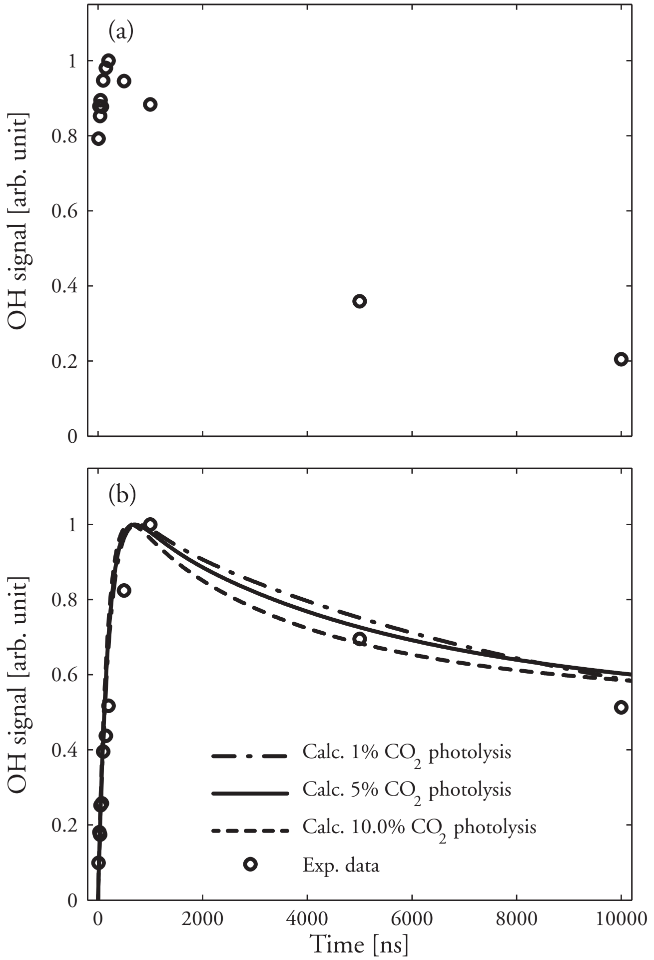

Figure 7.11: *(a) Reaction-zone photofragment signal as a function of the pump-probe delay time. (b) The interference signal in the product zone as a function of the pump-probe delay time. Also shown in panel (b) are three calculated curves corresponding to different photolysis levels of* CO_2 *into* $CO + O$*.*

Chapter 8

Outlook

This chapter briefly proposes ideas and possible measurements which have not yet been tested and verified experimentally. Some of the investigations mentioned here are planned in the near future, while others require additional studies before they can be carried out. The suggestions and ideas presented in this chapter are not supported by detailed literature analysis, and should thus be subject to some literature studies before being carried out experimentally.

Since H_2O_2 and H_2O often appear in the same systems, an interesting diagnostic could be to probe H_2O via two-photon LIF at 248 nm, while having a second laser, tuned to an OH transition to probe OH photofragments generated by the 248 nm photolysis of H_2O_2. If this method is going to be useful in practical situations, it is important that the OH contribution from photodissociation of H_2O is low compared to the number of OH photofragments generated from H_2O_2. Multiphoton studies of H_2O using excitation wavelengths near 248 nm have been performed by several research groups, see e.g. [157–160]. Common for these studies is that very high laser-pulse energies were used, on the order of 100 mJ/pulse focused to either a point or a sheet. Hence, the photodissociation of H_2O_2 is expected to be saturated, and the photofragment contribution from H_2O_2 could be much larger than that from H_2O. However, for experiments in free flows of H_2O_2/H_2O generated from liquid mixtures, the significantly higher equilibrium vapor pressure of H_2O compared to that of H_2O_2 could be problematic. On the other hand, in industrial applications, vaporization is often performed actively in an evaporator, thus providing a gas mixture with the same H_2O_2/H_2O ratio as in the feeding liquid. Neij and Aldén [158] recorded excitation scans around 248 nm in ambient air as well as in a hydrogen flame. Their results show that the two-photon LIF signal from H_2O (emission peak around 425 nm) is due to resonant excitation. Thus, two images could be recorded, one with the laser tuned to a two-photon H_2O absorption peak and one image with the laser tuned away from this resonance. The photofragment contribution from H_2O_2 ought to be equal in the two images for a small wavelength tuning, while the difference in the contribution from H_2O should be significant.

All the PF-LIF measurements reported on in this thesis were performed using ns laser pulses under atmospheric pressure. Switching to ps pulses will open new fields since it will allow the nascent rotational population to be probed. Sinha et al. [161] measured the rotational state distribution following photodissociation of HO_2 at 220 nm. They found that the nascent rotational population is highest in $N = 1$ of the F_1 branch and peaks at $N = 3$ in the F_2 branch. In addition, rotational states above $N = 10$ are negligibly populated. This finding should be compared to the nascent rotational population distribution of H_2O_2, which seems to be fundamentally different, see e.g. figure 3.2 for 193 nm photodissociation. This deviation in rotational distribution of generated OH photofragments could potentially be utilized to distinguish between OH generated from photolysis of HO_2 and OH photofragments stemming from H_2O_2. For flame studies, it would be advantageous to probe from high N-values, such as $N = 12$ for 193 nm H_2O_2 photolysis, due to the low natural OH fractional population. Regarding OH photofragments from HO_2, they apparently have a rotational population which more resembles that of natural OH, and hence, it would not be possible to suppress the signal from natural OH to the same extent as for H_2O_2.

Apart from possibly providing means of species specific measurements, probing the nascent photofragment population will minimize the interference that was observed in the product zone in the measurements presented in paper VII since the interference is due to chemical reactions. It can be clearly seen in figure 7.11b that the interference signal approaches zero for short pump-probe delay times. If the signal-to-noise ratio allows single-shot imaging, having minor interference would make measurements in turbulent flames possible. Picosecond excitation also minimizes rotational repopulation in the ground state of OH during excitation. Yet another advantage is that it allows short-pulse time gated detection in order to minimize the effects of collisional quenching of $OH(A^2\Sigma^+)$ on the detected signal.

However, ns excitation may be sufficient for ignition studies. Simulations predict a time period prior to ignition, when the OH concentration is significantly lower than the concentrations of H_2O_2 and HO_2. Under such conditions PF-LIF as applied in the experimental work presented in this thesis could be performed without subtraction of signal contributions from natural OH, which would increase the sensitivity and accuracy of the technique. In addition, interferences originating from photodissociation of CO_2, or any other product species, would not be an issue prior to ignition.

Another way of applying PF-LIF that could potentially provide species specificity is vibrationally mediated photodissociation followed by LIF on the generated photofragments. The idea behind this technique is that the photodissociation pulse is of a wavelength of insufficient energy to photodissociate a species which is not in a high lying vibrational state. For this technique to be practically applicable, it is probably important to be able to selectively vibrationally excite different species. Vibrationally mediated photodissociation of H_2O_2 has been studied, see [162–164] for a few examples.

Yet another important and interesting step would be to investigate the possibilities of using a UV LED for probing the OH photofragments. The aim would be to create a PF-LIF sensor for industrial applications. The main issue, as was mentioned in section 5.2, is whether sufficiently intense fluorescence can be induced by an LED. Any effort put into this study may, however, not be in vain even if it turns out it does not work in practical situations. With the development of diode lasers in the wavelength regions $\sim$308 nm and $\sim$282 nm, the shortcomings of UV LEDs will be bypassed.

Finally, it is worth mentioning that *ab initio* calculations predict bound electronic states for H_2O_2 in the VUV region [53]. If these states could be excited through multiphoton excitation and emit fluorescence or phosphorescence that is sufficiently Stokes shifted not to be in the VUV, direct detection of H_2O_2 through multiphoton LIF could be applied. This idea is, however, very much speculative, and the other suggestions presented in this chapter are more likely to be practically useful for diagnostics.

Chapter 9

Conclusions

This thesis presents PF-LIF measurements applied to H_2O_2 and HO_2. The primary focus has been on indirect visualization and measurement of H_2O_2 concentrations. However, in the flame studies it turned out that HO_2 was the primary source of OH photofragments.

The first experiments aimed at ascertaining whether PF-LIF could be a feasible optical measurement technique for visualization of H_2O_2 in mixtures with N_2, O_2 and water vapor. It was shown that H_2O_2 number densities on the order of $\sim 7.5 \cdot 10^{14}$ cm^{-3} could be observed in single shot, and that the PF-LIF signal was proportional to the H_2O_2 concentration for short pump-probe delay times. It has been verified that non-steady flow structures can be captured in single-shot acquisitions.

A second set of experiments were carried out in order to target the behavior of the chemical consumption of OH photofragments following photodissociation in systems initially made up of H_2O_2 and H_2O in mixture with N_2 and O_2. It was found that the rate of OH consumption increased with increasing photolysis fluence. Comparison between measurements and calculations demonstrated that the observed increase in OH consumption rate could be explained by including more reactions than just $OH + H_2O_2 \rightarrow HO_2 + H_2O$. The three most important reactions to consider in addition to the one already mentioned are:
$OH + OH + M \rightarrow H_2O_2 + M$
$OH + OH \rightarrow H_2O + O$
$OH + HO_2 \rightarrow H_2O + O_2$

The second study was an important advance in order to be able to apply the PF-LIF scheme for quantitative H_2O_2 concentration measurements, which it has been successfully used for in an industrial application since publication of the results from the second study (paper V). Photofragmentation laser-induced fluorescence using the current setup has also been demonstrated to work well for 2D imaging in industrial injection studies, even though development in lasers and instrumentation could potentially yield much better PF-LIF setups for industrial applications.

The PF-LIF technique was used for measurements in laminar, premixed flames.

These measurements were challenging for many reasons. The observed signal stemming from OH photofragments were most often obscured by a much stronger signal contribution from natural OH. This latter contribution had to be subtracted by recording two images, one with both the photolysis laser and the probe laser fired, and one with only the probe laser fired. The latter image was then subtracted from the former. Averaging was required; hence, the current application of PF-LIF is probably suited only for laminar flames. Moreover, an interference signal was observed in the reaction and product zones of the studied methane flames. The technique, as currently applied, requires spatial separation of pre-combustion species, intermediate species and post-combustion species, putting further limitations on measurements in non-stable flames, where reactants, intermediates and products mix.

The flame studies unveiled that the observed interference signal was most likely dominated by photofragmentation of CO_2 into $CO + O$ followed by reactions between generated O atoms with H_2 and H_2O. This conclusion is supported by the fact that the interference is absent for hydrogen flames, but appears if CO_2 is seeded into the flames. In addition, the detailed Konnov C/H/N/O mechanism predicts a buildup of OH similar to what is observed experimentally for the studied CH_4/air flames. In general, it can be stated that measured photofragment profiles show good agreement with profiles calculated using the Konnov mechanism.

A certain amount of work has been directed towards development of a wide-field scheme for fluorescence lifetime imaging. This work resulted in a conceptually new method, which has been experimentally verified to measure fluorescence lifetimes of less than 1 ns in single-shot acquisitions. The two main advantages with this technique compared to comparable methods are that the entire signal may be integrated, i.e. photons reaching the cameras do not have to be discarded, and no approximations are involved, except for the fact that the fluorescence decay is assumed to be single exponential. Using the lifetime imaging concept, it was demonstrated that LIF measurements in flames have to be compensated for differences in fluorescence quantum yield in order even for qualitative interpretations to be correct.

Greek Alphabet

A	α	alpha
B	β	beta
Γ	γ	gamma
Δ	δ	delta
E	ϵ	epsilon
Z	ζ	zeta
H	η	eta
I	ι	iota
K	κ	kappa
Λ	λ	lambda
M	μ	mu
N	ν	nu
Ξ	ξ	xi
O	o	omicron
Π	π	pi
P	ρ	rho
Σ	σ	sigma
T	τ	tau
Υ	υ	upsilon
Φ	ϕ	phi
X	χ	chi
Ψ	ψ	psi
Ω	ω	omega

Acknowledgements

I would like to take the opportunity to express my deepest gratitude to my supervisor *Docent Joakim Bood*. His understanding of physics and enthusiastic approach to laboratory work and research in general has been very inspiring. He has an ability to solve problems and find relevant articles in a way I can only hope to learn some day. With *Joakim's* diverse knowledge, great personality, relaxed style and vast experience I cannot imagine a better mentor. Without his support this thesis would simply not exist. I would also like to thank *Joakim* for being a good friend.

Ulf Lindblad, Tetra Pak Packaging Solutions, and *Professor Marcus Aldén*, Head of the Division of Combustion Physics, are acknowledged for their support and deep commitment as well as for having provided the means required to perform the work presented in this thesis. I would also like to thank *Marcus* and *Ulf* for proof reading manuscripts before submission.

During my time at the Division of Combustion Physics I have met a lot of kind and helpful people, a few of whom I have spent quite some time together with. I would like to particularly thank *Billy Kaldvee*. It has been a pleasure to share office with him over the last five years. Unfortunately I never had the opportunity to collaborate with him in the lab. I would also like to give a very special thanks to *Andreas Ehn*. I am truly grateful for having had the chance to work with him in the lab, where he has shared his vast knowledge about fundamental physics and lab equipment. Both *Billy* and *Andreas* are good and inspiring friends, always willing to help.

I am truly grateful to *Andreas Arvidsson* for being a great friend, who always provides support when needed. *Andreas* is the person who explained simulated annealing to me, and he has provided valuable input regarding some texts in this thesis.

I would like to thank *Bo Li* and *Malin Jonsson* for countless hours in the lab as well as for many enriching conversations. Both *Malin* and *Bo* are very easy to collaborate with and they always have smiles on their lips. I also thank *Christian Brackmann* for many enriching conversations. Unfortunately *Christian* joined *Joakim's* research group quite recently so I never had the chance to work with him.

I would like to express my appreciation to *Professor Per-Erik Bengtsson*. It is always a pleasure to talk to him, and he has a deep commitment to making the Division an exciting place to work at with sport activities and other elements besides work.

I am thoroughly indebted to *Professor Alexander Konnov*, who has helped me with questions related to chemistry on several occasions. He possesses extensive knowledge, which he is always willing to share. It has always been a pleasure to talk to him. Also *Frederik Ossler* is acknowledged for interesting discussions, mainly concerning molecular physics. *Mattias Richter* and *Zhongshan Li* are acknowledged for assistance on laser related issues. Their experience with lasers has been irreplaceable on several occasions. I would also like to thank both *Mattias* and *Zhongshan* for many interesting conversations.

Andreas Lantz, *Christoph Knappe*, *Edouard Berrocal*, *Eric Baudoin*, *Holger Grosshans*, *Piero Iudiciani*, *Ronald Whiddon* and *Tobias Joelsson* have been great friends both at and off from work and I am very grateful for that. I would also like to take the opportunity to direct a special thanks to *Ronald* for proof reading my thesis. *Ronald* is a very knowledgeable and entertaining person, to whom it is always a pleasure to speak or listen to. A special thanks is also given to *Sven-Inge Möller*. He always has a laugh, and it is thus always a pleasure to talk to him. He is also very interested in all fields of research and takes his time to participate and assist in science-related conversations.

I am indebted to *David Sedarsky* and *Jonathan Johnsson* for computer related assistance on several occasions. In addition, it is always very interesting to discuss various matters with *David* and *Jonathan*. I am also indebted to the current and former staff at the Division of Combustion Physics. *Minna Ramkull*, *Cecilia Bille*, *Eva Persson*, *Anneli Nilsson Ahlm*, *Rutger Lorensson*, *Susanne Dunér*, *Nina Mårtensson*, *Sara Holmgren*, *Åke Johansson* and *Thomas Wendel* have helped me with all kinds of different matters throughout my time here. Without them this work would not have been possible.

I would also like to thank my current and former colleagues at the Division of Combustion Physics that I have not already mentioned. *Alexis Bohlin*, *Anna-Lena Sahlberg*, *Elias Kristensson*, *Elna Heimdal Nilsson*, *Emil Nordström*, *Fredrik Vestin*, *Gustaf Särner*, *Henrik Bladh*, *Jenny Nauclér*, *Jimmy Olofsson*, *Joakim Rosell*, *Johan Sjöholm*, *Johan Zetterberg*, *Johannes Lindén*, *Karl Netzell*, *Linda Vallenhag*, *Martin Linvin*, *Martin Tunér*, *Nils-Erik Olofsson*, *Per Petersson*, *Rikard Wellander*, *Robert Collin*, *Sven-Göran Pettersson*, *Vladimir Alekseev* and *Zhiwei Sun* have all contributed to making the Division of Combustion Physics a pleasant place to work at.

At Tetra Pak Packaging Solutions AB I have met many nice and knowledgeable persons. I greatly acknowledge *Fredrik Hellqvist*, consultant from Sydteknik, for irredeemable assistance with the two test rigs at Tetra Pak as well as for many interesting and entertaining chats in the lab. *Jimmy Ahlberg* is acknowledged for rig assistance, especially regarding the water rig, and for many amusing conversations. However, I would also like thank *Jimmy* for providing me with CAD drawings of the gas rig and the active nozzle. I thank *Alaa Omrane* and *Hans Seyfried* for being great friends and for providing valuable input and assistance in the lab at Tetra Pak. Both *Hans* and *Alaa* are also acknowledged for providing invaluable input regarding some texts in the thesis.

Antonio Zannini, Flow group manager, *Michael Olsson*, *Jenny Olsson*, *Mårten Regner*, *Fredrik Carlsson*, *Madeleine Jonsson*, *Dragos Moroianu* and all the other people in or in connection with the Flow group at Tetra Pak Packaging Solutions are acknowledged for assistance on flow-related issues as well as for all the interest they have shown in this project. I would also like to thank *Laurence Mott*, Vice President of Packaging Technology at Tetra Pak, who initiated the project which led to this thesis.

Finally I want to direct my deepest gratitude to my mother *Sigrid*, *Håkan* and my younger brother *Dan* for their endless support and assistance whenever I need it. I also greatly appreciate all the support and friendship from the rest of my family and all of my friends.

References

[1] Jones, C.W. *Applications of hydrogen peroxide and derivatives*. Royal Society of Chemistry, Cambridge, 1999.

[2] Logan, J.A., Prather, M.J., Wofsy, S.C., and McElroy, M.B. *Tropospheric chemistry: a global perspective*. Journal of Geophysical Research, **86**(C8):7210–7254, 1981.

[3] Kleinman, L.I. *Photochemical formation of peroxides in the boundary layer*. Journal of Geophysical Research, **91**(D10):10889–10904, 1986.

[4] Finlayson-Pitts, B.J. and Pitts Jr., J.N. *Chemistry of the upper and lower atmosphere*. Elsevier Science & Technology, London, 2000.

[5] Thomas, D., Colle, S., and Vanderschuren, J. *Kinetics of SO_2 absorption into fairly concentrated sulphuric acid solutions containing hydrogen peroxide*. Chemical Engineering and Processing, **42**(6):487–494, 2003.

[6] Lee, M., Heikes, B.G., and O'Sullivan, D.W. *Hydrogen peroxide and organic hydroperoxide in the troposphere: a review*. Atmospheric Environment, **34**(21):3475–3494, 2000.

[7] Slemr, F., Harris, G.W., Hastie, D.R., Mackay, G.I., and Schiff, H.I. *Measurement of gas phase hydrogen peroxide in air by tunable diode laser absorption spectroscopy*. Journal of Geophysical Research, **91**(D5):5371–5378, 1986.

[8] Baardsen, E.L. and Terhune, R.W. *Detection of OH in the atmosphere using a dye laser*. Applied Physics Letters, **21**(5):209–211, 1972.

[9] Hard, T.M., O'brien, R.J., Chan, C.Y., and Mehrabzadeh, A.A. *Tropospheric free radical determination by FAGE*. Environmental Science & Technology, **18**(10):768–777, 1984.

[10] Whalley, L.K., Furneaux, K.L., Goddard, A., Lee, J.D., Mahajan, A., Oetjen, H., Read, K.A., Kaaden, N., Carpenter, L.J., Lewis, A.C., Plane, J.M.C., Saltzman, E.S., Wiedensohler, A., and Heard, D.E. *The chemistry of OH and HO_2 radicals in the boundary layer over the tropical Atlantic ocean*. Atmospheric Chemistry and Physics, **10**(4):1555–1576, 2010.

[11] Parker, A.E., Jain, C., Schoemaecker, C., Szriftgiser, P., Votava, O., and Fittschen, C. *Simultaneous, time-resolved measurements of OH and* HO_2 *radicals by coupling of high repetition rate LIF and cw-CRDS techniques to a laser photolysis reactor and its application to the photolysis of* H_2O_2. Applied Physics B-Lasers and Optics, 2010, doi:10.1007/s00340-010-4225-1.

[12] Thiebaud, J., Sabine, C., and Fittschen, C. *Measurements of line strengths in the* $2\nu_1$ *band of the* HO_2 *radical using laser photolysis/continuous wave cavity ring-down spectroscopy (cw-CRDS).* Journal of Physical Chemistry, **111**(30):6959–6966, 2007.

[13] Warnatz, J., Maas, U., and Dibble, R.W. *Combustion-physical and chemical fundamentals, modeling and simulation, experiments, pollutant formation.* Springer-Verlag, Heidelberg, 4 edn., 2006.

[14] Anderson, W.R., Decker, L.J., and Kotlar, A.J. *Concentration profiles of NH and OH in a stoichiometric* CH_4/N_2O *flame by laser excited fluorescence and absorption.* Combustion and Flame, **48**(2):179–190, 1982.

[15] Lucht, R.P., Sweeney, D.W., Laurendeau, N.M., Drake, M.C., Lapp, M., and Pitz, R.W. *Single-pulse, laser-saturated fluorescence measurements of OH in turbulent nonpremixed flames.* Optics Letters, **9**(3):90–92, 1984.

[16] Jeffries, J.B., Kose-Höinghaus, K., Smith, G.P., Copeland, R.A., and Crosley, D.R. *Rotational-level-dependent quenching of* $OH(A^2\Sigma^+)$ *at flame temperatures.* Chemical Physics Letters, **152**(2,3):160–166, 1988.

[17] Laurendeau, N.M. and Goldsmith, J.E.M. *Comparison of hydroxyl concentration profiles using 5 laser-induced fluorescence methods in a lean subatmospheric-pressure* $H_2/O_2/Ar$ *flame.* Combustion Science and Technology, **63**:139–152, 1989.

[18] Barlow, R.S., Dibble, R.W., and Lucht, R.P. *Simultaneous measurement of Raman scattering and laser-induced OH fluorescence in nonpremixed turbulent jet flames.* Optics Letters, **14**(5):263–265, 1989.

[19] Schäfer, M., Ketterle, W., and Wolfrum, J. *Saturated 2D-LIF of OH and 2D determination of effective collisional lifetimes in atmospheric pressure flames.* Applied Physics B-Photophysics and Laser Chemistry, **52**(5):341–346, 1991.

[20] Heard, D.E., Jeffries, J.B., Smith, G.P., and Crosley, D.R. *LIF measurements in methane/air flames of radicals important in prompt-NO formation.* Combustion and Flame, **88**(2):137–148, 1992.

[21] Bernstein, J.S., Fein, A., Choi, J.B., Cool, T.A., Sausa, R.C., Howard, S.L., Locke, R.J., and Miziolek, A.W. *Laser-based flame species profile measurements: a comparison with flame model predictions.* Combustion and Flame, **92**(1-2):85–105, 1993.

[22] Köllner, M. and Monkhouse, P. *Time-resolved LIF of OH in the flame front of premixed and diffusion flames at atmospheric pressure.* Applied Physics B-Lasers and Optics, **61**(5):499–503, 1995.

[23] Battles, B.E. and Hanson, R.K. *Laser-induced fluorescence measurements of NO and OH mole fraction in fuel-lean, high-pressure (1-10 atm) methane flames: fluorescence modeling and experimental validation.* Journal of quantitative spectroscopy & radiative transfer, **54**(3):521–537, 1995.

[24] Atakan, B., Heinze, J., and Meier, U.E. *OH laser-induced fluorescence at high pressures: spectroscopic and two-dimensional measurements exciting the A-X (1,0) transition.* Applied Physics B-Lasers and Optics, **64**(5):585–591, 1997.

[25] Beaud, P., Radi, P.P., Franzke, D., Frey, H.M., Mischler, B., Tzannis, A.P., and Gerber, T. *Picosecond investigation of the collisional deactivation of OH* $A^2\Sigma^+ \, (v' = 1, N' = 4, 12)$ *in an atmospheric-pressure flame.* Applied Optics, **37**(15):3354–3367, 1998.

[26] Kose-Höinghaus, K. *Laser techniques for the quantitative detection of reactive intermediates in combustion systems.* Progress in Energy and Combustion Science, **20**(3):203–279, 1994.

[27] GRI-Mech, Web site, http://www.me.berkeley.edu/gri-mech.

[28] Konnov, A.A. *Implementation of the NCN pathway of prompt-NO formation in the detailed reaction mechanism.* Combustion and Flame, **156**(11):2093–2105, 2009.

[29] Salooja, K.C. *The degenerate chain branching intermediate in hydrocarbon combustion: some evidence from studies on the isomeric hexanes.* Combustion and Flame, **9**(3):219–227, 1965.

[30] Pitz, W.J. and Westbrook, C.K. *Chemical kinetics of the high pressure oxidation of n-butane and its relation to engine knock.* Combustion and Flame, **63**(1-2):113–133, 1986.

[31] Michael, J.V., Sutherland, J.W., Harding, L.B., and Wagner, A.F. *Initiation in* H_2/O_2*: rate constants for* $H_2 + O_2 \rightarrow H + HO_2$ *at high temperature.* Proceedings of the Combustion Institute, **28**:1471–1478, 2000.

[32] Swartling, P. and Lindgren, B. *The sterilizing effect against Bacillus subtilis spores of hydrogen peroxide at different temperatures and concentrations.* Journal of Dairy Research, **35**(3):423–428, 1968.

[33] Toledo, R.T., Escher, F.E., and Ayres, J.C. *Sporicidal properties of hydrogen peroxide against food spoilage organisms.* Applied Microbiology, **26**(4):592–597, 1973.

[34] Smith, Q.J. and Brown, K.L. *The resistance of dry spores of Bacillus subtilis var. globigii (NCIB 8058) to solutions of hydrogen peroxide in relation to aseptic packaging.* Journal of Food Technology, **15**(2):169–179, 1980.

[35] Toledo, R.T. *Chemical sterilants for aseptic packaging.* Food Technology, **29**(5):102–112, 1975.

[36] Yoshpe-Purer, Y. and Eylan, E. *Disinfection of water by hydrogen peroxide.* Health Laboratory Science, **5**(4):233–238, 1968.

[37] Rosenzweig, A.L. *Hydrogen peroxide in prevention of water contamination.* The Lancet, **311**(8070):944, 1978.

[38] Wardle, M.D. and Renninger, G.M. *Bacterial effect of hydrogen peroxide on spacecraft isolates.* Applied Microbiology, **30**(4):710–711, 1975.

[39] Wang, J. and Toledo, R.T. *Sporicidal properties of mixtures of hydrogen peroxide vapor and hot air.* Food Technology, **40**(12):60–67, 1986.

[40] Klapes, N.A. and Vesley, D. *Vapor-phase hydrogen peroxide as a surface decontaminant and sterilant.* Applied and Environmental Microbiology, **56**(2):503–506, 1990.

[41] Alfa, M.J., DeGagne, P., Olson, N., and Puchalski, T. *Comparison of ion plasma, vaporized hydrogen peroxide, and 100% ethylene oxide sterilizers to the 12/88 ethylene oxide gas sterilizer.* Infection Control and Hospital Epidemiology, **17**(2):92–100, 1996.

[42] Ikarashi, Y., Tsuchiya, T., and Nakamura, A. *Cytotoxicity of medical materials sterilized with vapour-phase hydrogen peroxide.* Biomaterials, **16**(3):177–183, 1995.

[43] Chung, S., Kern, R., Koukol, R., Barengoltz, J., and Cash, H. *Vapor hydrogen peroxide as alternative to dry heat microbial reduction.* Advances in Space Research, **42**(6):1150–1160, 2008.

[44] Corveleyn, S., Vandenbossche, G.M.R., and Remon, J.P. *Near-infrared (NIR) monitoring of H_2O_2 vapor concentration during vapor hydrogen peroxide (VHP) sterilization.* Pharmaceutical Research, **14**(3):294–298, 1997.

[45] Adams, D., Brown, G.P., Fritz, C., and Todd, T.R. *Calibration of a near-infrared (NIR) H_2O_2 vapor monitor.* Pharmaceutical Engineering, **18**(3):1–11, 1998.

[46] Hunt, R.H., Leacock, R.A., Peters, C.W., and Hecht, K.T. *Internal-rotation in hydrogen peroxide: the far infrared spectrum and the determination of the hindering potential.* Journal of Chemical Physics, **42**(6):1931–1946, 1965.

[47] Flaud, J.M., Camy-Peyret, C., Johns, J.W.C., and Carli, B. *The far infrared spectrum of H_2O_2. First observation of the staggering of the levels and determination of the cis barrier.* Journal of Chemical Physics, **91**(3):1504–1510, 1989.

[48] Lin, S.Y. and Guo, H. *Exact quantum mechanical calculations of rovibrational energy levels of hydrogen peroxide (HOOH).* Journal of Chemical Physics, **119**(12):5867–5873, 2003.

[49] Bitencourt, A.C.P., Ragni, M., Maciel, G.S., Aquilanti, V., and Prudente, F.V. *Level distributions, partition functions, and rates of chirality changing processes for the torsional mode around O-O bonds.* Journal of Chemical Physics, **129**(15):154316, 2008.

[50] Koput, J., Carter, S., and Handy, N.C. *Ab initio prediction of the vibrational-rotational energy levels of hydrogen peroxide and its isotopomers.* Journal of Chemical Physics, **115**(18):8345–8350, 2001.

[51] Halpern, A.M. and Glendening, E.D. *An intrinsic reaction coordinate calculation of the torsion-internal rotation potential of hydrogen peroxide and its isotopomers.* Journal of Chemical Physics, **121**(1):273–279, 2004.

[52] Drozd, G.T., Melnichuk, A., and Donahue, N.M. *The HOOH uv spectrum: importance of the transition dipole moment and torsional motion from semiclassical calculations on an ab initio potential energy surface.* Journal of Chemical Physics, **132**(8):084304, 2010.

[53] Liu, Y.J., Persson, P., and Lunell, S. *Theoretical study of the photodissociation of low lying excited states of hydrogen peroxide.* Molecular Physics, **102**(23-24):2575–2584, 2004.

[54] Helminger, P., Bowman, W.C., and De Lucia, F.C. *A study of the rotational-torsional spectrum of hydrogen peroxide between 80 and 700 GHz.* Journal of Molecular Spectroscopy, **85**(1):120–130, 1981.

[55] Bowman, W., De Lucia, F.C., and Helminger, P. *The higher K_{-1} states of hydrogen peroxide.* Journal of Molecular Spectroscopy, **87**(2):571–574, 1981.

[56] Petkie, D.T., Goyette, T.M., Holton, J.J., De Lucia, F.C., and Helminger, P. *Millimeter/submillimeter-wave spectrum of the first excited torsional state in HOOH.* Journal of Molecular Spectroscopy, **171**(1):145–159, 1995.

[57] Camy-Peyret, C., Flaud, J.M., Johns, J.W.C., and Noël, M. *Torsion-vibration interaction in H_2O_2: first high-resolution observation of ν_3^1.* Journal of Molecular Spectroscopy, **155**(1):84–104, 1992.

[58] Perrin, A., Flaud, J.M., Camy-Peyret, C., Schermaul, R., Winnewisser, M., Mandin, J.Y., Dana, V., Badaoui, M., and Koput, J. *Line intensities in the far-infrared spectrum of H_2O_2.* Journal of Molecular Spectroscopy, **176**(2):287–296, 1996.

[59] Hillman, J.J., Jennings, D.E., Olson, W.B., and Goldman, A. *High-resolution infrared spectrum of hydrogen peroxide: the* ν_6 *fundamental band.* Journal of Molecular Spectroscopy, **117**(1):46–58, 1986.

[60] Perrin, A., Flaud, J.M., Camy-Peyret, C., Goldman, A., Murcray, F.J., and Blatherwick, R.D. *New analysis of the* ν_6 *band of* HO_2*: the (n, τ) = (0, 1), (1, 1), (2, 1), (0, 3) and (1, 3) torsional subbands.* Journal of Molecular Spectroscopy, **142**(1):129–147, 1990.

[61] Perrin, A., Valentin, A., Flaud, J.M., Camy-Peyret, C., Schriver, L., Schriver, A., and Arcas, P. *The 7.9-μm band of hydrogen peroxide: line positions and intensities.* Journal of Molecular Spectroscopy, **171**(2):358–372, 1995.

[62] Redington, R.L., Olson, W.B., and Cross, P.C. *Studies of hydrogen peroxide: the infrared spectrum and the internal rotation probleml.* Journal of Chemical Physics, **36**(5):1311–1326, 1962.

[63] Olson, W.B., Hunt, R.H., Young, B.W., Maki, A.G., and W., B.J. *Rotational constants of the lowest torsional component (0G) of the ground state and lowest torsional component (1G) of the first excited torsional state of hydrogen peroxide.* Journal of Molecular Spectroscopy, **127**(1):12–34, 1988.

[64] Cook, W.B., Hunt, R.H., Shelton, W.N., and Flaherty, A. *Torsion-rotation energy levels, hindering potential, and internal parameters of the first excited vibrational state of the antisymmetric O-H stretch in hydrogen peroxide.* Journal of Molecular Spectroscopy, **171**(1):91–112, 1995.

[65] Rogers, J. and Hillman, J.J. *Prediction of absolute infrared intensities for the fundamental vibrations of* H_2O_2. Journal of Chemical Physics, **75**(3):1085–1090, 1981.

[66] Rogers, J.D. and Hillman, J.J. *Ab initio calculation of infrared intensities for hydrogen peroxide.* Journal of Chemical Physics, **76**(8):4046–4055, 1982.

[67] Koput, J. *On the* r_0^* *structure and the torsional potential function of hydrogen peroxide.* Journal of Molecular Spectroscopy, **115**(2):438–441, 1986.

[68] Harding, L.B. *Theoretical studies of the hydrogen peroxide potential surface. 1. An ab initio anharmonic force field.* Journal of Physical Chemistry, **93**(24):8004–8013, 1989.

[69] Harding, L.B. *Theoretical studies of the hydrogen peroxide potential surface. 2. An ab initio, long-range,* $OH(^2\Pi) + OH\,(^2\Pi)$ *potential.* Journal of Physical Chemistry, **95**(22):8653–8660, 1991.

[70] Koput, J. *An ab initio study on the equilibrium structure and torsional potential energy function of hydrogen peroxide.* Chemical Physics Letters, **236**(4-5):516–520, 1995.

[71] Koput, J., Carter, S., and Handy, N.C. *Potential energy surface and vibrational-rotational energy levels of hydrogen peroxide.* Journal of Physical Chemistry, **102**(31):6325–6330, 1998.

[72] Pitsevich, G.A., Shundalau, M.B., and Umreiko, D.S. *Calculation of torsional and rotational raman spectra of hydrogen peroxide.* Journal of Applied Spectroscopy, **77**(1):45–54, 2010.

[73] Dellepiane, G., Gussoni, M., and Hougen, J.T. *Hamiltonian, symmetry group, and vibrational coordinates for the nonrigid molecule* $CXY_2-C{\equiv}C-CXY_2$. Journal of Molecular Spectroscopy, **47**(3):515–530, 1973.

[74] Wilson Jr., E.B., Decius, J.C., and Cross, P.C. *Molecular vibrations the theory of infrared and raman vibrational spectra.* Dover publications, inc., New York, 1955.

[75] Meal, J.H. and Polo, S.R. *Vibration-rotation interaction in polyatomic molecules. I. The Zeta Matrices.* Journal of Chemical Physics, **24**(6):1119–1125, 1956.

[76] DeMore, W.B., Sander, S.P., Golden, D.M., Hampson, R.F., Kurylo, M.J., Howard, C.J., Ravishankara, A.R., Kolb, C.E., and Molina, M.J. *Chemical kinetics and photochemical data for use in stratospheric modeling, Evaluation No. 12.* JPL Publication, **97-4**, 1997.

[77] Grunewald, A.U., Gericke, K.H., and Comes, F.J. *Photofragmentation dynamics of hydrogen peroxide: analysis of two simultaneously excited states.* Journal of Chemical Physics, **87**(10):5709–5721, 1987.

[78] Gericke, K.H., Klee, S., Comes, F.J., and Dixon, R.N. *Dynamics of* H_2O_2 *photodissociation: OH product state and momentum distribution characterized by sub-Doppler and polarization spectroscopy.* Journal of Chemical Physics, **85**(8):4463–4479, 1986.

[79] Klee, S., Gericke, K.H., and Comes, F.J. *Doppler spectroscopy of OH in the photodissociation of hydrogen peroxide.* Journal of Chemical Physics, **85**(1):40–44, 1986.

[80] Baek, S.J., Shin, S.K., Park, C.R., and Kim, H.L. *Photodissociation dynamics of* H_2O_2 *at 280-290 nm.* Bulletin of the Korean Chemical Society, **16**(3):256–260, 1995.

[81] Brouard, M., Martinez, M.T., Milne, C.J., Simons, J.P., and Wang, J.X. *Near threshold stereo-dynamics of molecular photodissociation: the visible and near ultraviolet photodissociation of* H_2O_2. Chemical Physics Letters, **165**(5):423–428, 1990.

[82] Atkinson, R., Baulch, D.L., Cox, R.A., Crowley, J.N., Hampson, R.F., Hynes, R.G., Jenkin, M.E., Rossi, M.J., and Troe, J. *Evaluated kinetic and photochemical data for atmospheric chemistry: volume I - gas phase reactions of* O_x, HO_x, NO_x *and* SO_x *species.* Atmospheric Chemistry and Physics, **4**:1461–1738, 2004.

[83] Thiebaud, J., Aluculesei, A., and Fittschen, C. *Formation of HO_2 radicals from the photodissociation of H_2O_2 at 248 nm.* Journal of Chemical Physics, **126**(18):186101, 2007.

[84] Jacobs, A., Wahl, M., Weller, R., and Wolfrum, J. *Rotational distribution of nascent OH radicals after H_2O_2 photolysis at 193 nm.* Applied Physics B-Photophysics and Laser Chemistry, **42**(3):173–179, 1987.

[85] Grunewald, A.U., Gericke, K.H., and Comes, F.J. *Influence of H_2O_2 internal motion on scalar and vector properties of OH photofragments.* Journal of Chemical Physics, **89**(1):345–354, 1988.

[86] Schinke, R. *Rotational distributions in direct molecular photodissociation.* Annual Review of Physical Chemistry, **39**:39–68, 1988.

[87] Schinke, R. and Staemmler, V. *Photodissociation dynamics of H_2O_2 at 193 nm: an example of the rotational reflection principle.* Chemical Physics Letters, **145**(6):486–492, 1988.

[88] Schinke, R. *Angular momentum correction in the photodissociation of H_2O_2 at 193 nm.* Journal of Chemical Physics, **92**(14):4015–4019, 1988.

[89] Cai, Z.T., Zhang, D.H., and Zhang, J.Z. *Quantum dynamical studies for photodissociation of H_2O_2 at 248 nm and 266 nm.* Journal of Chemical Physics, **100**(8):5631–5638, 1994.

[90] Schinke, R. *Photodissociation dynamics.* Cambridge University Press, Cambridge, 1993.

[91] Watts, J.D. and Francisco, J.S. *Ground and electronically excited states of methyl hydroperoxide: comparison with hydrogen peroxide.* Journal of Chemical Physics, **125**(10):104301, 2006.

[92] Ondrey, G., van Veen, N., and Bersohn, R. *The state distribution of OH radicals photodissocated from H_2O_2 at 193 and 248 nm.* Journal of Chemical Physics, **78**(6):3732–3737, 1983.

[93] Jacobs, A., Kleinermanns, K., Kuge, H., and Wolfrum, J. *OH($X^2\Pi$ state distribution from HNO_3 and H_2O_2 photodissociation at 193 nm.* Journal of Chemical Physics, **79**(6):3162–3163, 1983.

[94] Gölzenleuchter, H., Gericke, K.H., and Comes, F.J. *State-selected photofragments from two-photon excitation of H_2O_2 at 193 nm.* Chemical Physics Letters, **116**(1):61–65, 1985.

[95] Klee, S., Gericke, K.H., Gölzenleuchter, H., and Comes, F.J. *2-Photon excitation of hydrogen peroxide at 266 and 193 nm: determination of the absorption cross section and photofragment state distribution.* Chemical Physics, **139**(2-3):415–425, 1989.

[96] Kinsey, J.L. *Laser-induced fluorescence*. Annual Review of Physical Chemistry, **28**:349–372, 1977.

[97] Altkorn, R. and Zare, R.N. *Effects of saturation on laser-induced fluorescence measurements of population and polarization*. Annual Review of Physical Chemistry, **35**:265–289, 1984.

[98] Daily, J.W. *Laser induced fluorescence spectroscopy in flames*. Progress in Energy and Combustion Science, **23**(2):133–199, 1997.

[99] Amorim, J., Baravian, G., and Jolly, J. *Laser-induced resonance fluorescence as a diagnostic technique in non-thermal equilibrium plasmas*. Journal of Physics D - Applied Physics, **33**(9):R51–R65, 2000.

[100] Johnson, M.E. and Landers, J.P. *Fundamentals and practice for ultrasensitive laser-induced fluorescence detection in microanalytical systems*. Electrophoresis, **25**(21-22):3513–3527, 2004.

[101] Bransden, B.H. and Joachain, C.J. *Physics of atoms and molecules*. Pearson Education Limited, Harlow, 1983.

[102] Luque, J. and Crosley, D.R. *LIFBASE: database and spectral simulation program (version 1.5)*. SRI International Report MP 99-009, 1999.

[103] van der Loo, M.P.J. and Groenenboom, G.C. *Ab initio calculations of (2+1) resonance enhanced multiphoton ionization spectra and lifetimes of the (D,3)$^2\Sigma^-$ states of OH and OD*. Journal of Chemical Physics, **123**(7):074310, 2005.

[104] Herzberg, G. *Molecular spectra and molecular structure. I Spectra of diatomic molecules*. D. van Nostrand company, inc., Toronto, 2 edn., 1950.

[105] Luque, J. and Crosley, D.R. *Transition probabilities in the $A^2\Sigma^+ - X^2\Pi_i$ electronic system of OH*. Journal of Chemical Physics, **109**(2):439–448, 1998.

[106] Parlant, G. and Yarkony, D.R. *A theoretical analysis of the state-specific decomposition of OH$(A^2\Sigma^+, v', N', F_1/F_2)$ levels, including the effects of spin-orbit and Coriolis interactions*. Journal of Chemical Physics, **110**(1):363–376, 1999.

[107] Brzozowski, J., Erman, P., and Lyyra, M. *Precision estimates of the predissociation rates of the OH $A^2\Sigma$ state (≤ 2)*. Physica Scripta, **17**(5):507–511, 1978.

[108] Spaanjaars, J.J.L., ter Meulen, J.J., and G., M. *Relative predissociation rates of OH $A^2\Sigma^+, v' = 3$ from combined cavity ring down - laser-induced fluorescence measurements*. Journal of Chemical Physics, **107**(7):2242–2248, 1997.

[109] Heard, D.E., Crosley, D.R., Jeffries, J.B., Smith, G.P., and Hirano, A. *Rotational level dependence of predissociation in the $v' = 3$ level of OH $A^2\Sigma^+$*. Journal of Chemical Physics, **96**(6):4366–4371, 1992.

[110] Julienne, P.S., Krauss, M., and Donn, B. *Formation of OH through inverse predissociation*. The Astrophysical Journal, **170**(1):65–70, 1971.

[111] Rothe, E.W., Gu, Y.W., , and Reck, G.P. *Laser-induced predissociative fluorescence: dynamics and polarization and the effect of lower-state rotational energy transfer on quantitative diagnostics*. Applied Optics, **35**(6):934–947, 1996.

[112] Brown, J. and Carrington, A. *Rotational spectroscopy of diatomic molecules*. Cambridge University Press, Cambridge, 2003.

[113] Bernath, P.F. and Colin, R. *Revised molecular constants and term values for the $X^2\Pi$ and $B^2\Sigma^+$ states of OH*. Journal of Molecular Spectroscopy, **257**(1):20–23, 2009.

[114] Langhoff, S.R., Sink, M.L., Pritchard, R.H., and Kern, C.W. *Theoretical study of the spin-orbit coupling in the $X^2\Pi$ state of OH*. Journal of Molecular Physics, **93**(1):200–218, 1982.

[115] Hill, E. and van Vleck, J.H. *On the quantum mechanics of the rotational distortion of multiplets in molecular spectra*. Physical Review, **32**(2):250–272, 1928.

[116] Mulliken, R.S. *The interpretation of band spectra. Parts I, IIa, IIb - Symbols and notation*. Review of Modern Physics, **2**(1):0060–0115, 1930.

[117] Bormann, F., Nielsen, T., Burrows, M., and Andresen, P. *Single-pulse collision-insensitive picosecond planar laser-induced fluorescence of OH $A^2\Sigma^+$ $(v' = 2)$ in atmospheric-pressure flames*. Applied Physics B-Lasers and Optics, **62**(6):601–607, 1996.

[118] van Munster, E.B. and Gadella, T.W.J. *Fluorescence lifetime imaging microscopy (FLIM)*. Advances in Biochemical Engineering/Biotechnology, **95**:143–175, 2005.

[119] Scully, A.D., Ostler, R.B., Phillips, D., O'Neill, P., Townsend, K.M.S., Parker, A.W., and MacRobert, A.J. *Application of fluorescence lifetime imaging microscopy to the investigation of intracellular PDT mechanisms*. Bioimaging, **5**(1):9–18, 1997.

[120] Koban, W., Koch, J.D., Hanson, R.K., and Schulz, C. *Toluene LIF at elevated temperatures: implications for fuel-air ratio measurements*. Applied Physics B-Lasers and Optics, **80**(2):147–150, 2005.

[121] Robinson, T., Valluri, P., Manning, H.B., Owen, D.M., Munro, I. Talbot, C.B., Dunsby, C., Eccleston, J.F., Baldwin, G.S., Neil, M.A.A., de Mello, A.J., and French, P.M.W. *Three-dimensional molecular mapping in a microfluidic mixing device using fluorescence lifetime imaging*. Optics Letters, **33**(16):1887–1889, 2008.

[122] Ni, T. and Melton, L.A. *Two-dimensional gas-phase temperature measurements using fluorescence lifetime imaging*. Applied Spectroscopy, **50**(9):1112–1116, 1996.

[123] Woods, R.J., Scypinski, S., Cline Love, L.J., and Ashworth, H.A. *Transient digitizer for the determination of microsecond luminescence lifetimes*. Analytical Chemistry, **56**(8):1395–1400, 1984.

[124] Kirkpatrick, S., Gelatt Jr., C.D., and Vecchi, M.P. *Optimization by Simulated Annealing*. Science, **220**(4598):671–680, 1983.

[125] Černý, V. *Thermodynamical approach to the traveling salesman problem: an efficient simulation algorithm*. Journal of Optimization Theory and Applications, **45**(1):41–51, 1985.

[126] Rodgers, M.O., Asai, K., and Davis, D.D. *Photofragmentation-laser induced fluorescence: a new method for detecting atmospheric trace gases*. Applied Optics, **19**(21):3597–3605, 1980.

[127] Simeonsson, J.B. and Sausa, R.C. *A critical review of laser photofragmentation/fragment detection techniques for gas-phase chemical analysis*. Applied Spectroscopy Reviews, **31**(1):1–72, 1996.

[128] Simeonsson, J.B. and Sausa, R.C. *Laser photofragmentation/fragment detection techniques for chemical analysis of the gas phase*. Trends in Analytical Chemistry, **17**(8-9):542–550, 1998.

[129] Keyser, L.F. *Absolute rate constant of the reaction* $OH{+}H_2O_2 \longrightarrow HO_2 + H_2O$ *from 245 to 423 K*. Journal of Physical Chemistry, **84**(13):1659–1663, 1980.

[130] Sridharan, U.C., Reimann, B., and Kaufman, F. *Kinetics of the reaction* $OH{+}H_2O_2 \longrightarrow HO_2{+}H_2O$. Journal of Chemical Physics, **73**(3):1286–1293, 1980.

[131] Wine, P.H., Semmes, D.H., and Ravishankara, A.R. *A laser flash photolysis kinetics study of the reaction* $OH{+}\ H_2O_2 \longrightarrow HO_2{+}H_2O$. Journal of Chemical Physics, **75**(9):4390–4395, 1981.

[132] Marinelli, W.J. and Johnston, H.S. *Reaction rates of hydroxyl radical with nitric acid and with hydrogen peroxide*. Journal of Chemical Physics, **77**(3):1225–1234, 1982.

[133] Lamb, J.J., Molina, L.T., Smith, C.A., and Molina, M.J. *Rate constant of the* $OH{+}H_2O_2 \longrightarrow HO_2{+}H_2O$ *reaction*. Journal of Physical Chemistry, **87**(22):4467–4470, 1983.

[134] Vaghjiani, G.L. and Ravishankara, A.R. *Reactions of OH and OD with* H_2O_2 *and* D_2O_2. Journal of Physical Chemistry, **93**(23):7833–7837, 1989.

[135] Lovejoy, E.R., Murrells, T.P., Ravishankara, A.R., and Howard, C.J. *Oxidation of* CS_2 *by reaction with OH. 2. Yields of* HO_2 *and* SO_2 *in oxygen*. Journal of Physical Chemistry, **94**(6):2386–2393, 1990.

[136] Turnipseed, A.A., Vaghjiani, G.L., Gierczak, T., Thompson, J.E., and Ravishankara, A. *The photochemistry of ozone at 193 and 222 nm.* Journal of Chemical Physics, **95**(5):3244–3251, 1991.

[137] Hippler, H. and Troe, J. *Rate constants of the reaction* $OH+H_2O_2 \longrightarrow HO_2+H_2O$ *at* $T\geq 1000$ *K.* Chemical Physics Letters, **192**(4):333–337, 1992.

[138] Vakhtin, A.B., McCabe, D.C., Ravishankara, A.R., and Leone, S.R. *Low-temperature kinetics of the reaction of the OH radical with hydrogen peroxide.* Journal of Physical Chemistry A, **107**(49):10642–10647, 2003.

[139] Atkinson, R., Baulch, D.L., Cox, R.A., Crowley, J.N., Hampson, R.F., Hynes, R.G., Jenkin, M.E., Rossi, M.J., and Troe, J. *Evaluated kinetic and photochemical data for atmospheric chemistry: volume I - gas phase reactions of* O_x, HO_x, NO_x *and* SO_x *species.* Atmospheric Chemistry and Physics, **4**:1461–1738, 2004.

[140] Kulatilaka, W.D., Frank, J.H., Patterson, B.D., and Settersten, T.B. *Analysis of 205-nm photolytic production of atomic hydrogen in methane flames.* Applied Physics B-Lasers and Optics, **97**(1):227–242, 2009.

[141] Raiche, G.A., Crosley, D.R., and Copeland, R.A. *Laser-induced flourescence and dissociation of acetylene in flames.* "Advances in Laser Science IV", American Institute of Physics Conference Proceedings, **191**:758–760, 1989.

[142] Monkhouse, P.B., Gottwald, U.A., Davidsson, K.O., Lönn, B., Engvall, K., and Pettersson, J.B.C. *Phase discrimination of alkali species in PCFB combustion flue gas using simultaneous monitoring by surface ionisation and photofragmentation fluorescence.* Fuel, **82**(4):365–371, 2003.

[143] Hartinger, K.T., Monkhouse, P.B., Wolfrum, J., Baumann, H., and Bonn, B. *Determination of flue gas alkali concentrations in fluidized-bed coal combustion by excimer- laser-induced fragmentation fluorescence.* Proceedings of the Combustion Institute, **25**:193–199, 1994.

[144] Schürmann, H., Monkhouse, P.B., Unterberger, S., and Hein, K.R.G. *In situ parametric study of alkali release in pulverized coal combustion: effects of operating conditions and gas composition.* Proceedings of the Combustion Institute, **31**:1913–1920, 2007.

[145] Osborn, D.L. and Frank, J.H. *Laser-induced fragmentation fluorescence detection of the vinyl radical and acetylene.* Chemical Physics Letters, **349**(1-2):43–50, 2001.

[146] Li, Z.S., Li, B., Sun, Z.W., Bai, X.S., and Aldén, M. *Turbulence and combustion interaction: high resolution local flame front structure visualization using simultaneous single-shot PLIF imaging of CH, OH, and* CH_2O *in a piloted premixed jet flame.* Combustion and Flame, **157**(6):1087–1096, 2010.

[147] Sato, H. *Photodissociation of simple molecules in the gas phase*. Chemical Reviews, **101**(9):2687–2725, 2001.

[148] Underwood, J. and Wittig, C. *Two-photon photodissociation of* H_2O *via the* $\tilde{B}$ *state*. Chemical Physics Letters, **386**(1-3):190–195, 2004.

[149] Jeffries, J.B., Schulz, C., Mattison, D.W., Oehlschlaeger, M.A., Bessler, W.G., Lee, T., Davidson, D.F., and Hanson, R.K. *UV absorption of* CO_2 *for temperature diagnostics of hydrocarbon combustion applications*. Proceedings of the Combustion Institute, **30**:1591–1599, 2005.

[150] Kassner, C., Heinrich, P., Stuhl, F., Couris, S., and Haritakis, S. *Fragments in the UV photolysis of the* CH_3 *and* CH_3O_2 *radicals*. Chemical Physics Letters, **208**(1-2):27–31, 1993.

[151] Hartmann, D., Karthäuser, J., and Zellner, R. *The 248-nm photofragmentation of the* CH_3O_2 *radical*. Journal of Physical Chemistry, **94**(7):2963–2966, 1990.

[152] Sutton, J.A. and Driscoll, J.F. *Rayleigh scattering cross sections of combustion species at 266, 355, and 532 nm for thermometry applications*. Optics Letters, **29**(22):2620–2622, 2004.

[153] Joens, J.A. *A model for the temperature-dependence of the near UV absorption-spectra of organic peroxy-radicals*. Journal of Physical Chemistry, **98**(5):1394–1397, 1994.

[154] Baulch, D.L., Cox, R.A., Hampson, R.F., Kerr, J.A., Troe, J., and Watson, R.T. *Evaluated kinetic and photochemical data for atmospheric chemistry*. Journal of Physical and Chemical Reference Data, **9**(2):295–471, 1980.

[155] Eckbreth, A.C. *Laser diagnostics for combustion temperature and species*. Gordon and Breach Publishers, Amsterdam, 2 edn., 1996.

[156] Schwarzwald, R., Monkhouse, P., and Wolfrum, J. *Picosecond fluorescence lifetime measurement of the OH radical in an atmospheric-pressure flame*. Chemical Physics Letters, **142**(1-2):15–18, 1987.

[157] Meijer, G., ter Meulen, J.J., Andresen, P., and Bath, A. *Sensitive quantum state selective detection of* H_2O *and* D_2O *by* $(2+1)$*-resonance enhanced multiphoton ionization*. Journal of Chemical Physics, **85**(12):6914–6922, 1986.

[158] Neij, H. and Aldén, M. *Application of two-photon laser-induced fluorescence for visualization of water vapor in combustion environments*. Applied Optics, **33**(27):6514–6523, 1994.

[159] Edery, F. and Kanaev, A. *Two-photon laser-induced fluorescence of* H_2O *and* D_2O *molecules at ambient pressure*. The European Physical Journal D, **23**(2):257–264, 2003.

[160] Läuter, A., Naik, P.D., Mittal, J.P., Volpp, H.R., and Wolfrum, J. *Laser-induced fluorescence study of the hydrogen atom formation dynamics in the 248 nm gas-phase photodissociation of vibration state selected water* ($H_2O(| 04^{-}\rangle)$). Research on Chemical Intermediates, **33**:513–522, 2007.

[161] Sinha, A., Coleman, J., and Barnes, R. *Photodissociation dynamics of* HO_2 *at 220 nm: determination of the* $O(^1D)$: $O(^3P)$ *branching ratio*. Journal of Physical Chemistry, **98**(48):12462–12465, 1994.

[162] Brouard, M., Martinez, M.T., O'Mahony, J., and Simons, J.P. *Photofragment vector correlations in the vibrationally mediated photodissociation of* H_2O_2. Chemical Physics Letters, **150**(1-2):6–12, 1988.

[163] Likar, M.D., Baggott, J.E., Sinha, A., Ticich, T.M., Vander Wal, R.L., and Crim, F.F. *Vibrationally mediated photodissociation*. Journal of the Chemical Society-Faraday Transactions II, **84**:1483–1497, 1988.

[164] Brouard, M. and Mabbs, R. *Vibrationally mediated photodissociation of* H_2O_2 $(4\nu_{OH})$*: rotational state dependent photodissociation cross sections and vibrational state mixing*. Chemical Physics Letters, **204**(5-6):543–550, 1993.

Summary of Papers

I. A conceptually new wide-field method for obtaining single-acquisition fluorescence lifetimes in 2D is reported. Two cameras are used, and the concept is based on a thorough characterization of the experimental setup so that a library of simulated signal ratios can be compared to experimental data. Fluorescence lifetimes of less than 1 ns recorded in single shot in gas phase experiments are shown. A geometrical interpretation is presented, and it is shown that it is the difference of the temporal expectation values of the signals measured by the two cameras that makes the formed ratio a function of the fluorescence lifetime with determinate solutions. Hence, the technique allows all photons reaching the cameras to be detected, which can provide maximum signal-to-noise ratio. Moreover, a choice of gate functions that, in theory, will provide equally good sensitivity for any fluorescence lifetime is suggested.

   Andreas Ehn and I planned the measurements together with Joakim Bood. I took part in building the setup and I participated in all the experimental work. I wrote the image-overlapping algorithms and derived the equation that provides the geometrical interpretation of when the ratio is a function of the fluorescence lifetime. I assisted in writing the manuscript.

II. In this paper the fluorescence lifetime algorithm described in paper I is used to quenching-correct LIF measurements obtained in a rich CH_4/O_2 flame using 355 nm for excitation. Neither is the DIME concept used in single shot, nor are the ideal gates discussed in paper I used. However, the DIME concept is shown to work in a practical combustion application, and in this case, more important, it is demonstrated that even qualitative LIF measurements can be wrongly interpreted if the data are not corrected for differences in fluorescence lifetimes.

   Andreas Ehn, Joakim Bood and I planned the measurements. I took part in the experimental work. The image-overlap algorithms that I had previously programmed were used for image overlapping. I wrote part of the paper.

III. This paper proposes photofragmentation laser-induced fluorescence to be a practical diagnostic tool for detection of gas phase H_2O_2. The PF-LIF scheme for applied H_2O_2 measurements is explained, and it is demonstrated that the PF-LIF signal increases linearly with the gas phase H_2O_2 concentration. A detection limit of 30 ppm is estimated for 2D measurements with the current setup.

Joakim Bood and I planned the measurements and the layout of the paper. I constructed the experimental setup, and I did the measurements together with Joakim Bood. We also wrote the paper.

IV. In this conference contribution a single-shot acquisition obtained in a non-steady free flow of H_2O_2 is presented. The pixel intensities are converted to H_2O_2 concentrations after laser-intensity corrections since the maximum concentration is known to be the equilibrium vapor pressure for a 50% (weight) solution of H_2O_2/H_2O at 296 K.

I planned the measurements together with Joakim Bood. I built the experimental setup, conducted the measurements and wrote the paper with the assistance of Joakim Bood.

V. This paper demonstrates how the photolysis fluence affects the OH-photofragment chemical consumption for an initial system of H_2O_2, H_2O and a bath gas. This study is important in order to be able to perform quantitative PF-LIF measurements of H_2O_2 based on the chemical consumption of OH following photolysis. It is shown that the OH decay is faster for high photolysis fluences than for low fluences. A chemical kinetic model including 14 elementary reactions is proposed and shown to explain the experimentally observed behavior.

I planned the measurements and the structure of the paper together with Joakim Bood. I constructed the experimental setup, did the measurements and developed the code used to simulate the PF-LIF signal as a function of the delay time between the photolysis laser pulse and the probe laser pulse. I also wrote the majority of the paper.

VI. This manuscript reports on measurements performed in two industrial test rigs at Tetra Pak Packaging Solutions AB in Lund, Sweden. The PF-LIF technique is demonstrated to be useful for imaging of H_2O_2 flows in industrial applications. Local concentration buildup in water and gas are compared. In addition, comparisons of quantitative H_2O_2 concentration measurements using different techniques are reported on.

I planned the study together with Ulf Lindblad, Alaa Omrane and Hans Seyfried. I assisted Fredrik Hellqvist in some of the work on the gas rig, and I constructed the setup used for the PF-LIF measurements, which I also performed. I did the water-rig measurements together with Hans Seyfried. I wrote the manuscript.

VII. Photofragmentation laser-induced fluorescence measurements are performed in laminar, premixed flames. The distribution of primarily HO_2 is for the first time shown in 2D in flames. For rich CH_4/O_2 flames, CH_3O_2 was found to give a detectable photofragment signal contribution. The CH_4 flames had interfering signal contributions in their reaction and product zones. Measurements as well as calculations suggest photolysis of CO_2 to be the underlying source. Carbon dioxide cannot by itself give rise to OH from photodissociation. Chemical kinetic calculations suggest that most of these interfering OH molecules are created in reactions between O atoms formed from photolysis of CO_2 and naturally present H_2O and H_2.

I planned most of the experimental work together with Joakim Bood. I built the experimental setups for the majority of the studies, and I had the lead role in all experimental work. Joakim Bood and I did the data analysis, and I wrote the majority of the paper. It should be pointed out that Alexander Konnov performed all chemical kinetic calculations. However, with assistance from Joakim Bood, I did all the calculations needed to compare measurements and calculations.

VIII. This manuscript presents ps-LIF results obtained in a flow of toluene mixed with different levels of O_2 and N_2 at ambient pressure and temperature. The fluorescence lifetime is shown to follow a Stern-Volmer expression. The slope is derived and presented. Information regarding the fluorescence lifetime of toluene exposed to different levels of O_2 allows fluorescence lifetime imaging to be used for visualization of gas mixing.

I participated in the experimental work and have taken part in discussions regarding interpretation of the results.